Neutron scattering on magnetic nanostructures

Frédéric OTT

IRAMIS - Laboratoire Léon Brillouin CEA/CNRS
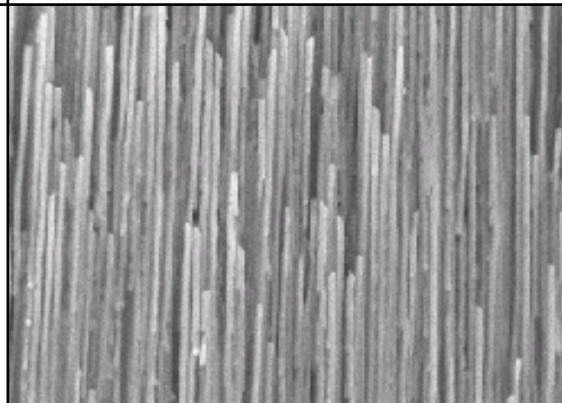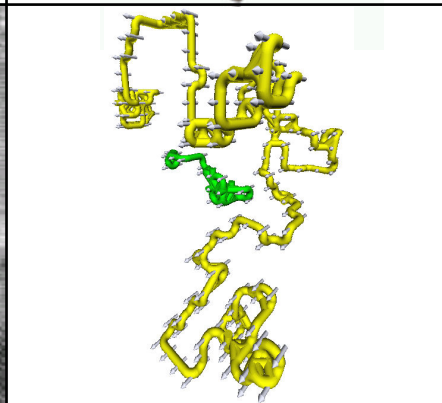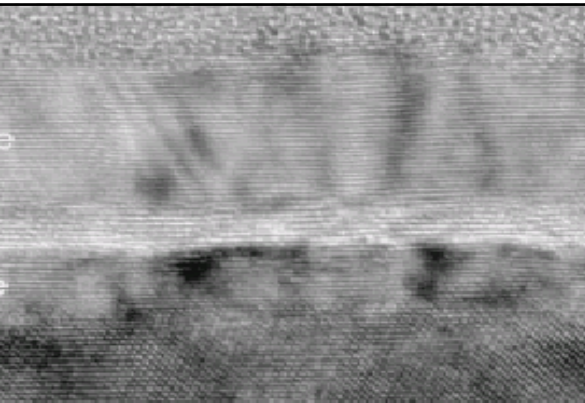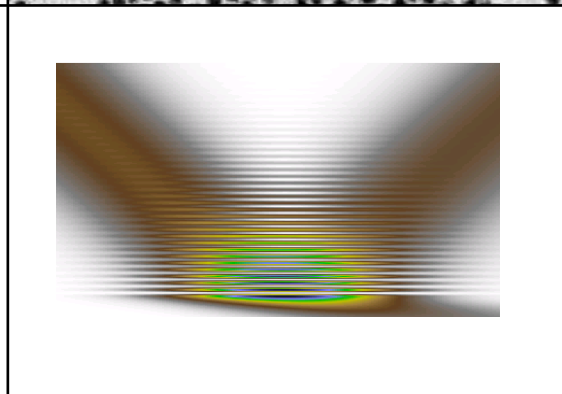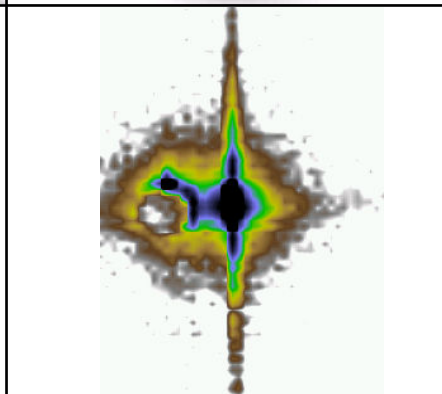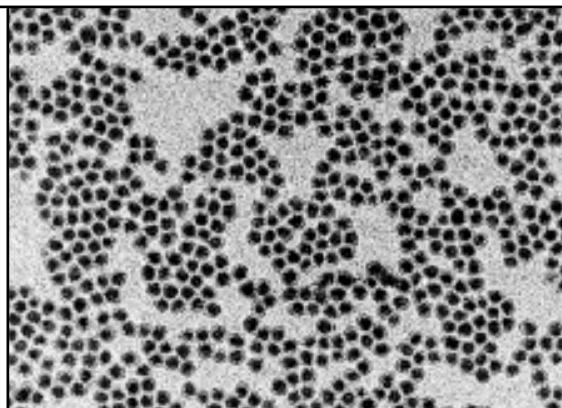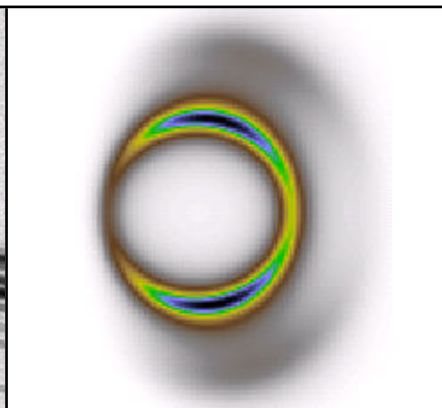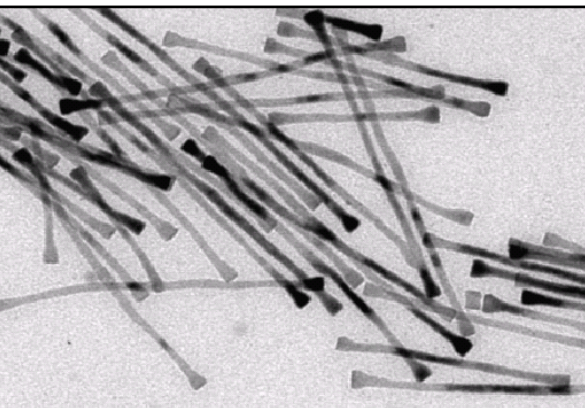
Frédéric OTT
IRAMIS - Laboratoire Léon Brillouin UMR12 CEA/ CNRS
Centre d'Etudes de Saclay
F-91191 Gif sur Yvette Cedex
France

Tél : 01 69 08 61 21
Fax : 01 69 08 82 61
Mail : Frederic.Ott@cea.fr

Cover illustrations (top-left to right-bottom)
> *Nanowires grown in an alumina membrane*
> *Off-specular neutron scattering*
> *Magnetic domains in FePd layers*
> *Magnetic nanowires*
> *SANS on plane of nanowires*
> *Magnetic Co nanoparticles*
> *Bloch wall*
> *GISANS signal*
> *Neutron wave-function during a reflection on a surface*
> *Spin-valve system*
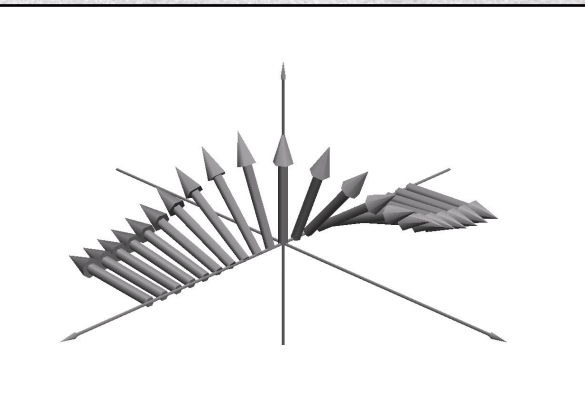> *Magnetic percolation path in a magnetic crystal*
> *Magnetic nanowires*

Neutron scattering on magnetic nanostructures

Frédéric OTT

Laboratoire Léon Brillouin UMR12 CEA/CNRS
Centre d'Etudes de Saclay F-91191 Gif sur Yvette, FRANCE

Version 1.0

January 11, 2009

Contents

Contents

Contents

Preamble

During the last 10 years, I have devoted my work to the development of neutron scattering techniques for the study of different types of magnetic nanostructures and I have been trying to apply and adapt neutron techniques to study new types of systems. I have tried to organize this manuscript in order to give a broad overview of all the possibilities offered by the neutron scattering techniques. In order to illustrate the different possibilities, I have selected studies that I have performed at the Laboratoire Léon Brillouin but in some cases experiments performed in other neutron centers are also presented either because they were pioneering work, or because they are very illustrative or for the sake of completeness.

I also intend this document to be a review of the state of the art in neutron scattering techniques so that scientists interested in applying these techniques on magnetic nanostructures can quickly evaluate if they are suitable or not for their problems. I have thus tried to limit as much as possible the technical and theoretical aspects of the different techniques and focused on the achievable goals. Readers are invited to refer to separate publications for detailed discussions of the techniques.

In a first chapter, I browse through the different types of magnetic systems and nanostructures that are being studied at the moment and show how rapidly the field has evolved in the last 15 years.

In a first part, the different neutron scattering techniques are described. I present the reflectivity technique, including off-specular scattering, the Small Angle Scattering technique and the derived technique of Grazing Incidence Small Angle Scattering. I also mention the technique of neutron diffraction which can be applied on some epitaxial systems. The use of these different techniques is illustrated by studies performed on various spectrometers at the Laboratoire Léon Brillouin and in other neutron centers.

In a second part, I discuss a more specific topic which are magnetic non collinear structures and helical orders in magnetic nanostructures. I show how neutron scattering can probe such structures in a unique way since the inner configuration of very complex magnetic structures can be accessed. In a first chapter, I present examples of such non collinear structures in various thin film systems and in a second chapter, experiments on magnetic single crystals.

In a last part, I focus on instrumentation and software developments. Both fields are very important in the implementation of new neutron scattering techniques. In a first chapter several concepts of new instruments are presented. They should allow to bring neutron reflectivity a step forward by providing significant gains in flux. In the last chapter, I describe the software packages which I have developed.

A last chapter I review the perspectives offered by neutron scattering on magnetic nanostructures in the next decade and present my projects for the future.

The last part compiles various annexes on specific technical points which would have been too long to develop in the main text.

NOTATIONS

b	scattering length of a nucleus
ρ	atomic density (atoms per m^3)
n	refractive optical index
σ	absorption cross section (barn)
$V(r)$	interaction Hamiltonian
d	thickness of a layer
$\mathbf{k}$	wave vector
m	neutron mass
m_e	electron mass
e	charge of the electron
Q	scattering wave-vector
g	Landé factor, (g =2)
g_n	$g_n = -1.9132$, nuclear Landé factor of the neutron
λ	neutron wavelength
$\mathcal{E}_0$	energy of the neutron in the vacuum
μ_B	Bohr magneton $\mu_B = e\hbar/(2m_e) = 9.27 \times 10^{-24}\ J.T^{-1}$
μ_n	nuclear magneton $\mu_n = e\hbar/(2m_p) = 5.05 \times 10^{-27}\ J.T^{-1}$

We call "up" (resp. "down") the neutron polarisation parallel (resp. anti-parallel) to the external applied magnetic field.

1. Magnetic nanostructures

During the last 20 years, the field of the magnetism of nanostructures has exploded. A huge number of new magnetic structures have appeared in which the nanometer scale plays a key role. It is possible to classify them into 3 categories:

- In 1 dimension, *thin films* produced by physical means such as vacuum deposition (sputtering, evaporation, laser ablation ...): metal thin films, oxide thin films, magnetic semi-conductors.
- In 2 dimensions, *nanometer size objects organized on surfaces*. These objects can be either produced by lithography techniques or by self-organization processes.
- In 3 dimensions, *nanoparticles* in solutions forming ferrofluids or *nanomagnetic entities* in crystals.

In the following, I describe the different fields and topics in which neutron reflectivity and neutron scattering has been applied for the study of magnetic nanostructures.

1.1. Magnetic thin films

During the early 1980s, advanced techniques for the deposition of ultra-thin metal films have been developed. This has led to the fabrication of new artificial materials comprising of the stacking of different materials in thin sandwiches (hetero-structures). The combination of different types of materials has given rise to new physical phenomena. The first new phenomenon to be probed was the magnetic exchange coupling in super-lattices (Fig. 1.1a). It appeared that magnetic layers separated by non magnetic spacer layers can be magnetically coupled. The coupling can be either ferromagnetic, anti-ferromagnetic or more complex (quadratic or even helical). The coupling can also change sign (from ferro to anti-ferro) as a function of the spacer layer thickness. Such phenomena were observed in rare-earth super-lattices (Gd/Y, Dy/Y, Gd/Dy, Ho/Y [1]), transition metals super-lattices (Fe/Cr [2, 3], Co/Cu [4], Fe/V [5], Co/Ru [6]), mixing of semiconductors and metals (Fe/Si [7], Fe/Ge [8]). The field is still open and new systems are still being synthesized, especially with magnetic semi-conducting materials (GaMnAs [9], EuS/PbS [10]).

These magnetic coupling phenomena are strongly connected to the Giant Magneto-Resistance effect [11] : depending on the orientation of the magnetization of the different layers in the hetero-structure, the electrical resistivity of the system varies significantly. This has opened a new field of study which is now referred to as *spintronics*.

In the early 1990s, the phenomenon of exchange bias was revived. A ferromagnetic layer in contact with an anti-ferromagnetic material can be magnetically strongly coupled (Fig. 1.1b) [12, 13]. The soft magnetic layer is thus strongly pinned along a well defined direction. This is presently used in most of the spintronics systems (Fig. 1.1c). The phenomenon is used in commercial devices but is still not fully understood from a

theoretical point of view. The origin of the coupling depends on the type of materials, their crystallinity, the fabrication process... [14].

In the late 1990s, it appeared that the performances of giant magneto-resistive systems could be enhanced by combining tunnel barriers and magnetic materials (using materials such as Fe_2O_3, Fe_3O_4, $CoFe_2O_4$, MgO, Al_2O_3. This field is still very active and a number of phenomena still need to be understood. Electronic devices using magnetic tunnel junctions (such as Magnetic Random Access Memories) are about to be commercialized but significant progress can still be made.

Besides the combination of well known materials, during the late 1990s, a wealth of new materials were synthesized (typically perovskites of the type $ABMnO_3$). The growth of these materials as epitaxial thin films was quickly mastered following the experience acquired previously on oxide superconductors. These materials have properties ranging from colossal magneto-resistance to magneto-electric effects [15].

More recently, a new field has developed which is the search for new magnetic semi-conductors. After the early studies of Eu based magnetic semi-conductors (EuO and EuS) in the 1970s, the field was dormant until $GaMnAs$ magnetic semiconductors were synthesized in the middle of the 1990s. Since then, a number of new systems have been synthesized in order to find room temperature magnetic semi-conductors. The discovery of a suitable material could boost the field of spintronics. These new materials range from diluted semi-conductors ($GaMnN$, $SiC:Fe$, $GeMn$) to magnetically doped insulating oxide materials ($ZnO:Co$, $ZnO:Mn$, $TiO_2:Co$, $ZnFe_2O_4$).
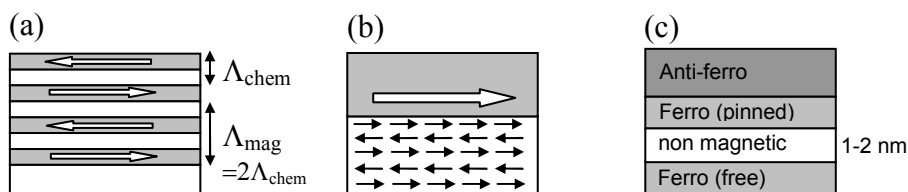
Figure 1.1.: *(a) Exchanged coupled super-lattice with an anti-ferromagnetic order. (b) Exchange bias between a ferromagnet and an anti-ferromagnet. (c) GMR spin-valve system or magnetic tunnel junction.*

Besides these extensively studied topics, we can also mention other types of studies on magnetic thin films such as the penetration of the magnetic flux in superconductor thin films [16], the exchange spring effect between soft and hard magnetic layers [17], the magnetism of ultra-thin films [18], proximity effects between magnetism and super-conductivity [19], induced magnetism at interfaces (e.g. the magnetism induced in V in contact with Gd [20]), the super-anti-ferromagnetism (edge effects in Fe/Cr super-lattices [21]).

1.2. Nanometer size objects organized on surfaces

The natural extension of the development of thin film structures was to try to organize nanostructures in the plane of thin films. A number of techniques have been used to create 2D nanostructures.

Bottom-up approaches.

(i) The earliest one was to control the adsorption of atoms on clean surfaces, using the substrate intrinsic structure (atomic steps for example). Atoms deposited on such surfaces can in some conditions organize themselves into ordered 2D structures [22] (Fig. 1.2a). Such processes are however often limited to rather small structures and the flexibility of the technique is limited since it usually depends on very specific thermodynamic conditions.

(ii) The second technique derived from the previous one is to synthesize the objects of interest prior to their deposition on surfaces. This has been extensively studied in the case of the adsorption of small spherical nanoparticles on surfaces. In order to obtain a better ordering, the surface may be *prepared* to guide the organisation of the nano-objects

(iii) In some specific cases, the magnetic nano-organisation may result form intrinsic properties of the material. For example, FePt, FePd or CoPt thin films develop a complex 2D magnetic domains pattern (Fig. 1.2d).

Top-bottom approaches.

(iv) It is also possible to devise techniques derived from traditionnal lithography processes. Unfortunately, optical lithography is limited to "large scales" (above $100\,nm$, at least until recently). Electronic lithography only allows to produce very small samples with a very limited surface ($< 0.1mm^2$). Thus techniques using self-organized templates have been used to create the equivalent of masks which could then be used for the fabrication of regular nanostructures [23, 24]. This is illustrated in the case of alumina masks (see Fig. 1.2c) in which either dots or wires are deposited using electrochemical methods (Fig. 1.2).
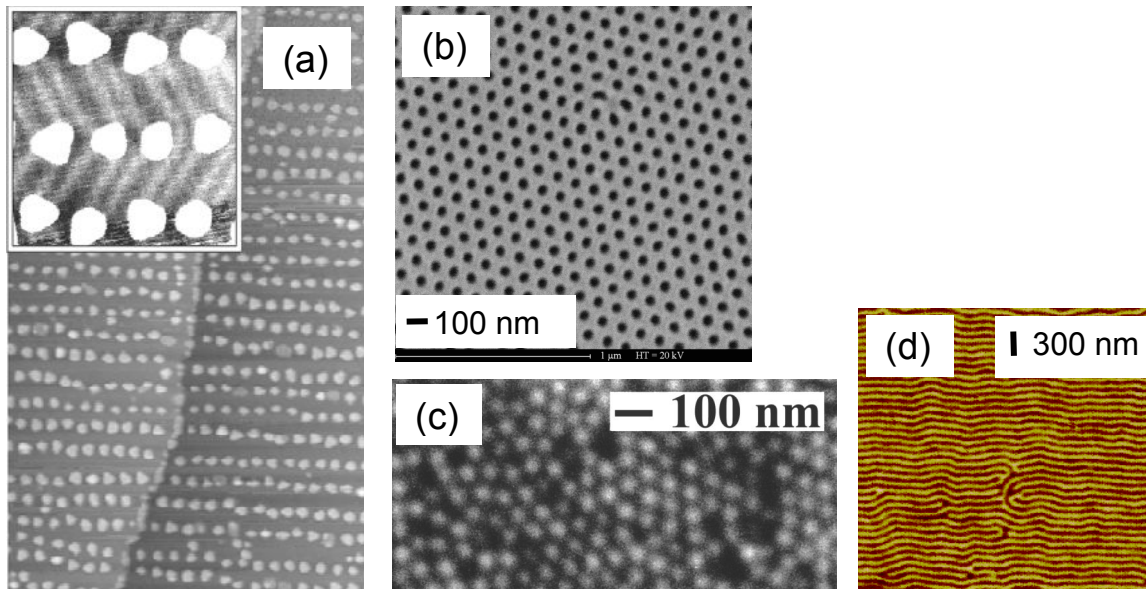
Figure 1.2.: *(a) $300 \times 300nm$ image of self-organized Co dots on a gold substrate [22]. (b) Alumina membrane with pores of diameter $60\,nm$ in which metals can be electrochemical grown. (c) Fe nanodots with average diameter and periodicity of 32 and $63\,nm$ grown using a Al_2O_3 mask [24]. (d) Magnetic domains in a FePt thin film. The periodicity of the pattern is 100 nm.*

1.3. Magnetic nanostructures in 3D

This category is very broad but can nevertheless be divided in two main classes of magnetic materials:

(i) Systems in which the magnetic nanostructures appear as an instrinsic property of a bulk material. One can mention magnetic phase separations in crystals (often oxide materials), the formation of a self organized magnetic domain structure, the critical fluctuations at the Curie temperature which can take place over nanometer scales, metallic alloys such as steels containing magnetic inclusions.

(ii) Systems which are created from scratch usually using a *bottom-up* approach. For a long time, the basic building bricks have been spherical nanoparticles (either oxide or metallic). These nano-bricks may in some cases form macroscopic pseudo-crystal structures [25, 26] (Fig. 1.3). In these systems, not only the individual magnetic structure is interesting (core-shell [27]) but also the properties of the assembly of particles (transport properties, magnetic coupling, chains formations, materials reinforcement, solidification of ferrofluids). More recently, more complex nano-objects have started to be synthesized (see Fig. 1.4) such as nanowires [28] or nanotubes.
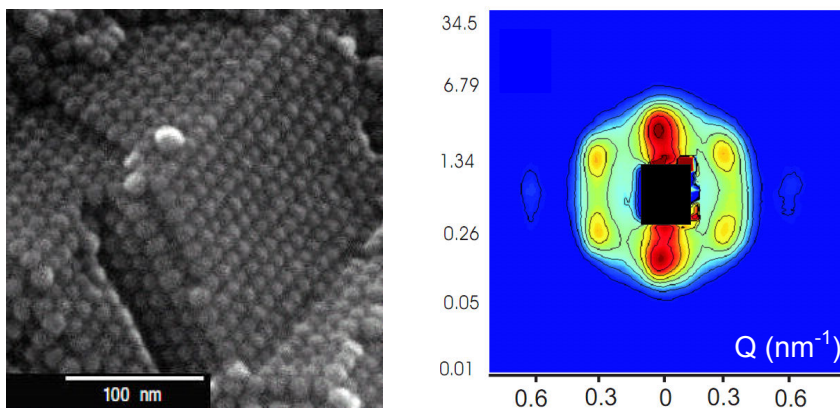
Figure 1.3.: *(left) Crystal of FeCo nanoparticles [25]. (right) Hexagonal order in a ferrofluid probed by SANS [26].*
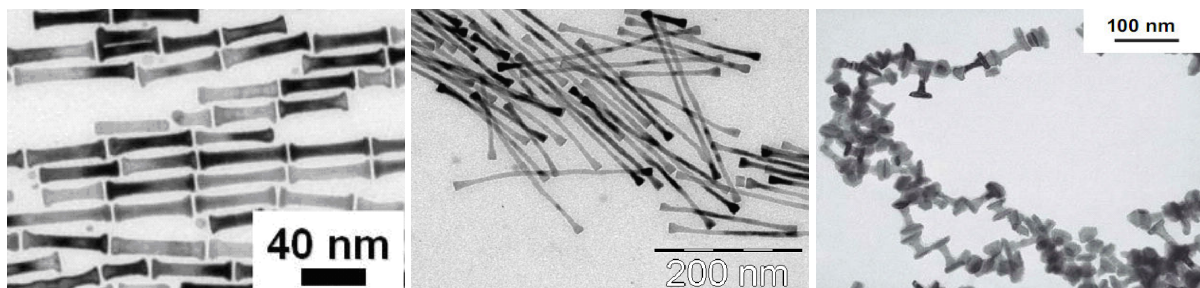
Figure 1.4.: *Co and $Co_{80}Ni_{20}$ nanowires (courtesy of G. Viau).*

This chapter gave a quick overview of the different magnetic nanostructures which have been synthesized during the last decade. In the following chapter, we will describe how neutron scattering can contribute to the study of these systems.

Part I.

Neutron scattering techniques applied to magnetic nanostructures

Framework

In this first part, I describe the state of the art of the different neutron scattering techniques applied to the study of magnetic nanostructures. For each of the different techniques, I give a short description of the technique and illustrate its use with a few examples of studies performed in the past years at the Laboratoire Léon Brillouin.

Case of thin films and planar nanostructures

Magnetic surfaces and interfaces at the nanometric scale correspond to very small volumes of matter, of the order of a few micrograms. The use of a grazing incidence geometry increases the neutron interaction with the sample surface and makes such experiments feasible.

At grazing incidence, it is possible to distinguish 3 scattering geometries (Fig. 1.5):

* specular reflection,
* scattering in the incidence plane (off-specular scattering),
* scattering perpendicular to the incidence plane (Grazing Incidence SANS).

Specular reflection
$0.06 < Q_z < 3$ nm^{-1}
3 nm $< \xi < 100$ nm

Incidence plane
$10^{-4} < Q_x < 10^{-2}$ nm^{-1}
600 nm $< \xi < 60$ µm

Plane perpendicular
to the incidence plane
$10^{-4} < Q_y < 3$ nm^{-1}
3 nm $< \xi < 100$ nm
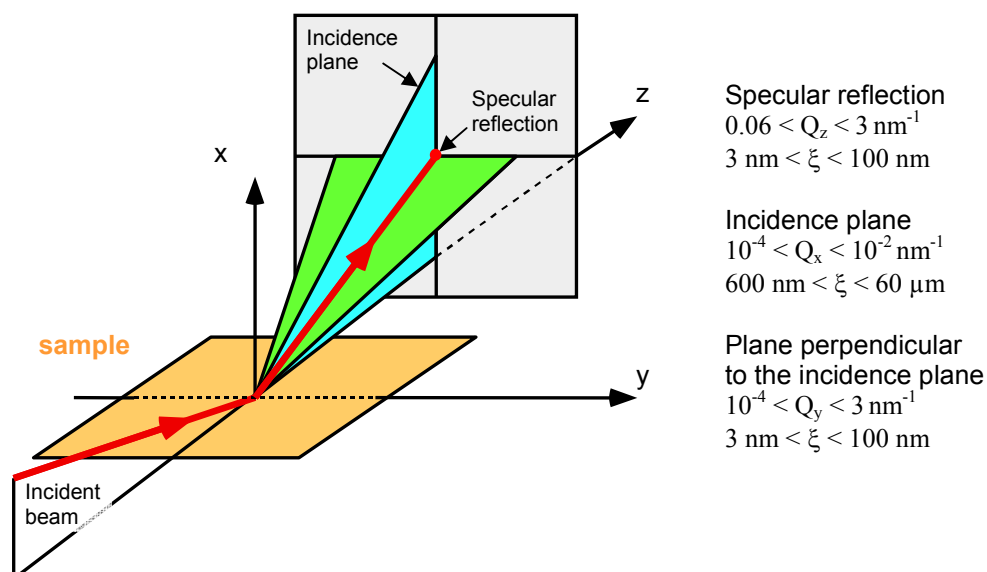
Figure 1.5.: *The different surface scattering geometries. (red line) specular reflectivity geometry; (blue plane) off-specular scattering plane, corresponding to the incidence plane; (green plane) GISANS scattering plane, perpendicular to the incidence plane. These different scattering geometries probe a very wide range of length-scales both in the depth and along the surface of the film.*

These different scattering geometries probe different length-scales ξ and directions in the sample surface. Specular reflectivity probes the structure along the depth in the film ($3\,nm < \xi < 100\,nm$). Off-specular scattering probes surface features at a micrometric

scale (600 $nm < \xi < 60\,\mu m$). Grazing Incidence SANS probes surface features in the range $3\,nm < \xi < 100\,nm$. These different scattering geometries allow the study of a very wide range of length-scales ξ ranging from a few nm up to several μm both in the depth and on the surface of the film.

Chapter 1 will be dedicated to specular reflectivity which is the most routinely used technique. Chapter 2 will quickly describe the off-specular technique. Chapter 3 will describe the Small Angle Scattering (SANS) technique which can be used in the situations where a large amount of matter is available (such as crystals or powders). Chapter 4 will then describe how the SANS technique can be extended to the study of planar nanostructures.

Finally, I will mention the possibilities offered by other neutron techniques such as single crystal diffraction and inelastic scattering in Chapters 6 and 7.

2. Specular reflectivity

2.1. Principles

Neutrons can be reflected on surfaces in the same way as x-rays or electrons [29]. All the formalisms developed for x-ray reflectivity can be transposed to neutron reflectivity [30]. In a reflectivity geometry (Fig. 2.1a), the incidence angle θ_i on the surface is small (typically ranging from 0.5 to 5°). The reflection angle θ_r is the same as the incidence angle θ_i. As a consequence, the scattering wave-vector Q is perpendicular to the surface. The typical range of accessible scattering wave-vector $Q = k_r - k_i$ is $0.05 - 3\,nm^{-1}$. This corresponds in the real space to typical length-scales ranging between 2 and $100\,nm$ so that neutron reflectivity does not probe structures at the atomic level. In a reflectivity geometry it is thus possible to do the "optical approximation" [30] and model the neutron interaction with the material as a continuous potential. The details of the atomic structure are smoothed out (Fig. 2.1b). The interaction potential V with a material is given by:

$$V = \frac{h^2}{2\pi m}\rho \quad with \quad \rho = \frac{1}{V}\sum_i b_i$$

where h is the Planck constant and m is the neutron mass. ρ is called the "scattering length density" and is the average of the nuclear scattering lengths b_i of the different nuclei in the material in a small volume V.

In the case of a magnetic system, the interaction between the neutron spin and the material magnetization is of the form $V = -\overrightarrow{\mu}.\overrightarrow{B}$ where $\overrightarrow{\mu}$ is the magnetic moment of the neutron and $\vec{B}$ is the magnetic induction inside the thin film.

In the reflectivity geometry, the equivalent of a neutron "optical index" can be derived from the Schrödinger equation [30]. Neglecting absorption, the value of this optical index is given by the following expression:

$$n^{\pm} = 1 - \delta \mp \delta_M = 1 - \frac{\lambda^2}{2\pi}\rho \mp \frac{m\lambda^2}{h^2}\mu.B$$

where δ is the nuclear contribution to the optical index, and δ_M is the magnetic contribution to the optical index. The sign of the magnetic contribution depends on the relative orientation of the neutron spin with respect to the magnetization (parallel or anti-parallel). Table 2.1 gives values of optical indexes for some typical materials. One should notice that the magnetic optical index is of the same order of magnitude as the nuclear optical index. The use of polarized neutrons permits to measure both optical indexes n^+ and n^- and thus to obtain detailed information about the magnetic structure of the sample.

In a specular reflectivity measurement, the most important assumption is that the system is invariant in translation in the thin film plane, that is, there are no inhomogeneities along the film surface. Thus the interaction potential V is assumed to be only a function

2. Specular reflectivity
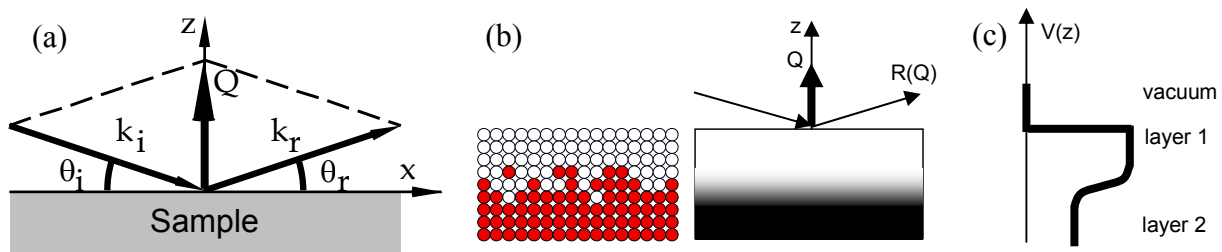
Figure 2.1.: *(a) Specular reflectivity geometry. The reflection angle is equal to the incidence angle; the scattering wave-vector Q is perpendicular to the sample surface. (b) Interface between 2 surfaces. In the optical approximation, the interface is approximated as a continuous medium. (c) Reflection on a thin film deposited on a surface. The reflectivity measures the Fourier transform of the interaction potential V(z).*

element	$\delta(\times 10^{-6})$	$\delta_M(\times 10^{-6})$	σ_a(barns)
Fe	20.45	11.7	2.56
Co	5.7	10.3	37.2
Ni	24	3.7	4.49
Gd	5.0	14.5	49700

Table 2.1.: *Nuclear and magnetic optical index $n = 1 - \delta \pm \delta_M$ for some materials at $\lambda = 0.4nm$.*

of the depth z in the multilayer system (Fig. 2.1c). In a first approximation, the specular reflectivity measures the Fourier transform of the optical index profile $n(z)$.

However, at low incidence angles, there is total reflection up to a critical wave-vector Q_c and thus the Born approximation is not valid at small scattering wave-vectors. The Born approximation can be applied only above a scattering wave-vector of about $3Q_c$. Below this limit, one must solve the Schrödinger equation and perform a full dynamical calculation. The detailed theoretical treatment of the polarized reflectivity can be found in [30, 31, 32, 33, 34].

Figure 2.2a presents the situation of the reflection of a neutron beam on a multilayer Si//Cu/Cr: above the critical wave-vector of total reflection, the reflected intensity decreases as $1/Q^4$. Modulations of the reflected intensities are observed. They correspond to constructive and destructive interferences of the neutron waves scattered by the different interfaces of the multilayer system. These oscillations are called Kiessig fringes. Their pattern is characteristic of the multilayer system. Figure 2.2b presents the situation of a magnetic thin film on a substrate. In this case, the optical index depends on the relative orientation of the neutron spin with respect to the thin film magnetization. The measured reflectivity is very different for neutron incident with a spin parallel to the magnetization (optical index $n^+ = 1 - \delta - \delta^+$) and for neutrons incident with a spin anti-parallel to the magnetization (optical index $n^+ = 1 - \delta + \delta^-$).

The measure of the reflectivity probes the profile of optical index $n(z)$ along the normal
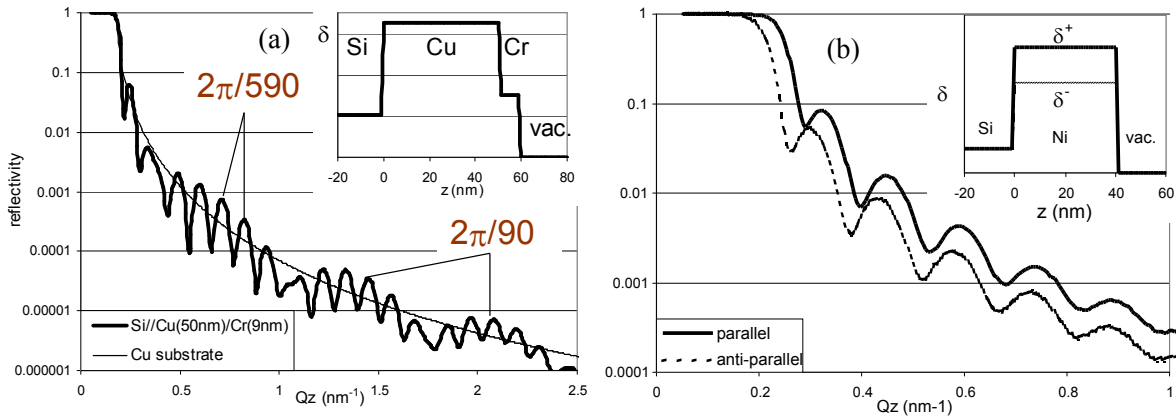
Figure 2.2.: *(a) Reflectivity on a multilayer system Si//Cu(50nm)/Cr(9nm). The short period oscillations are characteristic of the total thickness of the layer (59nm). The long range modulation is characteristic of the thin Cr layer (9nm). (Insert) optical index profile as a function of the depth in the film. (b) Reflectivity of a magnetic film Si//Ni(40nm). The reflectivity depends on the relative orientation of the neutron spin with respect to the magnetization. (Insert) optical index profile for both neutron polarizations (parallel and anti-parallel).*

(Oz) to the thin film system. Numerical models are then used to reconstruct the thickness of the different layers of the system as well as their individual scattering length densities ρ which is characteristic of their chemical composition. Inter-diffusion and roughness at interfaces can be quantified with more detailed models. In the case of magnetic systems, information on the amplitude and the direction of the magnetization of the different layers can be obtained using polarized neutron reflectivity. One should note that polarized reflectivity is sensitive to the induction in the thin films: no difference is made between the spin and orbital magnetic moments. In practice, it is possible to measure 4 cross-sections in a polarized reflectivity experiment: 2 non spin-flip cross sections, R^{++} (resp. R^{--}), corresponding to the number of incoming "up" (resp. "down") neutrons reflected with an "up" (resp. "down") polarization; 2 spin-flip cross sections, $R^{+-} = R^{-+}$, corresponding to the number of neutrons experiencing a spin-flip during the reflection on the sample. In a first approximation, the non-spin-flip cross sections probe the components of the magnetization which are parallel to the applied field; the spin-flip cross sections are sensitive to the components of the magnetization perpendicular to the applied field. Combining this information it is possible to reconstruct the magnetization direction and amplitude along the depth of the film. The depth resolution is of the order of 2-3 nm in simple systems. Polarized reflectivity is a surface technique and thus is not sensitive to paramagnetic or diamagnetic contribution from the substrate. There is no absorption. There are no phenomenological parameters. The data are "naturally" normalized. All these characteristics make neutron reflectivity data easy to model and interpret.

In the following, we will illustrate some of the possibilities offered by polarized reflectivity on super-lattices and single thin films. For other examples, the interested reader should refer to the following recent reviews [35, 36, 37, 38, 39].

2.2. Examples

2.2.1. Super-lattices

2.2.1.1. Magnetic coupling in periodic Multilayers

A super-lattice consists of a periodic repetition (n times) of a bilayer system $[A/B]_n$. (see Figure 1.1a). If the material **A** is magnetic, depending on the thickness of the intermediate layer **B** (from 0.5 to 3 nm) and the type of the **B** material (Cr, Mn, Cu..) a magnetic coupling can be mediated through this non magnetic **B** layer. The coupling energy can be described by using an energy of the form :

$$E_{coupling} = -J_1 \, \vec{S}_1 \cdot \vec{S}_2 - J_2 \, \left(\vec{S}_1 \cdot \vec{S}_2 \right)^2$$

Depending on the sign and magnitude of the coupling constants J_1 and J_2, a variety of magnetic orderings can be observed. Usually the coupling constant oscillates between positive and negative values as a function of the thickness of the **B** spacer, thus the magnetic order between the **A** layers changes from ferromagnetic to anti-ferromagnetic. In some structures it is even possible to observe non collinear coupling between the different magnetic layers.
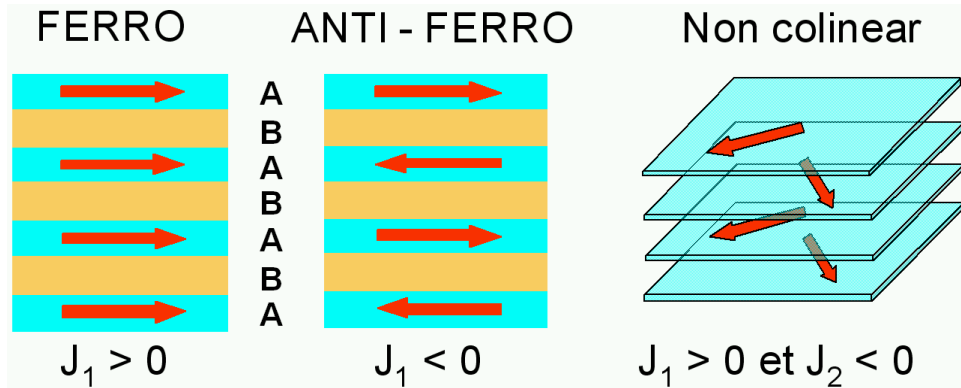
Figure 2.3.: *Different types of magnetic couplings in super-lattices.*

In the case of periodic multilayers, Bragg peaks corresponding to the period of the multilayer can be observed. With polarized neutrons, it is possible to measure very rapidly a precise value of the average magnetic moments. In the case of antiferromagnetic coupling or variable angle coupling, it is possible to obtain directly a mean angle between the different magnetic layers. If high order Bragg peaks are observed, a detailed description of the chemical and magnetic interface can be obtained. In the literature, there is a large amount of results on magnetic multilayers [6, 35, 40]. The most thoroughly studied system is the metallic system Fe/Cr. The pioneering polarized neutron reflectometry studies have been performed on this system [41]. Though the origin of the magnetic coupling is well understood in metallic hetero-structures [42], the exact origin of the ordering in structures combining semi-conductors or even insulators [43] is still unclear.

2.2.1.2. Metal super-lattice

Figure 2.4 shows an example of polarized neutron reflectometry on a system $[Fe(2.5nm)/Si(1.2nm)]_n$ produced by MBE by K. Fronc from the Polish Academy of Science. The reflectivity was measured at 20K in a planar field of 20 mT. At the position $Q = 0.17\text{Å}^{-1}$, the peak is indicative of the period of the super-lattice defined by the thickness 3.7 nm of the $[Fe(2.5nm)/Si(1.2nm)]$ bilayer. It corresponds to the [001] peak of the super-lattice. A magnetic contrast between the "up" and "down" reflectivities exists corresponding to a net magnetization component along the applied field. A the position $Q = 0.085\text{Å}^{-1}$, that is [0 0 ½], a strong diffraction peak is observed. It indicates an anti-ferromagnetic component. But the existence of a very strong spin-flip peak at [0 0 ½] indicates that a non collinear magnetic order has also set in the structure. Numerical modeling suggests that the Fe layers are arranged so that the magnetizations of alternating Fe layers make an angle of 30° with respect to the applied magnetic field. The magnetic moment of the Fe layer is however reduced to 1.4 μ_B per Fe atom because of the Si inter diffusion and of the fact that the Fe layers are very thin. In this system, magnetic fields larger than $1\,T$ are necessary to fully align the magnetic moments and make the AF component disappear. The question of the origin of the coupling remains unclear.
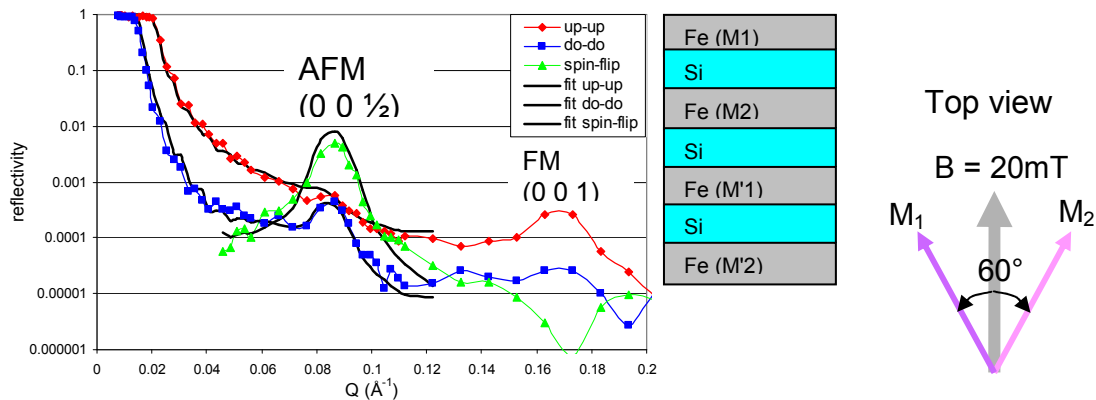
Figure 2.4.: *(a) Reflectivity of a $[Fe(2.4nm)/Si(1.2nm)]_n$ multilayer measured at 5 K. (b) Configuration of the magnetic moments in 2 adjacent Fe layers [7].*

The studies of the magnetic coupling in magnetic superlattices are still numerous: in metallic superlattices, Pd/Fe [44], Heussler alloys [45, 46], U/Fe [47]; in heterostructures involving semi-conductors Fe/Ge [48]; in rare-earths based materials $DyFe_2/YFe_2$ [49], Ho/Y [50]; in metal oxide layers Co/Al_2O_3 [51].

In such multilayer systems, neutron reflectivity can be sensitive to very small magnetic moments. In $[GaAs/GaMnAs]_n$ superlattices, magnetizations as small as $27kA/m$ (0.03T) can be determined [?].

2.2.1.3. Magnetic oxide super-lattice

This example illustrates the use of the magnetic contrast to measure the chemical segregation in manganite hetero-structures: $[(LaMnO_3)_a/(SrMnO_3)_b]_n$ (with 8 < a < 12 ; 4 < b < 8). These layers have been produced by P. Lecoeur by Pulsed Laser Deposition.

2. Specular reflectivity

These super-lattices are deposited layer by layer in order to enforce a cationic order between La and Sr and a cationic segregation between Mn^{3+} and Mn^{4+}. The first material is anti-ferromagnetic in its bulk form, the second is ferromagnetic. The objective of the measurement was to check if the cationic segregation (La/Sr) effectively induced a (AF / F) stacking. The reflectivity on one of these systems is presented on Figure 2.5a. Around the angle $\theta = 1.3°$, a super-structure peak corresponding to the system's periodicity can be observed. The contrast between the 2 reflectivity curves « up » and « down » is characteristic of the in-depth magnetization profile. In order to model the reflectivity curves, it is only necessary to introduce a small modulation of the magnetization in the system (Figure 2.5b): the cationic segregation does not lead to a clear magnetic segregation. The magnetization modulation is only 25% between the two types of layers. This can be accounted for by a limited efficiency of the chemical segregation.
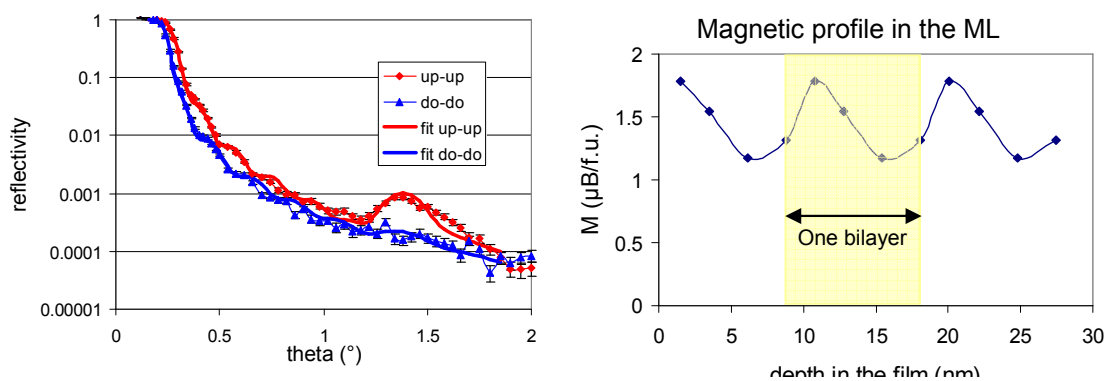
Figure 2.5.: *(a) Reflectivity on a super-lattice* $[(LaMnO_3)_a/(SrMnO_3)_b]_n$ *with a bilayer thickness of 9 nm. (b) Magnetic profile in the super-lattice.*

2.2.1.4. Supermirrors

For technical purposes it is interesting to build systems exhibiting an artificially large optical index [52]. One can can build such a structure by stacking periodic multilayers with an almost continuous variation of the period. In such a system, if the periodicity range is well chosen, a large number of Bragg peaks follow the total reflectivity plateau. Since the periodicity of the multilayer is varying continuously, all these Bragg peaks add constructively. Using this technique it is possible to enhance the length of the total reflection plateau by a factor 3 to 4 (up to 6 in technological demonstrators). Such mirrors are now widely used for neutron guides and for polarization devices. Figure 2.6 gives an example of a polarising mirror.

2.2.2. Magnetic single layers

Even though most of the studies are performed on super-lattices (usually for scattered intensity reasons), the magnetization of very thin systems can also be probed. The advantage of studying simple systems is that much more detailed information can be obtained since the signal is not blurred by interface roughness or thickness fluctuations.
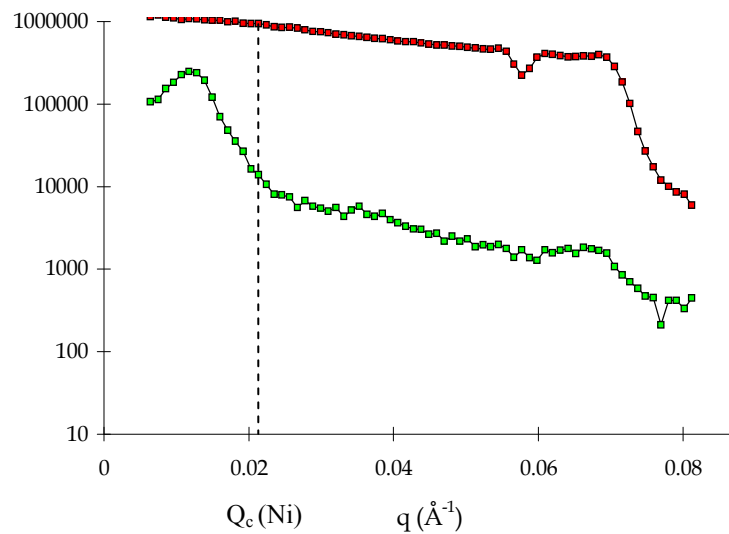
Figure 2.6.: *Reflectivity of a polarizing super-mirror produced at the Paul Scherrer Institute.*

2.2.2.1. Metal trilayer

We present here the example of the study of a coupled FeCo/Mn/FeCo trilayer system produced by S. Nerger at the Forschung Zentrum Jülich [53] . The structure of the sample is shown on Fig. 2.7a. The "active" region is formed by the layers FeCo/Mn/FeCo. The Ag layer is used to promote an epitaxial growth of the system. The Au layer is a simple protective capping. The presented system is $Fe_{0.5}Co_{0.5}/Mn(8\text{Å})/Fe_{0.5}Co_{0.5}$. The specificity of this system is that the magnetic couplings between Fe and Mn, and Co and Mn are of opposite sign. Ab initio calculation predicted that in such a system, contrary to a pure Fe/Mn interface, a complex magnetic behavior of the Mn layer arises. A first measurement (not shown) was performed in a saturating field of $1T$. A numerical modeling of the data shows that the magnetic moment in the $Fe_{0.5}Co_{0.5}$ layers is $2.4\mu_B/atom$ (as in bulk materials). A net magnetic moment of $0.8\mu_B/atom$ in Mn is also observed. This induced magnetization in the Mn layer was theoretically predicted for FeCo alloys by the ab-initio calculations [54]. Note that similar measurements in Fe/Mn/Fe trilayers [55] did not show any magnetization in Mn, also in agreement with ab-initio calculations.

The applied field was then decreased down to $1.2\,mT$. The reflectivity was remeasured. In these conditions a large spin-flip signal is observed (Fig. 2.7b, yellow curve). The reflectivity data was fitted by letting the magnetization directions vary. The best adjustment was obtained when the magnetization of the FeCo layers make an angle of 45° with respect to the applied field. The two magnetic layers make an angle of 90° with respect to each other; we have a quadratic coupling (Fig. 2.7).

2.2.2.2. Exchange bias - spin-valves

The magnetic thin film system which has enjoyed the most popularity until now is the spin-valve. It consists of a stack of two magnetic layers separated by a non magnetic spacer. The electrical resistance of the system depends on the relative orientation of the
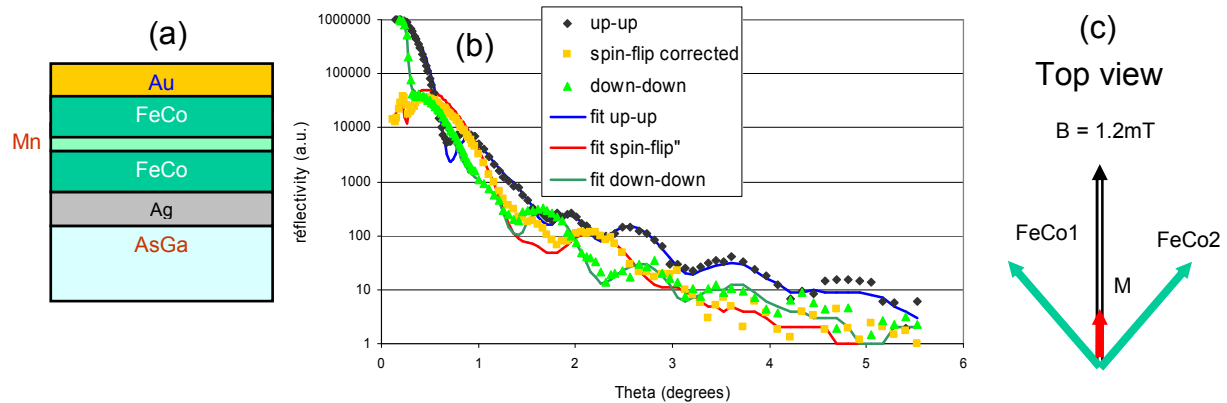
Figure 2.7.: *(a) Trilayer system FeCo(8nm)/Mn(0.8nm)/FeCo(5nm). (b) Reflectivity in the remanent state (1.2mT). (c) Magnetic configuration as deduced from the fit performed by S. Nerger [53].*

magnetizations of the two layers. In industrial systems, one of the magnetic layers is pinned by a coupling with an anti-ferromagnetic material through the so-called exchange-bias mechanism. The materials which are used in such structures are numerous : Co, Fe, Ni, $NiFe$, Fe_3O_4, $CoFe_2O_4$, $LaSrMnO_3$ for ferromagnetic layers; Cu, Cr, V, Al_2O_3, HfO_2, $SrTiO_3$ for the spacer layers; $FeMn$, $IrMn$, CoO, NiO, $BiFeO_3$, $Co/Ru/Co$ for the anti-ferromagnetic exchange bias layer.

Such spin valve systems have been extensively characterized [56, 57, 58, 59] and are now well understood. However, the microscopic understanding of exchange bias has been a long standing problem for decades now. A wealth of literature is being produced on various systems [60, 61, 62, 63, 64]. It appears that the exchange bias mechanism combines very subtle effects. The reversal process of the coupled magnetic layer has been studied in detail. Since the origin of the phenomenon is often linked to micromagnetic problems, reflectivity studies are often complemented with off-specular scattering which probe the underlying micromagnetic structures. This technique is described in the following.

2.2.2.3. Magnetic oxides

Polarized neutron reflectivity has also been used to probe the magnetism of oxide thin films (manganites [86, 87] or Fe_3O_4 [88]). For example, the hysteresis cycle of $La_{0.7}Sr_{0.3}MnO_3$ thin films shows a region with a low coercivity on which is superimposed a contribution which requires $0.3T$ to be saturated. This suggests that the films are not homogeneous and that they are composed of several phases having different coercivities. Neutron reflectivity measurements were performed on single $La_{0.7}Sr_{0.3}MnO_3$ thin films in order to probe the magnetization profiles through the depth of the films as a function of the temperature. Figure 2.8a shows the reflectivity on a $16\,nm$ $La_{0.7}Sr_{0.3}MnO_3$. Modeling using a homogeneous magnetic layer does not provide satisfactory fits. In order to quantitatively model the data, it is necessary to introduce a model taking into account different magnetizations at the interfaces. We thus consider a 3 layers model with magnetizations M_1, M_2 and M_3 in the depth of the films (Fig. 2.8b). Figure 2.8c shows the variations of the magnetizations M_1, M_2 and M_3 as a function of the temperature. One can note that

the interface magnetization is reduced by 25 to 30%.
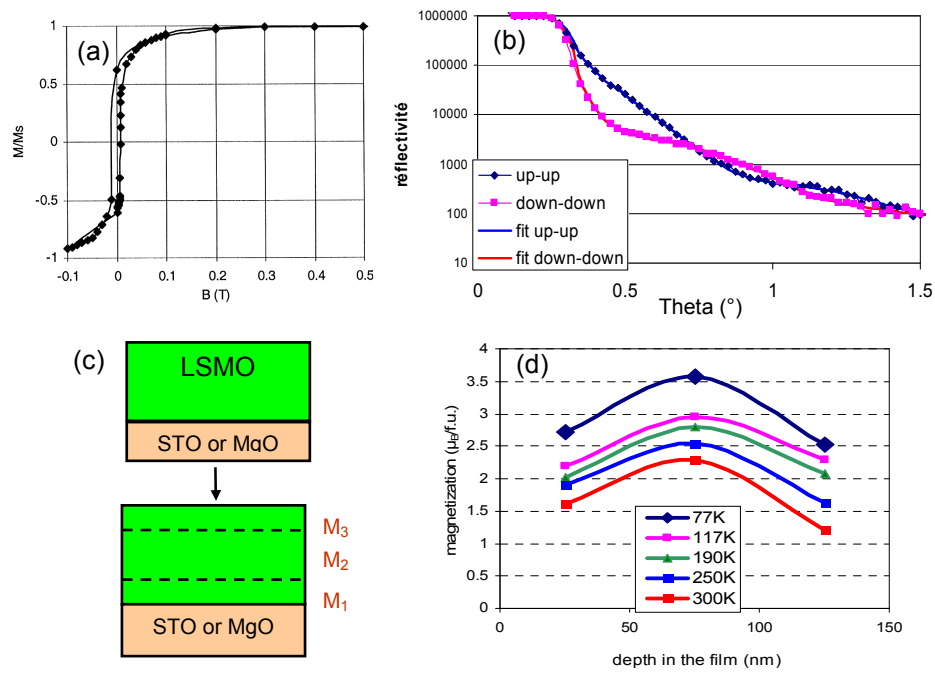
Figure 2.8.: *(a) Hysteresis cycle of a manganite thin film. (b) Reflectivity of a $La_{0.7}Sr_{0.3}MnO_3$ (16nm) film deposited on $SrTiO_3$. (c) Modeling of the system: (top) perfect system, (bottom) more realistic 3 layers model. (d) Magnetization profiles as a function of the temperature for the system $La_{0.7}Sr_{0.3}MnO_3$ (16nm)//$SrTiO_3$.*

2. Specular reflectivity

3. Off-specular scattering

3.1. Principle

In the case of specular reflectivity, the scattering vector $\mathbf{Q}$ is perpendicular to the sample surface and thus one only probes the structure of the sample along its depth. All the structures in the thin film plane are averaged out. However, in a number of situations, it can be of interest to probe in-plane structures. This is for example the case when there is formation of magnetic domains in the films or if the surface is rough. In such cases, it is interesting to look at the scattered intensities around the specular reflection direction, that is for $\theta_r \neq \theta_i$. In this geometry (Fig. 3.1), a small in-plane component Q_x of the scattering wave-vector appears. Note that at grazing incidence this in-plane component Q_x of the scattering vector is very small, of the order of $0.1 - 10\,\mu m^{-1}$. Thus, in this scattering geometry, one will be mostly sensitive to in-plane lateral structures with characteristic sizes ranging from $50\mu m$ down to $0.5\mu m$. The upper limit is set by the resolution of the spectrometer and the size of the direct beam. The lower limit is set by the available neutron flux. These sizes actually correspond to typical sizes of micro-magnetic domain structures. Thus magnetic off-specular is mostly used to probe such problems. Off-specular measurements are usually performed by using a position sensitive detector set after the sample and by measuring the scattering on the detector as a function of the incidence angle. A 2D mapping in the reciprocal space (Q_x, Q_z) can thus be obtained. The intensity scattered along the Q_z direction contains information about the depth structure of the system, the intensity scattered along the Q_x direction contains information about in-plane micrometric structures.

$$Q_x = \frac{2\pi}{\lambda}\left(\cos\theta_f - \cos\theta_i\right)$$

$$Q_z = \frac{2\pi}{\lambda}\left(\sin\theta_f + \sin\theta_i\right)$$
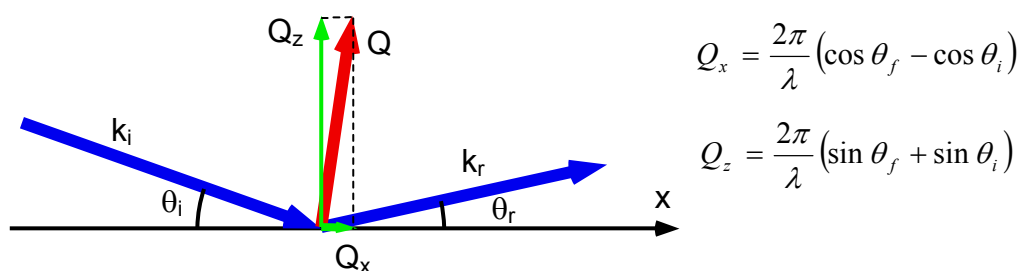
Figure 3.1.: *Off-specular scattering geometry. The scattering vector $\mathbf{Q}$ is not perpendicular to the thin film plane. There is a small Q_x component in the thin film plane.*

The pioneering work in the field of off-specular scattering was presented in the early 1990s [89]. For flux reasons, until now, most of these studies have been performed on multilayer systems. Figure 3.2 presents an example of the off-specular scattering from a $[Co/Cu]_{50}$ multilayer.

The diffuse signal has been measured as a function of Q_x and Q_z. On Fig. 3.2a and 3.2b, one observes the structural correlation peak [001] corresponding to the chemical

3. Off-specular scattering
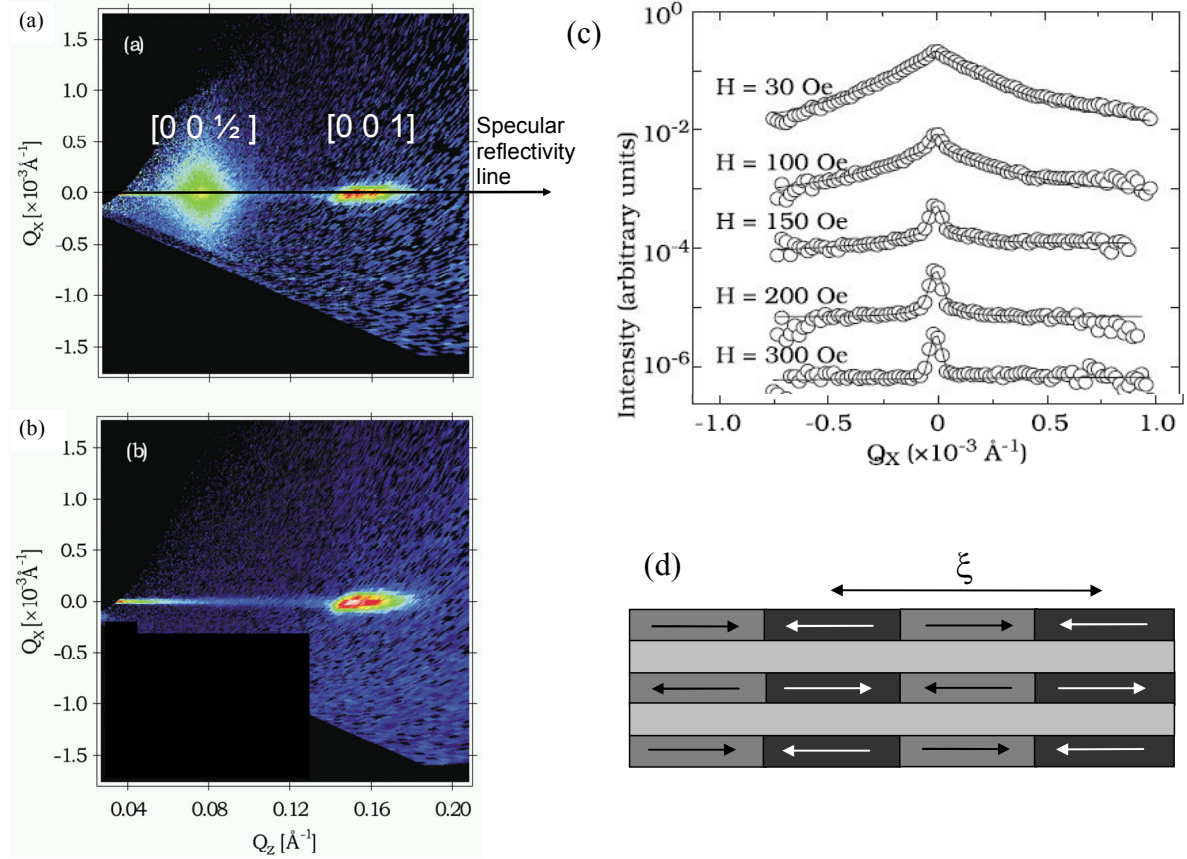
Figure 3.2.: $[Co(2nm)/Cu(2nm)]_{50}$ *multilayers (adapted from Langridge et al [4]). (a) Diffuse scattering at H = 0. One observes a strong diffuse signal at the AF position. (b) Diffuse scattering in a saturating field. The AF peak has disappeared. (c) Evolution of the AF peak as a function of the applied field (cut along $Q_z = 0.75nm^{-1}$). (d) Magnetic coupling between the layers. x is the lateral correlation length between magnetic domains. The Co layers are locally coupled AF but there is a strong disorder within each Co layer.*

periodicity. At remanence, a strong diffuse scattering peak is observed at the position $[0\ 0\ \frac{1}{2}]$. Since the magnetic diffuse scattering is localized around the position $[0\ 0\ \frac{1}{2}]$, it is possible to say that the Co layers are globally anti-ferromagnetically coupled along the thickness of the layer. However, since there is a strong diffuse scattering, it is also possible to say that there exists a significant magnetic disorder in the plane of the Co layers. The width of the diffuse scattering peak around the position $[0\ 0\ \frac{1}{2}]$ (Fig. 3.2c) is inversely proportional to the magnetic domain size and gives an estimate of the mean magnetic domain size which ranges from $1\mu m$ at remanence (30G) and grows to $6\mu m$ at $250G$.

Magnetic off-specular scattering has been mostly used to probe the magnetic domains sizes in multilayers. Detailed quantitative analysis of the magnetic off-specular scattering can be performed [21]. The effect of the micro-magnetic structure can then be correlated with other properties such as the magneto-crystalline anisotropy (in Fe/Cr superlattice [90]) or the magneto-resistive effect (in Fe/Cr [91] or Co/Cu [92] superlattices). The formation of micromagnetic structures is very important with respect to the transport

properties in magnetic sensors. The signal-to-noise ratio of Giant Magneto Resistive systems is very sensitive to the micromagnetic structure [56]. Off-specular studies are also used to complement studies on exchange bias systems: Co/CoO [93], $Ir_{20}Mn_{80}/Co_{80}Fe_{20}$ [94]. Off-specular scattering has also been used to study the problem of the reversal process in neutron polarizing super-mirrors [95] (see below). In some special cases, it has been shown that it is also possible to probe single interfaces (Fe/Cr/Fe trilayer [96] or waveguide structures [97], see below).

Off-specular has also been used to study patterned or self-organized micro-structures [98, 99, 100, 101]. In a number of studies, the influence of patterning on the exchange bias has been probed [102, 103, 104]. These studies are of interest when the magnetic heterostructures are to be integrated in large scale micro-circuits (typically for Magnetic RAMs.)

3.2. Examples

The study of the off-specular scattering was partly part of my PhD thesis which I developed for model systems such as gratings.

I am presenting here two examples of studies of off-specular scattering on continuous layers. The first example is a study on a super-lattice system. The large number of layers is sufficient to give rise to a measurable signal. The second example is somewhat more specific since it is one of the rare case in which the off-specular scattering from a single interface can be measured .

3.2.1. Magnetization process in polarizing neutron supermirrors

These studies were partly performed on the reflectometer PRISM at the LLB but were further complemented by U. Rücker by more extensive measurements on the spectrometer HADAS at the Forschung Zentrum Jülich. The presented data are the data measured on the HADAS spectrometer.

Neutron polarizing supermirrors consist of a stack of ferromagnetic and non-magnetic layers with a gradient in the layers thickness (see 2.2.1.4). The mirrors which have been studied here were commercial mirrors produced by Swiss Neutronics. They are produced in such a way that residual stress induce a well define magnetic anisotropy direction so that square hysteresis loops are obtained. This permits to maintain a high negative magnetization even in small positive fields. This makes them suitable for use as switchable polarizers: the mirrors are placed in a small magnetic guide field. Their magnetization can be reversed by simply applying a magnetic field pulse either positive of negative. They can thus reflect either "up" or "down" neutrons. Spin flippers are not needed anymore. However, in order to have a good polarization efficiency, it is necessary that the remanent magnetization is very high. Figure 3.3 shows the evolution of the reflectivity of the mirrors as a function of the applied field. The mirrors are first saturated with a negative field of $-0.5T$. For very low fields ($H = 1\,mT$), the magnetization is unchanged and still anti-parallel to the guide field. Thus the mirror reflects only "down" neutrons (red dots). For incidence angles between 10 and 20 mrad, the flipping ratio between "down" and "up" neutrons is very high, of the order of 100. When the field is increased, $H = 3.8\,mT$, the thinner layers start to reverse and some "up" neutrons start to be reflected (around

3. Off-specular scattering

$\theta_i = 20\,mrad$). When the field H reaches $5.6\,mT$, most of the layers have flipped except the thicker ones, corresponding to the region $\theta_i < 10\,mrad$. For a field of $25\,mT$, all the layers have flipped.
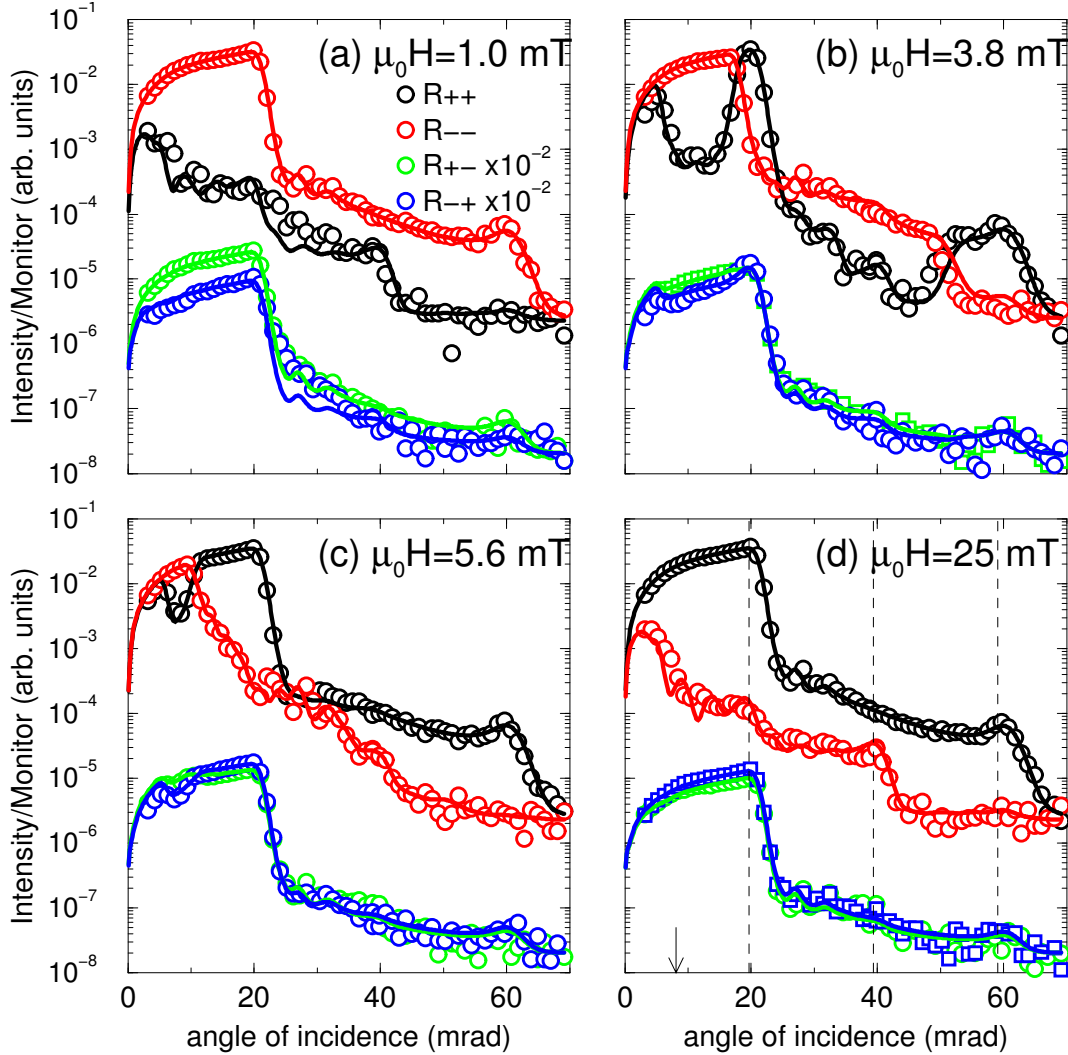
Figure 3.3.: *Specular reflectivity on polarizing supermirrors as a function of the applied field after having saturated them in a -0.5T field. Fits performed by E. Kentzinger [105].*

In order to have a more detailed insight in the reversal process in this system, off-specular scattering has also been measured as a function of the applied magnetic field. The data are presented on Figure 3.4. The data are represented in the (θ_i, θ_f) space which are the "natural" instrumental coordinates. In this representation, the diagonal $\theta_i = \theta_f$ corresponds to the specular reflectivity. The off-diagonal signal corresponds to the off-specular scattering.

At remanence, some off-specular signal is observed in the I^{--} channel. It corresponds to a local disorder of the magnetic layers, which remains however rather weak. At $3.8\,mT$, in the I^{++} channel, around the diffraction peak from the thinnest layers which have flipped, a Bragg sheet appears at $\theta_i + \theta_f = 40\,mrad$. The fact that the Bragg sheet is very
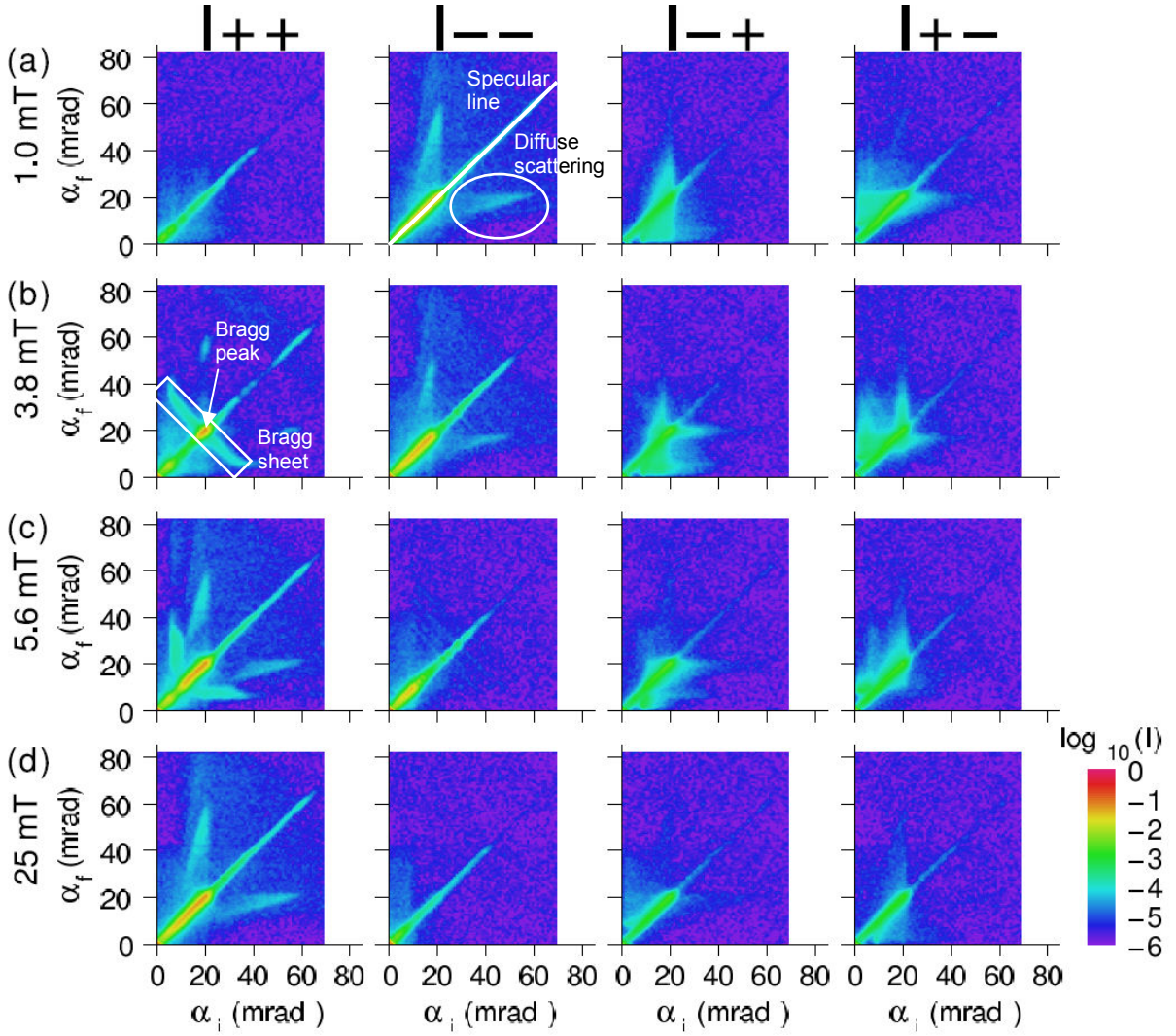
Figure 3.4.: *Spin resolved reflectivity and off-specular scattering measured after saturation of the sample in a negative field at four applied fields: H = 1 mT (a), 3.8 mT (b), 5.6 mT (c) and 25 mT (d). Measurements performed by U. Rücker on HADAS.*

intense indicates that the flipping of these layers is rather disordered. When the field is increased further to 5.6mT, the Bragg sheet from the thinnest layers disappear meaning that the magnetic domains are getting fully aligned. In parallel, diffuse scattering appears corresponding to thicker layers which have flipped. One does not observe anymore a nice Bragg sheet because of refraction effects. In higher fields ($25mT$), most of the magnetic domains have been saturated and the diffuse scattering has almost disappeared. The diffuse scattering in the spin-flip channels originates from fluctuations of the magnetization direction with respect to the applied field. It is not arranged along Bragg sheets meaning that these fluctuations are not vertically correlated. A quantitative analysis gives an average in-plane correlation length of $200\,nm$.

A quantitative detailed discussion of this study can be found in [105].

3.2.2. Neutron waveguides

In order to produce submicron neutron beams [106], together with S. Kozhevnikov from JINR Dubna, we are studying neutron magnetic wave-guides. We produce neutron wave-guides with the following typical tri-layer structure: Py(10-20nm)/Ti(10-80nm)/Py(10-50nm)//glass (Fig 3.5a). The top permalloy layer acts as the coupling layer with the incident beam, the Ti layer which has a low optical index acts as the guiding layer and the bottom layer acts as the reflecting layer (see Fig. 3.5b).
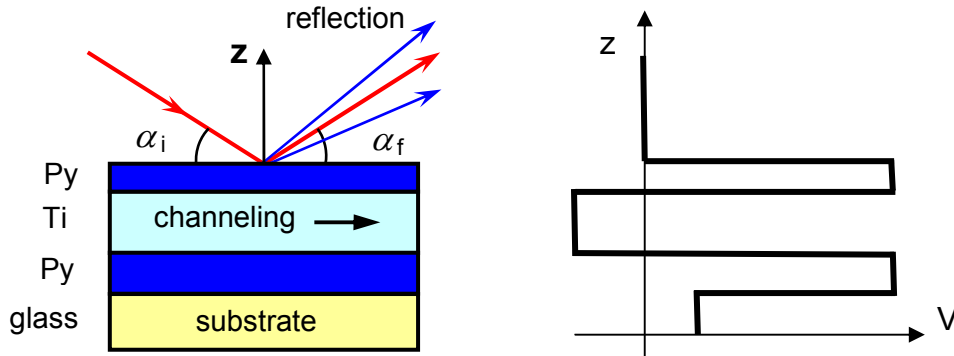
Figure 3.5.: *(a) Reflection from a magnetic neutron waveguide. (b) Optical index profile through the wave-guide structure.*

In such a wave-guide structure, the neutron can be trapped and guided in the Ti layer. The neutron wave function density for the "up" spin state is shown in Fig. 3.6 as a function of the sample depth $z(\text{Å})$ and the incident angle θ_i (mrad). In the Ti guiding layer there are 3 resonance states (order $m = 1, 2, 3$) in the total reflection region. The zero order resonance $m = 0$ is absent for this system. It can however be observed that the neutron wave function density can be enhanced in the guiding Ti layer by a factor 10 to 30. This localization of the wave-function for some incidence angles corresponds to an efficient guiding of the neutron in the Ti channel.
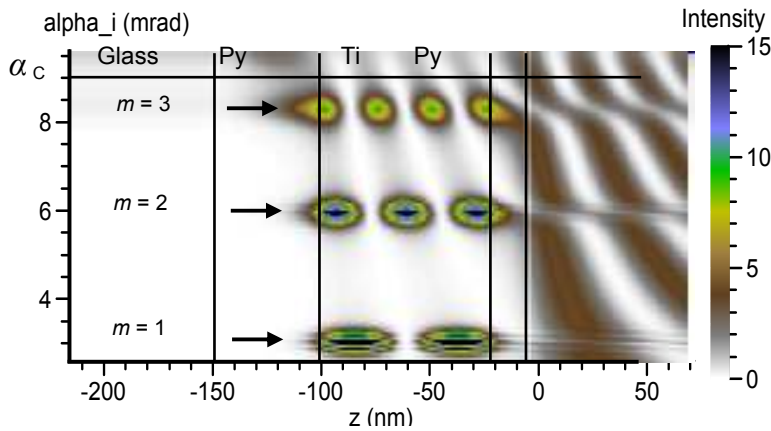
Figure 3.6.: *Wave function density inside the waveguide structure versus the incidence angle θ_i and the sample depth z (calculated using SimulReflec). The Ti guiding layer is 80 nm thick.*

The magnetic reflection of the waveguide has been measured in a saturating field of $100\,G$ and at remanence in $1\,G$ (see Fig. 3.7a and b). At the resonance conditions, one observes marked dips in the total reflection (the resonances modes $m = 1, 2, 3$ are indicated by arrows). In the saturating field (Fig. 3.7a) the magnetic Py layers are collinear and no spin-flip signal is observed. The large resonance dips (10-15%) cannot be accounted for by a regular reflectivity calculation. They correspond to the guiding of neutrons in the Ti layer over macroscopic distances (a few mm) [109]. The diffuse off-specular scattering at one resonance position only represents 10^{-2} of the specular signal and cannot account for the dips. In the remanent state, the magnetization is not collinear with the polarization. The spin-flip signal is strongly enhanced at the resonance position (factor 10).
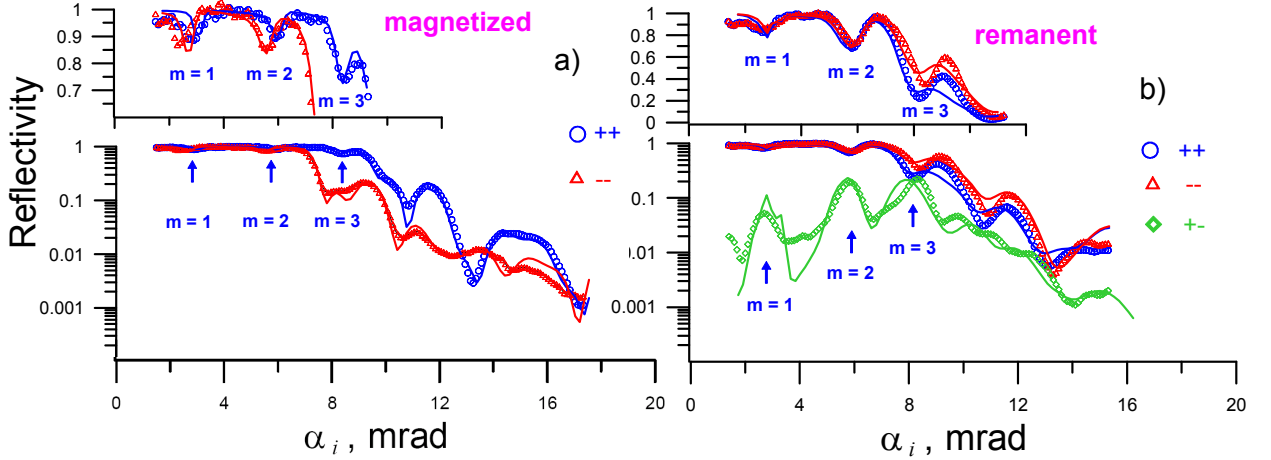
Figure 3.7.: *Specular reflectivity for the waveguide Py(20nm)/ Ti(80)/Py(50)//glass (points are experiment, lines are fit, insets are linear scale for total reflection): a) collinear; b) non-collinear.*

Off-specular scattering in the saturated state is presented in Fig. 3.8 in the axis coordinates (θ_i, θ_f). The diagonal $\theta_i = \theta_f$ corresponds to the specular reflectivity. Along the lines $\theta_i = Const$ and $\theta_f = Const$, one can observe the large off-specular scattering corresponding to the resonance modes ($m = 1, 2, 3$). The signal has been modeled using the program *sdms* [110, 111] based on the DWBA approximation [112]. It is possible to qualitatively account for the data by describing the system with magnetically collinear homogeneous layers (see Fig. 3.8). The shape and position of the diffuse scattering due to the guide effects (along the white lines) are easy to reproduce: it is simply necessary to introduce an in-plane roughness correlation length of the order of $100\,\mu m$. It is thus possible to reproduce the spots of enhanced intensity corresponding to the intersections of 2 resonant modes.

With these measurements, we show: (i) neutron resonance states in magnetic neutron waveguides lead to enhanced off-specular scattering up to 10^{-2}; (ii) the amplitude of resonances dips in the total reflection region (10-15%) mainly depends on wave guiding effect in Ti guiding layer and only a negligible part is connected to off-specular reflection; (iii) large spin-flip off-specular scattering can be observed without any micro-magnetic structure. This one of the rare systems in which measurable off-specular scattering from a single interface can be observed. More details can be found in [97].
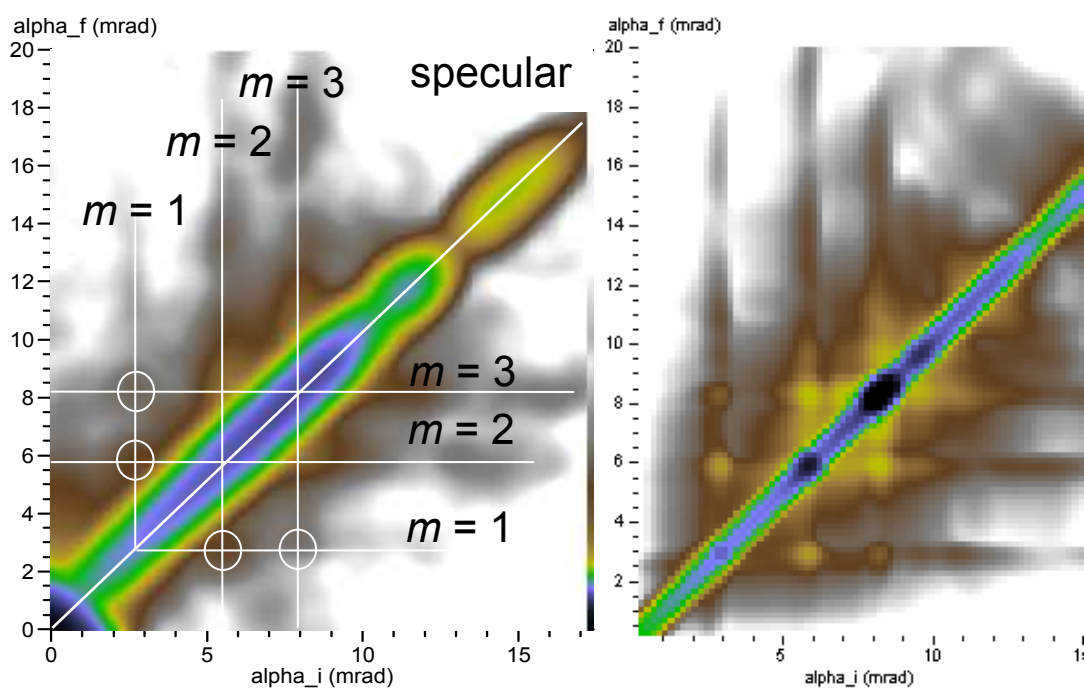
Figure 3.8.: *Experimental off-specular scattering (Up-Up) in the saturated state. (left) experiment – (right) simulation. (data measured on the spectrometer HADAS [108] at the FZ Jülich).*

4. Small angle scattering

One of the most mainstream technique used in neutron scattering is Small Angle Scattering. It is mostly used for polymer science and soft matter studies because of the contrast variation possibilities. It can also be used to perform studies on magnetic materials and take benefit of the strong magnetic scattering. This allows to probe nanometric properties of magnetic crystals.

4.1. Principles

The neutron-matter interaction potential is given by two main contributions, the neutron/nucleus and the neutron/magnetic induction interactions:

$$V = \frac{2\pi\hbar^2}{m} b_n \delta(r) \qquad and \quad V_M = -\mu \cdot B(r)$$

Since we are considering scattering at small scattering wave-vectors, we are not sensitive to the atomic details of the matter and the optical approximation can be applied. It is thus possible to define a scattering length density as:

$$b_{vol} = \frac{1}{V} \sum b_i$$

where the volume V over which the average is taken is of the order of a few nm^{-3}.
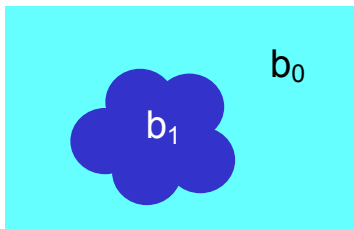
Figure 4.1.: *Object of scattering length b_1 in a matrix or solvent of scattering length b_0.*

If one considers nano-objects in a matrix (Fig. 4.1), SANS measures the form factor of the object which is the Fourier transform of the scattering length density contrast between the scattering object and its matrix $\Delta b = b_1 - b_0$. The measured intensity is the form factor squared:

$$I(Q) = |FT(\Delta b)|^2 = |F(Q)|^2$$

For the usual wavelengths and collimations used on small angle scattering spectrometers, the accessible Q range is $0.02 - 2nm^{-1}$ which corresponds to correlation lengths in real space ranging from 3 to $300nm$.

4. Small angle scattering

In the case of magnetic systems, the interaction is limited to the component of the magnetization perpendicular to the scattering wave-vector Q. The interaction potential has thus the form $F_M(Q) \sin\alpha$ where $F_M = FT(\triangle b_m)$ is the magnetic form factor and α is the angle between the magnetization and the scattering wave-vector.

With polarized neutrons one can measure two scattered intensities I^+ and I^- depending on the orientation of the neutrons polarization with respect to the applied field:

$$I^+(Q) = |F_N + F_M \sin\alpha|^2$$
$$I^+(Q) = |F_N - F_M \sin\alpha|^2$$

These intensities can be combined to provide the following relations:

$$(I^+ + I^-)/2 = F_N^2 + F_M^2 \sin^2\alpha$$
$$I^+ - I^- = 4F_N F_M \sin\alpha$$

When performing a polarized SANS measurement, it is possible to consider 2 geometries. The first possibility is to apply a field parallel to the neutron propagation direction (Fig. 4.2a). If in this situation the magnetization is parallel to the applied field, the scattering will be isotropic. The second possibility is to apply a magnetic field perpendicular to the neutron propagation direction (Fig. 4.2b). In this case, the scattered intensity is modulated by a $\sin^2\alpha$ factor (Fig. 4.2c). The magnetic scattered intensity is maximum in the direction perpendicular to the applied field ($\alpha = 90°$).
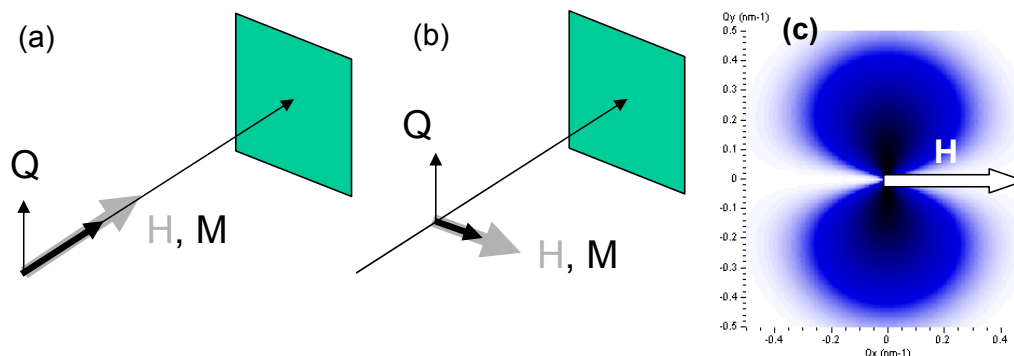
Figure 4.2.: *Different configurations for polarized small angle scattering. The field can be applied longitudinal (a) or transverse (b). For a transverse applied field, the intensity is modulated by a $\sin^2\alpha$ factor. The maximum scattered intensity is obtained in the direction perpendicular to the field (c).*

Some of the key advantages of SANS are that: (i) there is a strong scattering difference between hydrogen and deuterium which allows to perform selective labeling (of surfactants for example); (ii) the magnetic scattering is very large which make quantitative measurements possible; (iii) Neutron are barely absorbed, which permits to look at bulk samples and to use complex sample environments (low temperatures, high magnetic fields).

In the case of small magnetic particles, it is possible to study the detailed structure of the particles. We illustrate this point in the case of oxidized Co particles coated with a surfactant in colloidal suspension in a toluene solution (Fig. 4.3). Polarized SANS measurements in H and D-toluene solvent can provide the layered structures of these particles with great details [27] (Fig. 4.3).
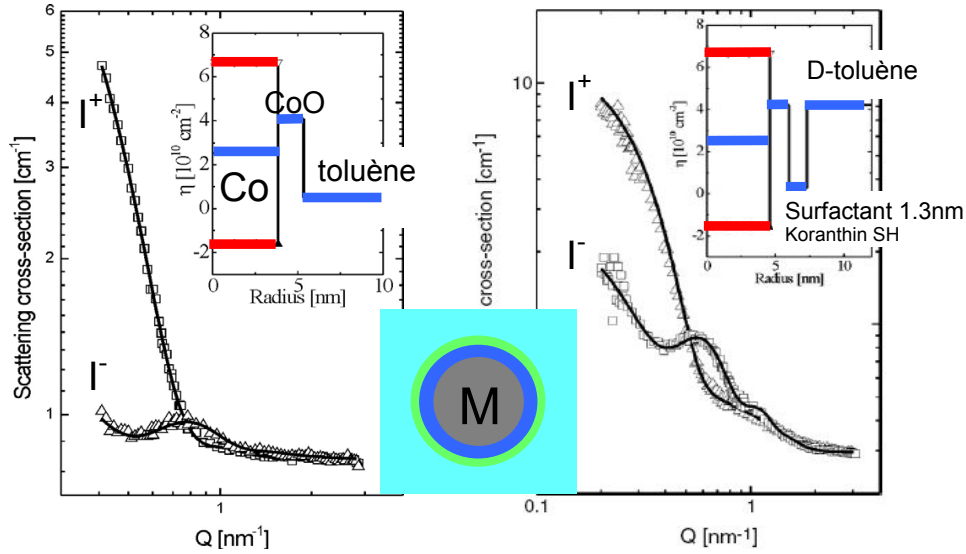
Figure 4.3.: *Magnetic Co particle with a magnetic core (gray), an oxidized surface (blue), a surfactant layer (green), floating in solvent (blue). It is possible to determine the thickness and the scattering lengths of these different layers by PSANS. (Adapted from A. Wiedenmann et al [27]).*

In the case of dense packing of nano-objects, the scattering becomes sensitive to the position correlation between the particles. The measured intensity is given by:

$$I(Q) = |F(Q)|^2 \cdot S(Q)$$

where $S(Q)$ is the structure factor which characterizes the correlations between the particle positions.

The system can be more or less well packed which leads to structure factors which are more or less well defined (see Fig. 4.4). In practice, it is difficult to observe any correlation peaks in the structure factor beyond the second nearest neighbour.

We can illustrate the effect on SANS of dense packing of nanoparticles in the case of an assembly of Co nanoparticles. Figure 4.5(top) shows the ordering of magnetite nanoparticles on a surface with a ZFC and FC procedure; Figure 4.5(bottom) shows the ordering of magnetite nanoparticles in bulk in ZFC and FC procedure [113].

In the above summary, I have presented examples of small angle scattering on well defined objects such as nano-spheres. More generally, it is possible to perform SANS studies to characterize magnetic critical scattering [114], the penetration of magnetic flux in superconductors [115], or any other type of magnetic correlations taking place at a nanometric scale.

The study of the magnetic properties of solid materials is much better performed on single crystals. Past experiences have shown that the use of powders led to very large parasitic SANS signals. In order to perform clean studies, it is thus necessary to use single crystals. This is not necessarily a limitation since rather small crystals are required (a few mm^3). In the following section, I present an example of study of a nanometric phase separation in a magnetic single crystal.
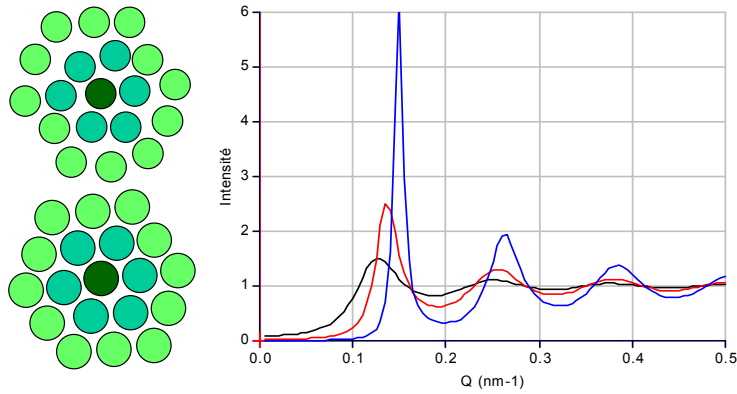
Figure 4.4.: *Dense packing of particles. The system can be more or less well packed which leads to different structure factors (packing density of 0.3, 0.45, 0.6).*
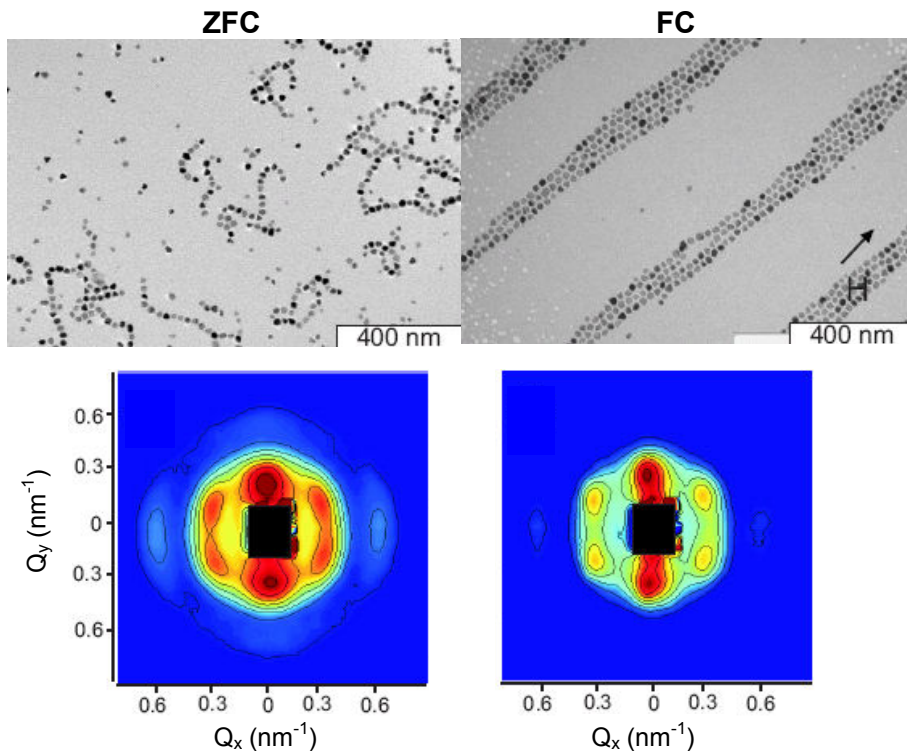
Figure 4.5.: *(top) Ordering of magnetite nanoparticles on a surface with a ZFC and FC procedure; (bottom) ordering of magnetite nanoparticles in bulk in ZFC and FC procedure (adapted from [113]).*

4.2. Magnetic filaments in $Pr_{0.67}Ca_{0.33}MnO_3$ crystals - hopping exchange

Manganites ($A_xB_{1-x}MnO_3$) (where A is a rare earth La^{3+}, Ba^{3+}, Pr^{3+} ... and B = Ca^{2+}, Sr^{2+}...) present a broad variety of phases in which the structural, magnetic

and transport properties are intimately linked. The magnetism is the result of a spin interaction due to the overlap of the electronic wave functions of the different atoms. In manganese oxides, where the magnetic Mn ions are separated by oxygen ions, the magnetic exchange is mediated by the overlap of the *2p* orbitals of the O^{2-} ions and the *3d* orbitals of the $Mn^{3+/4+}$ ions. The nature of this interaction called *super-exchange* (SE) depends on the orbitals in play. The SE coupling is in general anti-ferromagnetic. When the electrons can delocalize over at least two magnetic ions, a ferromagnetic exchange interaction appear called *Double Exchange* (DE) (see Figure 4.6). In doped manganites, this exchange is a mixture of SE and DE because of the different configurations of the electronic orbitals. These 2 antagonist interactions (ferromagnetic versus anti-ferromagnetic) can give rise to a magnetic phase separation [116].
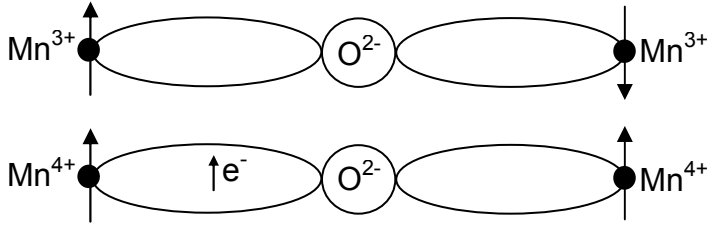
Figure 4.6.: *(top)* Super-exchange*: an anti-ferromagnetic coupling is created by direct overlap of the* Mn-O-Mn *orbitals. (bottom)* Double exchange*: an electron is delocalized over the two Mn ions and gives rise to an effective ferromagnetic coupling.*

The $Pr_{0.67}Ca_{0.33}MnO_3$ compound has a ferromagnetic transition below which the application of a magnetic field produces a first order transition from an insulating to a conducting state [117]. In this induced metallic-like state, the magnetization relaxes with time, leading to impressive resistive transitions [118]. This can be understood in a percolation picture where ferromagnetic regions are thermally activated into an antiferromagnetic insulating state. When the last percolation path breaks, the resistivity suddenly jumps to immeasurably large values. In order to finely characterize the phase separation in $Pr_{0.67}Ca_{0.33}MnO_3$ we have carried out Polarized Small Angle Neutron Scattering (PSANS) under applied fields along with electrical transport and magnetization measurements. The results presented here were obtained on a $1 \times 1 \times 3mm^3$ single crystal. The PSANS measurements were carried out at the ORPHEE reactor in Saclay (France) on the spectrometer PAPYRUS.

Unlike bulk measurements which may be interpreted in a phase separation framework because signals do not follow a usual law, the SANS intensity only appears when nanometer size objects are present. Its angular dependence gives the Fourier transform of chemical and magnetic heterogeneities with sizes ranging from 1 nm to 100 nm. As shown on the typical spectrum in the inset of Fig. 4.7, the SANS signal is characteristic of magnetic scattering with a contribution in $sin^2\alpha$ with respect to the direction of the applied field. Hence, the scattering entities are purely magnetic. At 4.2K, the measurements show that the scattering follows a power law q^{-n} with $1.6 < n < 1.7$ (see Fig. 4.7). This fractionnary exponent corresponds to fractal dimensions identical to the one observed in dilute polymer solution $(q^{-5/3})$. This parallel suggests that the phase separation observed in $Pr_{0.67}Ca_{0.33}MnO_3$ could be of filamentary type. In order to validate this hypothesis, we
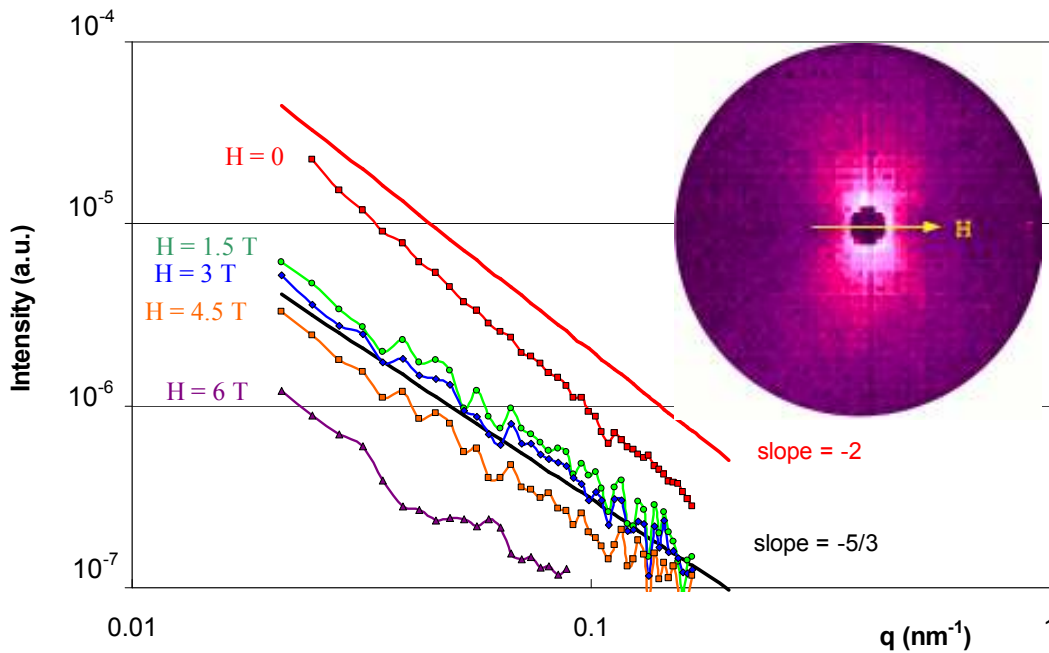
Figure 4.7.: *Magnetic SANS intensity from a $Pr_{0.67}Ca_{0.33}MnO_3$ single crystal, for a set of increasing fields from 0 to 6 T after zero field cooling to 4.2K. The two straight lines are power laws with exponents –2 and –5/3 (the latter line separates spectra measured in the insulating and metallic states). Inset: Typical PSANS 2D spectrum (log scale) showing the $\sin^2\alpha$ contribution of the magnetic scattering (the central black spot is due to the direct beam catcher).*

have modeled in a self consistent way the magnetic and transport properties which are intimately linked.

In the $Pr_{0.67}Ca_{0.33}MnO_3$ compound, the charge carriers are localized by a random magnetic potential. The electronic conduction takes place by random hopping of the charge carriers from one Mn ion to a neighboring site. This type of conduction is described by the *variable range hopping*. We propose a model in which after each electronic hop, the electrons transfer their magnetic moment to the new site and align with the Mn^{4+} ion magnetic moment. In the process, the total magnetic moment of the electron and the Mn ion is preserved (see Fig. 4.8).
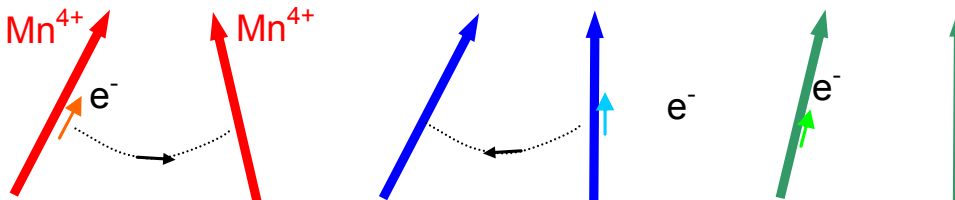
Figure 4.8.: *Hopping magnetic exchange: after each electronic hop, the magnetic moments of the Mn ions get better and better aligned.*

Because hopping happens preferentially between ions of similar spin direction, the ex-

change becomes stronger as spins are more closely aligned, which naturally results in a tendency to phase segregate. Indeed, once one Mn has in its vicinity another Mn with parallel spin, the hopping probability between this pair is overwhelmingly large and the ferromagnetic interaction will occur exclusively between these two moments. The remaining surrounding Mn ions interact only via SE. In order to demonstrate that this model leads to a filamentary phase segregation, Michel Viret has carried out Monte Carlo simulations treating transport and magnetism in a self-consistent manner (more details can be found in [119]). When hopping is turned on, magnetic filaments containing many parallel spin carriers with an enhanced mobility appear, as shown in Fig. 4.9.

In the zero field-cooled (ZFC) state at $H = 0$, the PSANS intensity can be well fitted with an exponent close to -2 (Fig. 4.7), i.e. a Debye function. This is consistent with previously published SANS data recorded at zero field and interpreted as an average coherence or a *red cabbage structure* [121]. Debye functions being reminiscent of polymer melts, this indicates, in our picture, that the magnetic filaments are entangled and do not self-avoid. This is understandable because a ZFC procedure generates a large density of filaments and a highly resistive state where carriers have to hop further than their nearest neighbors to find states lower in energy. Here, "super-exchange screening" does not work since electrons tunnel over distances longer than the screening length. Hence, Gaussian, entangled, randomly magnetized filaments are generated by a ZFC procedure as shown in Fig. 4.9a. When a field is applied, the filaments with their magnetization parallel to the field grow while others shrink. Within the filaments, mobility is large and carriers proceed by nearest-neighbor-hops, mediating ferromagnetic "hopping exchange". Super-exchange interactions screen the filaments to make them self-avoiding (see Fig. 4.9b) and the measured power laws are around -5/3. This exponent remains unchanged as only the global SANS intensity decreases with field, even when the sample resistance drops by orders of magnitude at 3.9 T. The variation in intensity results from a combination of a reduction in magnetic contrast as the background is forced to become more ferromagnetic and an increase in density due to the growth of the filaments. Complementary magnetization measurements (not shown here) allow us to conclude that the volume fraction of the filamentary phase increases monotonically as the field is raised. This naturally leads to a picture of magnetic filaments existing across the entire range of fields and becoming fainter as the background magnetization increases. At higher fields, the carriers leak out of the filaments into the entire volume (Fig. 4.9c) which is almost fully magnetized, and produces a homogeneous ferromagnetic phase. The percolation at 3.9 T has no SANS signature since nothing dramatic happens for the magnetic configuration.

In conclusion, we propose here that a ferromagnetic interaction due to electron hopping is responsible for the phase separation in resistive manganites. The random walk motion of the charge carriers leads to the appearance of magnetic filaments which were evidenced by neutron scattering in $Pr_{0.67}Ca_{0.33}MnO_3$ single crystals and supported by Monte-Carlo simulations. Further details of this study can be found in [119].
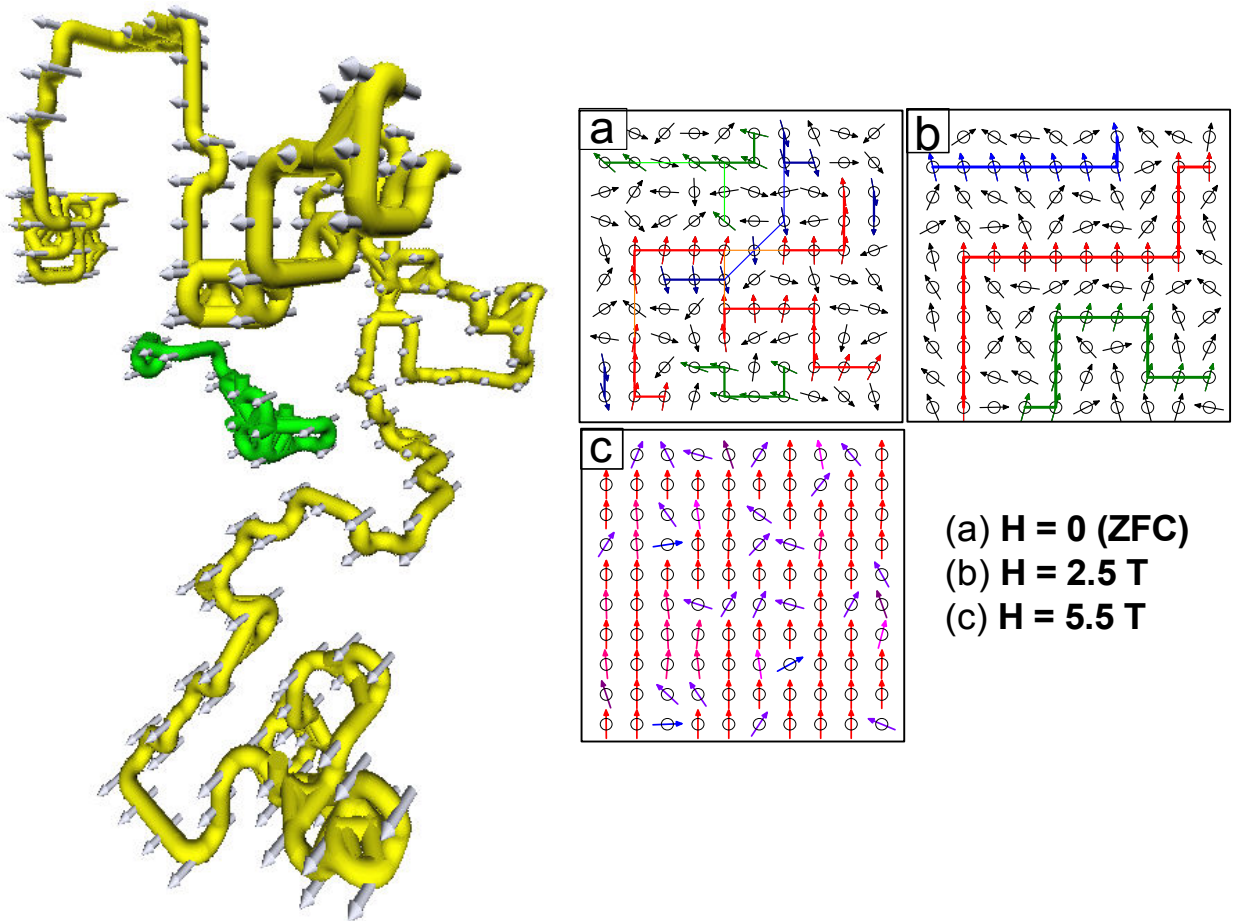
Figure 4.9.: *(left) Magnetic filament obtained by Monte-Carlo simulation (calculation performed by Michel Viret). (Right) Schematics of the evolution of the filamentary phase with the applied field. From a disordered assembly of small filaments after the ZFC procedure, the applied field makes filaments with spins parallel to H grow, and shrinks the other one. As the field continues to increase, the filaments percolate at 3.9T and then fade into the background when the difference in magnetization is too low to keep the carriers inside the filaments.*

5. Grazing incidence small angle scattering

5.1. Principle

Since nanosciences are aiming at very small scales (well below $1\mu m$), off-specular scattering will reach its limits since it can probe only rather large correlation lengths ($\xi > 500\,nm$). This is why surface scattering has been extended to the SANS geometry. In this geometry, one looks at the scattering in the plane perpendicular to the incidence plane (Fig. 1.5, green plane). The scattering wave vector Q_y is in a range comparable to the scattering wave vectors in SANS experiments: $10^{-4} < Q_y < 3nm^{-1}$. This corresponds to correlation lengths ξ ranging from 3 nm to 100 nm.

GISANS may typically be used to study small particle sitting on a surface ($\xi \sim 20 - 100nm$) (Fig. 5.1a), arrays of nanowires ($\xi \sim 20 - 100nm$) (Fig. 5.1b), magnetic domains self-organized in a regular structure ($\xi \sim 100nm$) (Fig. 5.1c), magnetic – structural surface correlations ($\xi \sim 10 - 20nm$) (Fig. 5.1d).
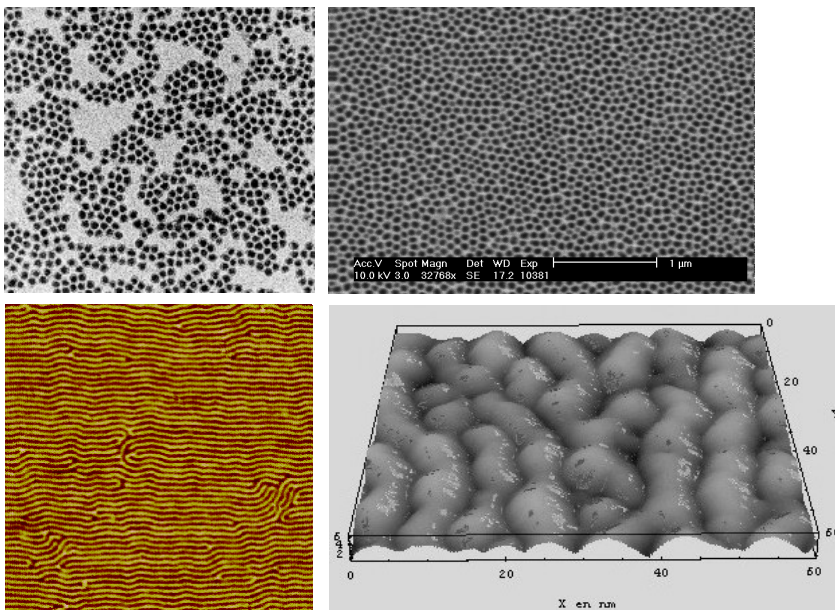
Figure 5.1.: *(a) Small particle sitting on a surface; (b) arrays of nanowires; (c) magnetic domains self-organized in a regular structure; (d) magnetic – structural surface correlations.*

The technique of grazing incidence neutron scattering is based on the propagation of an evanescent wave along the surface when the incident angle is smaller than the critical

5. Grazing incidence small angle scattering

angle of total reflection (see Annexe II) . Figure 5.2a illustrates the reflection of a neutron wave incident on a surface for an incidence angle equal to the critical angle of reflection. It can be seen that the neutron wave-function density is increased at the vicinity of the surface. It corresponds to the evanescent wave which travels along the surface. It is possible to calculate the penetration depth of the neutron in the substrate as a function of the incidence angle (Figure 5.2b). For very small angles, the neutron remains localized over the top 100Å of the surface; as soon as the incidence angle gets close to the critical edge, the neutron wave penetrates deeply in the substrate. When the neutron wave-function is localized at the surface in the form of an evanescent wave, its interaction with the surface and thus the scattering cross section are increased.
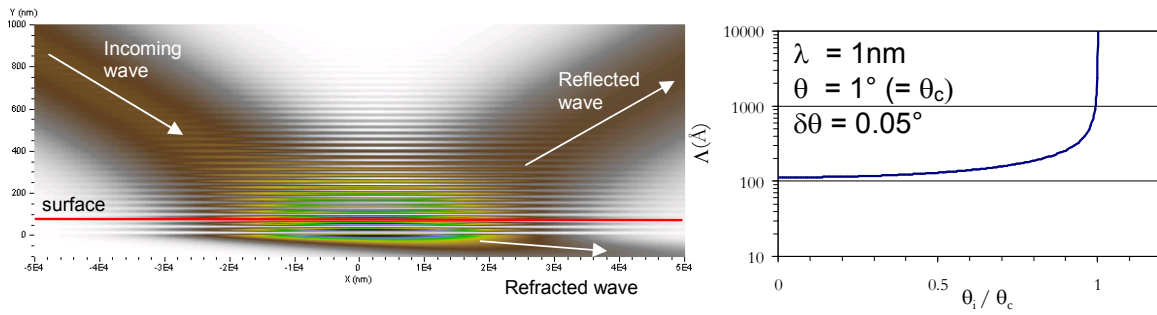
Figure 5.2.: *(a) Reflection of a neutron wave on a surface for an incidence angle equal to the critical angle. The plot represent the neutron wavefunction density $|\Psi|^2$. (b) Penetration depth Λ of the neutron in the film as a function of the incidence angle.*

It can be shown that in the case of buried particles (see Figure 5.3a), the scattered intensity can be expressed as [120]:

$$I\left(Q\right) \propto \left| T\left(k_z^i\right) T\left(k_z^f\right) F\left(Q\right) e^{iQd} \right|^2$$

where the T factors are the transmission coefficients amplitudes. The amplitude of these coefficient increases very strongly around the critical angle (see Fig. 5.3b) so that the scattered intensity is significantly enhanced by about a factor 10.
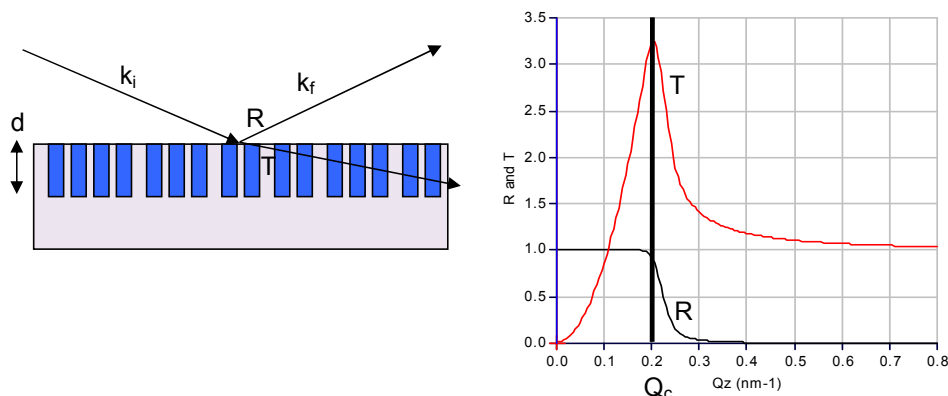
Figure 5.3.: *(a) Reflection on buried particles. (b) Enhancement of the transmission coefficients amplitude at the interface close to the critical edge (calculated for an angular and wavelength resolution of 10%).*

GISANS experiments are typically performed on SANS spectrometers because a good collimation is required both in the incidence plane (to define the incidence angle) and perpendicular to the incidence plane (to achieve the required resolution for the SANS measurement). The spectrometer PAPYRUS at the LLB has been upgraded so as to make GISANS experiments relatively easy to perform (Fig. 5.4). It provides a versatile sample environment (Cryomagnet 4K – 6T; Displex 4K ; Electromagnet 1T).
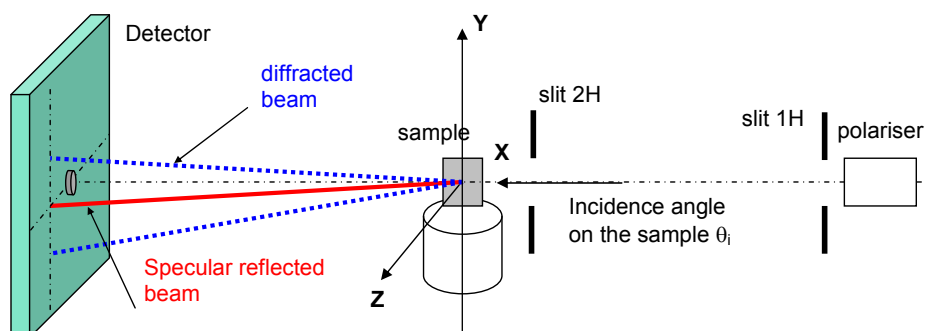
Figure 5.4.: *Scheme of the PAPYRUS spectrometer at the LLB.*

5.2. Example : Fe nanodots

By using alumina membrane masks, it is possible to produce arrays of nanodots (see Fig 5.5). C.P. Li et al have fabricated such arrays using Fe [24]. The typical size of the Fe dots ranges in the $30 - 50\,nm$ scale. Even though the amount of material is very small, we have been able to show that GISANS experiments were possible on such arrays (see Fig. 5.6). A clear magnetic constrast can be observed at the position of the correlation peak. Unfortunately, the low statistics prevent extracting more detailed information such as the magnetic form factor of these objects and probe the magnetic vortex state which is expected to exist in these very small dots.

This demonstrates that it is possible to probe very small amount of matter ($\sim 10\mu g$). More detailed information can be found in [24].

5. Grazing incidence small angle scattering

A more detailed example of GISANS study will be presented in Chapter 10.
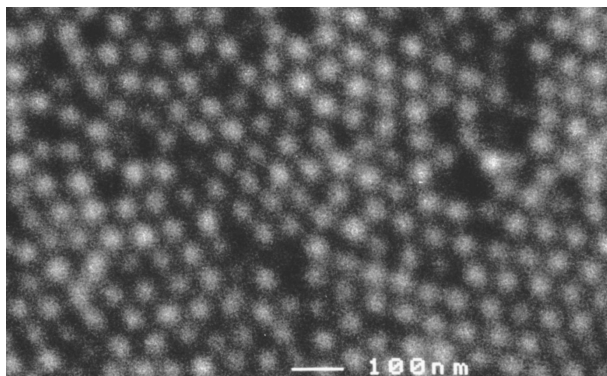
Figure 5.5.: *SEM image of an Fe dot array fabricated using an alumina mask anodized at 25 V with average diameter and periodicity of 32 and 63 nm respectively.*
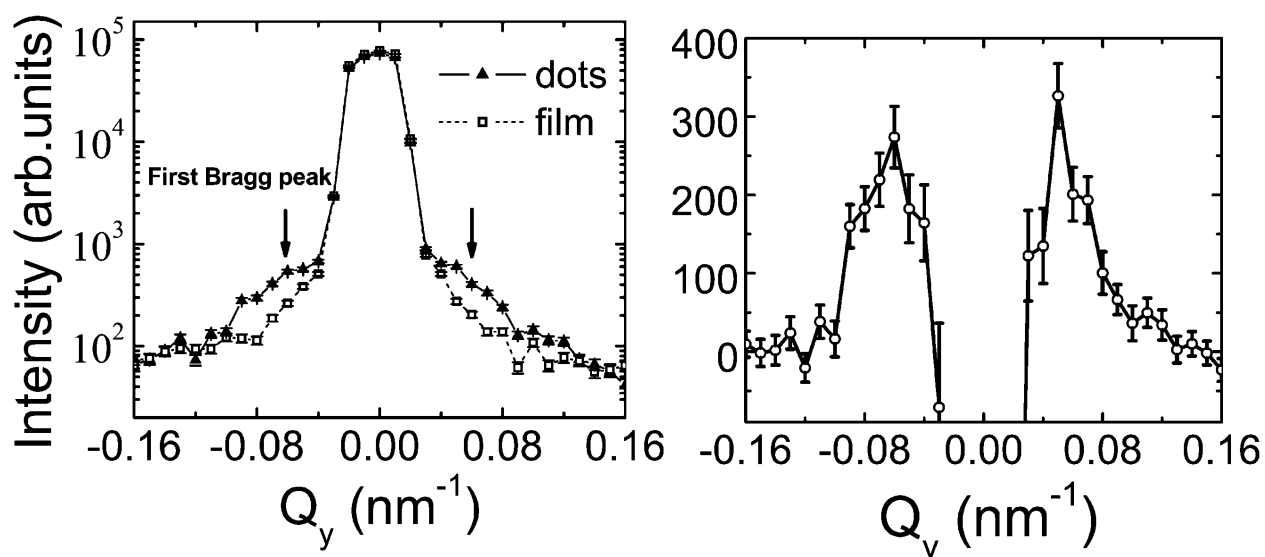
Figure 5.6.: *Scattering intensity as the function of momentum transfer vector Q_y for an array of Fe dots 20 nm height, 65 nm average diameter and a continuous Fe film of the same thickness . The statistical errors are given by the square root of the scattering intensity. Due to their small sizes, most of the error bars are covered by symbols. (bottom) Difference between the scattering intensity of dots and that of the film.*

6. Diffraction

In the previous chapters, we discussed experiments performed at grazing incidence. In this geometry, the interaction between the sample and the neutron beam is maximized but it limits the characterization to *nanoscale* ferromagnetic properties. One of the unique features of neutron diffraction is that the magnetic order can be probed at the atomic scale [122]. As it has been mentioned above, the neutron magnetic scattering length is of the same order as the nuclear scattering length. Diffraction experiments can be performed with short wavelength neutrons (from 0.5Å to 2.5Å). It is thus possible to measure the magnetic structure factor of a crystal, that is the location of the magnetic atoms. Neutrons provide information about the absolute value of the magnetization but also about their directions (Fe moments in $YBa_2Fe_3O_8$ for example [123]). It is thus possible to unravel complex magnetic orders (anti-ferromagnetic, helical or with several magnetic sublattices). It is also possible to measure the magnetic form factors which gives the spatial distribution of the magnetic electrons. This permits to reconstruct spin density maps in magnetic crystals [124]. Following the dependence of the magnetic scattering as a function of the temperature can give detailed information about magnetic phase transitions: spin reorientation phenomena [125] or the order parameter of magnetic sublattices (Er in $ErBa_2Cu_3O_7$ for example [126]).

The volume of magnetic matter is very small in thin films, but nevertheless, the performances of modern neutron spectrometers are such that high angle diffraction experiments can be performed on epitaxial thin films. Since the absorption is negligible, any direction in the reciprocal space can be probed and the sample substrate is not an issue, which is interesting compared to the use of x-rays. In practice, it is possible to probe epitaxial thin films with thicknesses down to 10 nm. Neutron diffraction is especially unique when probing anti-ferromagnetic crystals. Another advantage in the case of anti-ferromagnetic crystals is that it often gives rise to purely magnetic diffraction peaks which are not superimposed with structural peaks [127]. In the case of oxide films, we have probed the AF order in single layer NiO films as thin as 20 nm thick [128]. Neutron diffraction can be used in various situations for thin films. It has been used to follow the Néel transition temperature of thin films and correlate it with the apparition of exchange bias in systems such as Fe_3O_4/CoO. It has been demonstrated [129] that the blocking temperature at which the exchange coupling appears is not trivially correlated with the Néel temperature of the AF material. For very thin films (below 5nm), while the blocking temperature drops, the Néel temperature increases significantly.

In [NiO/CoO] superlattices, the propagation of the anti-ferromagnetic order throughout the superlattice as a function of the thickness of the bilayer period (ranging from 4 to 9nm) [130] was probed by neutron diffraction. Neutron diffraction can also be used to check the influence of epitaxial strain on the AF order in epitaxial films. For example, in CoO films, an epitaxial strain of 0.5% increases the Néel temperature by about 15K. This is a rather general trend. More recently, neutron diffraction showed that the epitaxial strain

destroys the helical order in $BiFeO_3$ films [131]. This is an important piece of information since the knowledge of the magnetic order is a prerequisite for the understanding and use of magneto-electric materials [132]. Beyond the information about the magnetic order, more refined information may be obtained about the sizes of AF domains by analyzing the diffraction peak widths. This information is of particular interest in exchange bias systems in which the anti-ferromagnetic microstructure is likely to play a key role in the exchange bias mechanism. This has been demonstrated in Fe_3O_4/NiO superlattices [133]. The field dependence of domains in the antiferromagnetic NiO is correlated with the presence or absence of exchange biasing. The data suggest that in this system, exchange biasing originates from domain walls frozen in the antiferromagnet upon field cooling.

A number of diffraction studies have also been performed on epitaxial RE thin films [139, 140, 141] in which the large magnetization of rare earths helps performing precise measurements.

I am presenting here the example of a recent study on $MnAs$ films in which I was involved (Fig. 6.1). The first order magnetic transition in a MnAs film ($100\,nm$ thick) between the magnetic phase α of MnAs to the paramagnetic β phase was followed by neutron diffraction (on the spectrometer 4F1 at the LLB). One can observe that both phases coexist over a wide temperature range ($\sim 70K$) and that the behavior of epitaxial films is very different compared to bulk systems. This allowed V. Garcia et al to understand the role of the epitaxial strains to stabilize the ferromagnetism to higher temperature [136].

A few years ago we have evaluated the possibility to perform *Polarized Grazing Incidence Diffraction*, in order to increase the diffraction efficiency on thin films samples [134, 135]. Technical details are presented in Annexe II. We demonstrated that it was possible to measure the diffraction on oxide films as thin as $20nm$. However, in practice, such experiments are very difficult to set-up since they require a complex sample alignment. It also proved that the lower flux in the guide hall was barely compensated by the grazing incidence geometry. But the biggest drawback of the Grazing Incidence Geometry is that the scattering plane is limited to the sample surface. Thus, the possibility of having neutrons passing through the substrate and scanning in arbitrary directions in Q-space is lost. This possibility is a key advantage since it makes neutron diffraction experiments competitive with x-ray experiments. We thus did not pursue the development of Grazing Incidence Diffraction technique.

More recently, significant improvements have been made in the field of diffraction via the use of Position Sensitive Detectors on 4-circles diffractometers. This set-up provides a very simple alignment of the samples even if the scattered signal is very weak and makes the experiment much more efficient than was previously possible. At the atomic scale, diffraction experiments are possible on very small quantities of matter (down to $0.001\,mm^3$) [138]. Magnetic structures specific to thin films heterostructures ($\sim 20 - 100\,nm$ thick) can be characterized. Rapid progress are being made in this field through the use of high resolution position sensitive detectors on single crystal diffractometers which allow to reduce the acquisition times by an order of magnitude: several diffraction peaks are measured at once, the shapes of the diffraction peaks are measured at once and complex magnetic structures can be very quickly disentangled [138].
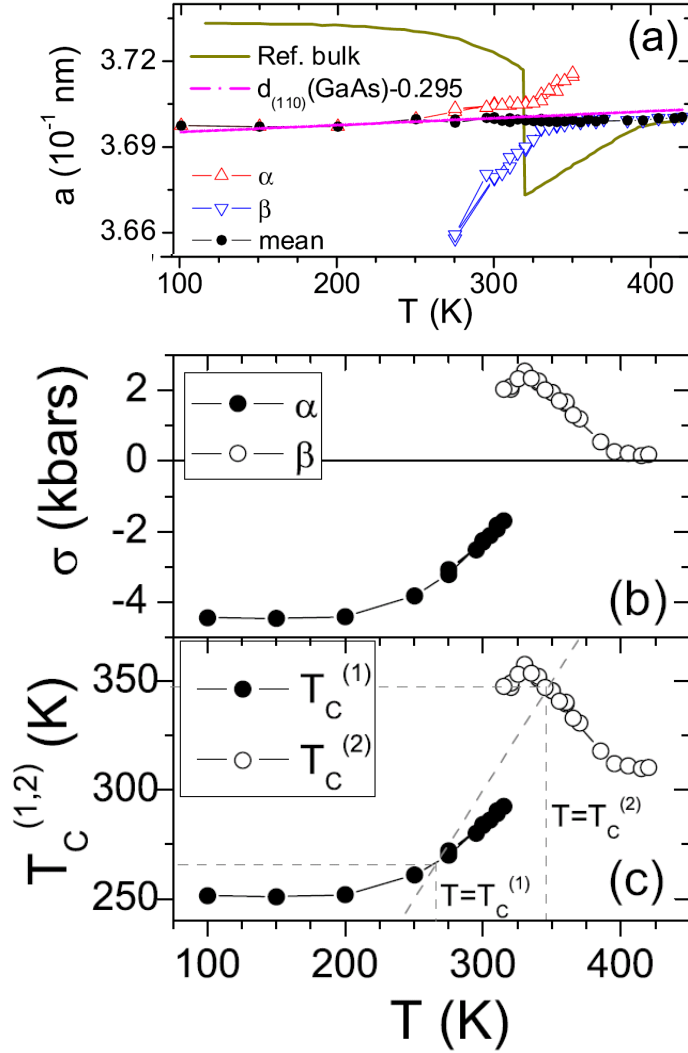
Figure 6.1.: *(a) Evolution of the lattice parameters 'a' of an epitaxial MnAs(100) thin film [136] as a function of the temperature deduced from neutron diffraction. (red) α-phase, (blue) β-phase, (green) in a bulk sample. In the thin film, the α and β phases coexist over 70 K around the transition temperature. (b) Calculated in-plane stress deduced from the lattice deformation compared to bulk values. (c) Calculated critical temperatures considering the in-plane stress equivalent to pressure using the temperature-pressure phase diagram of bulk MnAs from [137]. The critical points are deduced from the intersection between the experimental points and the straight line $T = T_C$. The 2 critical points T_C^1 and T_C^1 define the coexistence region between the α and β phases.*

6. Diffraction

7. Inelastic scattering

The neutron kinetic energy is related to its wavelength by the relation $E = h^2/2m\lambda^2$. After moderation, neutrons are very low kinetic energy particles. A neutron of wavelength 1Å neutrons has a kinetic energy of $80\,meV$. This makes neutrons very suitable for the study of the excitations such as phonons or magnons. Neutron scattering is routinely used for the measurement of magnons or phonons dispersion curves in crystals [142].

It is tempting to extend the use of inelastic scattering to magnetic nanostructures. The early successful attempts were performed on large volume samples composed of magnetic nanoparticles. I shall illustrate the technique by a couple of examples. In these cases, the sample volume was not a challenge.

Extending inelastic studies to thin films is far more challenging for the simple reason that the volume of matter is minute, well below a cubic millimeter. Very few successful attempts have been performed.

I have not been personally involved in any of these studies in which people were specifically interested in high energy magnons excitations. However, I have performed an attempt to study very low magnetic excitations (in the GHz range) called magneto-static excitations which are specific to the confined geometry of thin films.

7.1. Small particles

Surprisingly, rather few inelastic neutron scattering studies have been performed on small magnetic particles [143, 144, 145, 146, 147]. These studies were limited to spherical magnetic nanoparticles of Fe, $\alpha - Fe_2O_3$ and NiO. Figure 7.1 illustrates some of these measurements. Spin-echo spectroscopy provided a measurement of the relation time in correlated assemblies of Fe nanoparticles [146]. Inelastic time-of-flight measurements were used to probe the Néel-Brown model for superparamagnetic relaxation and for the collective magnetic excitations in $\alpha - Fe_2O_3$ particles [147].
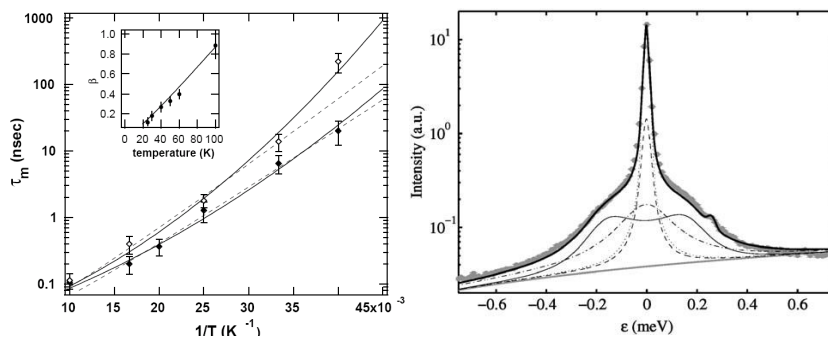
Figure 7.1.: *(a) Relaxation of Fe particles assemblies measured by Spin-Echo spectroscopy [146]; (b) damped harmonic oscillator function in the inelastic TOF signal.*

One of the reason why so few studies have been performed is linked to the request to produce high quality sample (very monodisperse nano-objects) in great quantity (grams). Combining these two requirements has not been very easy until recently. However, things are moving quickly in the synthesis of nano-objects and it is likely that the study of magnetic excitations in nanostructures by inelastic neutron scattering will develop in the near future.

7.2. Thin films

Presently, information on magnetic excitations in thin films is obtained by inelastic light scattering (BLS [148]) or by ferromagnetic resonance (FMR) [149]. FMR and BLS are limited by the fact that they can probe spin wave-excitations only at the center of the Brillouin zone. It is not possible to determine the dispersion of spin waves over the entire Brillouin Zone. With inelastic neutron scattering, it is in principle possible to probe the entire Brillouin zone.

The case of inelastic neutron scattering in magnetic thin films was considered very early [153]. Attempts to perform inelastic measurements on magnetic thin films have been restricted to very specific samples. These inelastic measurements were limited to the study of rather thick films ($1\mu m$) and materials with large magnetic moments (Dy [150] and Mn [151], Fig. 7.2). The volume of matter was of the order of $1\ mm^3$.
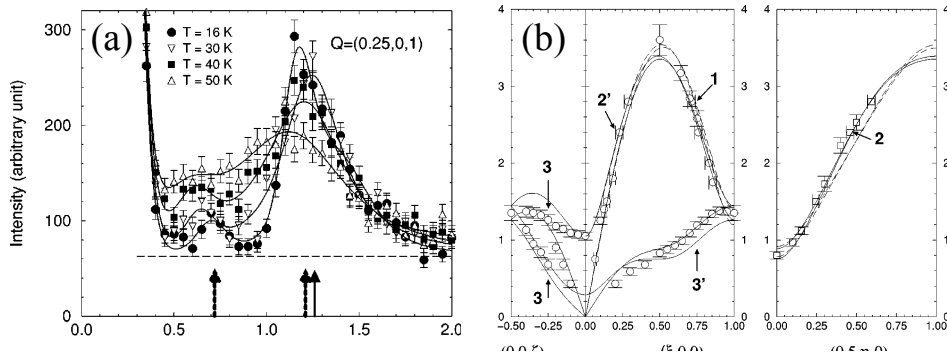
Figure 7.2.: *(a) Temperature dependence of the spin-wave modes in a MnTe epitaxial film. (b) Spin wave dispersion at T=15K (adapted from B. Hennion et al [151]).*

Besides these attempts to characterize magnon excitations in thin films (in the meV/THz range), we tried to study the dynamics of magneto-static excitations in thin films (in the GHz range) [152]. Such excitations can be quantified using Brillouin light scattering or ferromagnetic resonance but the dispersion of these waves is measurable only at very low scattering wave-vectors when using these techniques. Our aim was to extend the characterization of these excitations to non zero scattering wave vectors. These experiments have unfortunately not been successful. A more detailed description of these experiments is given in Annexe III.

Presently, the study of magnetic excitations in thin films is limited to feasibility studies and is not a mainstream technique. Unless there is a methodology or technological breakthrough, I do not expect this to change in the foreseeable future.

8. Conclusion – Future

8.1. Neutron – X-ray comparison

In the last decade, great efforts have been made to apply X-ray scattering to the study of the magnetism of thin films. The high flux available on the synchrotron sources compensates for the weak magnetic interaction of X-rays. In this paragraph we want to underline the strengths and weaknesses of the different scattering techniques.

Neutron reflectivity has the following characteristics:

+ It is a direct quantitative probe of the magnetization. The data processing is very simple and quantitative. It is straightforward to obtain the magnetization profile (amplitude and direction) in a thin film system.

+ Complex sample environments are available (very low temperatures, high temperatures, high magnetic fields)

+ It is possible to probe buried layers. Protective capping can be used. The corollary is that it is possible to probe complex systems consisting of several layers. It is not necessary to design the system specifically for the scattering experiment.

+ The high transmission of neutron beams allows to probe bulk properties of the materials. This is especially interesting in the case of SANS measurements.

− The flux is low and several hours of measurements are required for each sample and experimental conditions. Dynamics can be probed only down to $\sim 10\,\mu s$ in stroboscopic mode.

− Neutrons have a weak chemical sensitivity and resonant techniques or spectroscopic techniques do not exist.

− It is not possible to distinguish the spin and orbital moments.

The techniques of magnetic X-ray scattering (X-ray dichroism; resonant X-ray reflectivity; X-ray imaging) have the following advantages / disadvantages:

+ High flux

+ Chemical sensitivity

+ High speed dynamics

+ Imaging possibilities (sub-µm)

− The data processing is very complex because the magnetic interaction is tensorial. Quantitative data are difficult to extract on complex materials.

− It is difficult to setup complex sample environments.

− It is difficult to probe buried layers.

− It is not possible to perform vector magnetometry.

8.2. Future evolutions

A very large range of correlation lengths in thin film systems can now be probed using neutron surface scattering techniques.
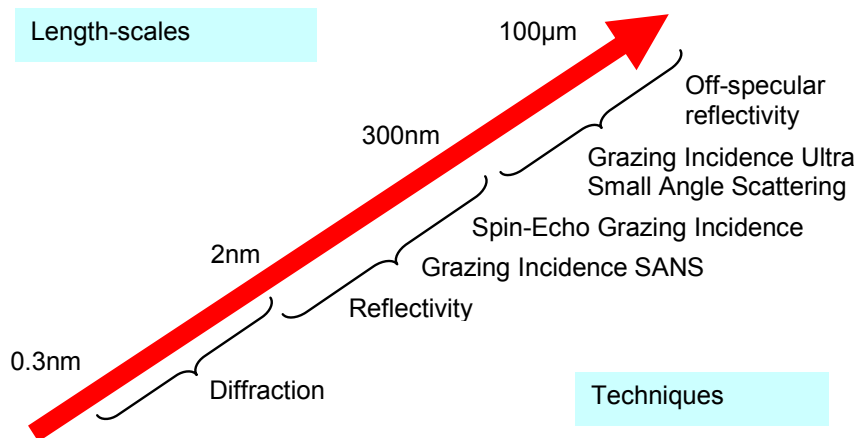
Figure 8.1.: *Correlation lengths and suitable scattering techniques.*

A wide set of techniques are nowadays available (Fig. 8.1): *specular neutron reflectivity* which is operated routinely, *off-specular scattering* which is easily performed but which requires complex data processing, *Grazing Incidence SANS* which is still in development, and *diffraction* on thin films which in the case of good quality systems is feasible. For the foreseeable future, *inelastic experiments* on thin films will be restricted to very specific systems. A very large range of correlation lengths in thin film systems can now be probed using these different scattering techniques.

Presently, a big effort is made in order to increase the flux on neutron reflectometers. Flux gains ranging from 10 to 100 can reasonably be expected in the next decade through the implementation of new types of neutron reflectometers (see Part III). Quantitative gains in the measuring time and in the minimum sample size will be achieved. However it is not yet clear if qualitative gains, i.e; new types of measurements besides the ones presented here, will be achieved.

A large number of neutron reflectometers are available across the world [155]. The Web site [156] gives you links to neutron reflectivity simulation and fitting programs.

Part II.

Magnetic non collinear structures - Magnetic chiral structures

9. Non collinear magnetic structures

We shall now discuss the scattering of neutrons on non collinear and more generally on chiral structures. This topic has been extensively studied in the field of diffraction where helical orders in crystals have been studied by neutron diffraction.

In this part we will focus more specifically on nanoscale non collinear structures, that is, with typical lengths well above of few lattice parameters as usually measured by neutron diffraction. In a first section, we recall the different configurations in which non collinear magnetic structures can appear in thin films or at interfaces. The next chapter then illustrates the various thin film systems in which I have encountered such magnetic nanostructures. The last chapter is dedicated to chiral structures observed in magnetic crystals by SANS.

In this chapter I will browse through the different situations in which non collinear magnetic structures may appear. Non collinear magnetic structures appear when a symmetry of the system is broken. This usually happens when magnetic domains are created in a material in which case the translation symmetry is broken. In this case, *surfaces called domain walls* appear between the magnetic domains. Understanding and modeling the spin structure at these surfaces is important since it plays a role in the magneto-transport properties of a materials. This is of prime interest for spintronics applications.

Domain walls or non collinear structures can also appear at grain boundaries, anti-phase boundaries, interfaces between two materials or in exchange coupled structures.

Non collinear structures also appear in bulk materials in the form of helix. This can be studied by neutron diffraction (typically in rare-earth materials) [157]. In the case of long range magnetic modulations, small angle scattering or reflectometry can be used.

9.1. Magnetic energies

In the formation of magnetic structures, a few magnetic energies play a key role:

- The *exchange energy* tends to keep adjacent magnetic moment parallel to each other. It corresponds to the cost of a change in the direction θ of the magnetization between two magnetic moments:

$$E_{ex} = A \left(\frac{\partial \theta}{\partial x} \right)^2$$

  where A is the exchange stiffness expressed in J/m.

- The *magnetostatic energy* tends to minimize the dipolar energy. It arises when there is a discontinuity in the normal component of the magnetization across an interface:

$$E_{ms} = -\mu_0 M_S \cdot H_i = \frac{\mu_0}{2} M_s^2 cos^2\theta$$

where $H_i = H_{ext} - NM$ is the internal field.

- The *magneto-crystalline anisotropy* describes the preference for the magnetization to be oriented along certain crystallographic directions:

$$E_a = K_1 \left(\alpha_1^2 \alpha_2^2 + \alpha_2^2 \alpha_3^2 + \alpha_3^2 \alpha_1^2 ... \right) \qquad for\ cubic\ crystals$$
$$E_a = K_2\ sin^2\theta \qquad for\ uniaxial\ crystals$$

where θ is the angle with respect to the easy axis and α_i are the direction cosines with respect to the crystallographic axis.

- The *magneto-elastic energy* is the part of the magneto-crystalline anisotropy which is proportional to strain:

$$E_{me} = B_1 \sum e_{ii} \left(\alpha_i^2 - 1/3 \right) + B_2 \sum e_{ij} \alpha_i \alpha_j \qquad for\ cubic\ crystals$$
$$E_{me} = B_1 e_{33} sin^2\theta = \tfrac{3}{2}\lambda_s \sigma cos^2\theta \qquad for\ isotropic\ materials$$

where λ_s is the magnetostrictive constant.

- The *Zeeman energy* is the potential energy of a magnetic moment in a field:

$$E_Z = -\mu_0 M \cdot H_{ext}$$

- A surface anisotropy energy which can be either positive or negative. A positive surface energy favors a perpendicular magnetization at the interface:

$$E_s = K_S\ sin^2\theta$$

9.2. Domain walls

In real samples, the equilibrium state is rarely a state with an homogeneous magnetization. In bulk crystals, magnetic domains and domain walls are formed to reduce the magneto-static energy. In thin films heterostructures, various types of coupling can lead to non collinear magnetic states.

We consider the general situation of 2 media separated by an interface at $z = 0$. Medium {1} spans from $-d_1$ to 0 and medium {2} spans from 0 to d_2. The normal to the interface is taken as the (Oz) axis. The direction of the magnetization with respect to the (Ox) axis is given by θ. We will quickly describe the way to derive the magnetization equilibrium state and apply it to various situations encountered in thin film systems.

The total magnetic energy can be expressed as:

$$E_{tot} = E_{ex} + E_a + E_Z + E_{int} + E_{surf}$$
$$= \int_{-d_1}^{d_2} \left[A\left(z\right) \left(\tfrac{d\theta}{dz} \right)^2 + K_u\left(z\right) sin^2\theta - \mu_0 M \cdot H\ cos\theta + \delta(z)\ A_{int} \left(\tfrac{d\theta}{dz} \right)^2 + \delta(z)\ K_S\ sin^2\theta \right] dz$$

where we have included the exchange energy, an uniaxial magnetic anisotropy K_u lying along (Ox), the Zeeman energy with an external field H applied along the (Ox) direction and two interfacial contributions, an exchange interface energy and a surface anisotropy
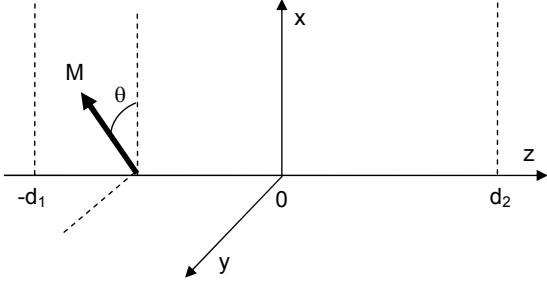
Figure 9.1.: *General situation of two media separated by an interface at $z = 0$.*

energy. Note that the demagnetizing field contribution is neglected in the above expression.

We want to determine the stable wall profile $\theta(z)$. It is thus necessary to minimize the total magnetic energy. The variational principle should be applied to the above equation: $\delta E_{tot} = 0$. This derivation provides Euler equations [159]:

$$2A(z)\frac{d^2\theta}{dz^2} = 2K_u sin\theta cos\theta + \mu_0 M \cdot H \, cos\theta$$

This differential can be solved in medium {1} and {2} and provides the general form:

$$\theta(z) = ArcTan\left[sinh\left(a_0 + b_0 z\right)\right] + \frac{\pi}{2} = 2ArcTan\left[exp\left(a_0 + b_0 z\right)\right]$$

We shall now browse through different situations which are encountered in real systems.

9.2.1. Bloch wall: 180° domain wall

The most standard situation is encountered in bulk materials where magnetic domains appear. In this case, medium {1} and {2} are equivalent and can be described by an exchange constant A and an anisotropy K_u. Since domains are much larger than the domain walls, the limits d_1 and d_2 can be set to infinity. The boundary conditions can then be taken as $\left(\frac{d\theta}{dz}\right)_{\pm\infty} = 0$.

The Euler equation can thus be solved and provide the following variation:

$$\theta(z) = ArcTan\left[sinh\left(\frac{\pi z}{\delta}\right)\right] + \frac{\pi}{2} = 2ArcTan\left[exp\left(\frac{\pi z}{\delta}\right)\right]$$

with $\delta_{DW} = \pi\sqrt{\frac{A}{K_u}}$ being the domain wall width.

This situation can be encountered in reflectivity when a Bloch wall is created parallel to a thin film surface. Such a configuration can be created by applying a strong electrical current in a magnetic thick film. Such systems are presently under study together with Michel Viret (IRAMIS/SPEC).

9.2.2. Néel wall

In bulk materials, Bloch walls are the most favorable magnetic walls since they minimize the magneto-static energy. However, in thin films, Bloch walls give rise to magneto-static
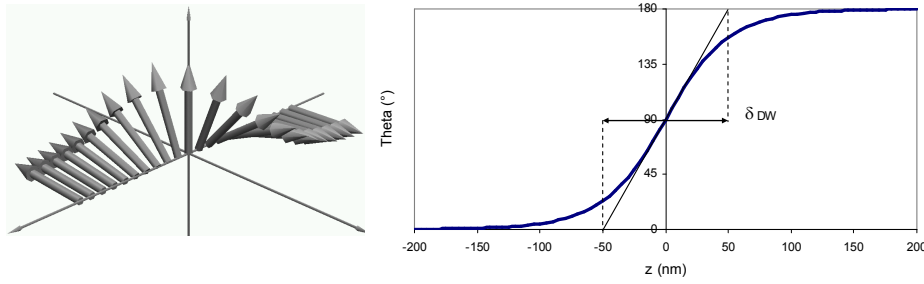
Figure 9.2.: *(a) Bloch wall. (b) Variation of the magnetization angle Vs position.*

energy at the top and the bottom of the wall (Fig. 9.3a). For sufficiently thin films, it is favorable to create a Néel wall (Fig. 9.3b) in which the spins rotate in a plane perpendicular to the domain wall (Fig. 9.4). The magnetization thus remains in the thin film plane and minimizes the magneto-static energy.

The width of a Néel wall is given by $\delta_{DW} = \pi\sqrt{\frac{2A}{K_u}}$.
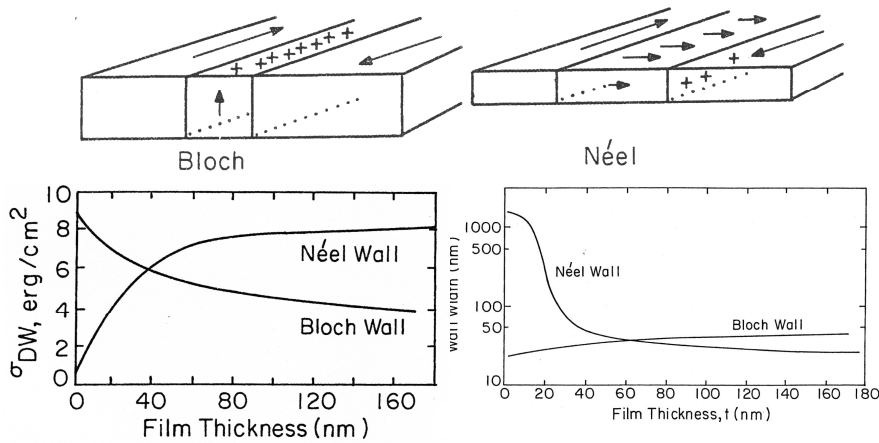
Figure 9.3.: *(a) Comparison of a Bloch and a Néel wall. (b) Energy per unit area of a Bloch wall and a Néel wall (for $A = 10^{-11} J/m$, $B = 1\,T$ and $K = 100\,J/m^3$).*
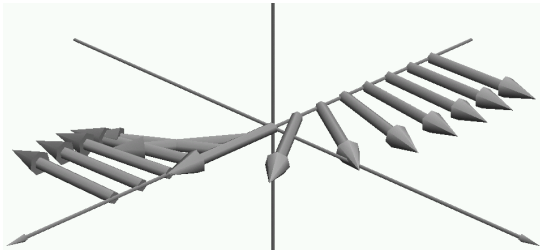
Figure 9.4.: *(a) Néel wall.*

9.2.3. Anti-phase boundaries

We shall now consider the case in which there is a physical interface between the two different magnetic domains. We first consider the case of an Anti-Phase Boundary which commonly appears in spinelle structures such as Fe_3O_4 or $CoFe_2O_3$.

At an anti-phase boundary, in spinelle materials, the magnetic sub-lattices are anti-ferromagnetically coupled. This gives rise to the pinning of domains walls at these interfaces. On Fig. 9.5, I have represented the case of 2 regions strongly anti-ferromagnetically coupled. At the interface there is a sharp jump of the magnetization by an angle π. This affects the magnetization in the material over a distance $\delta_{APB} = \pi \sqrt{\frac{A_F}{M_s H}}$.

This type of configuration will be discussed in the next chapter in the case of a system in which an artificial APB is created.
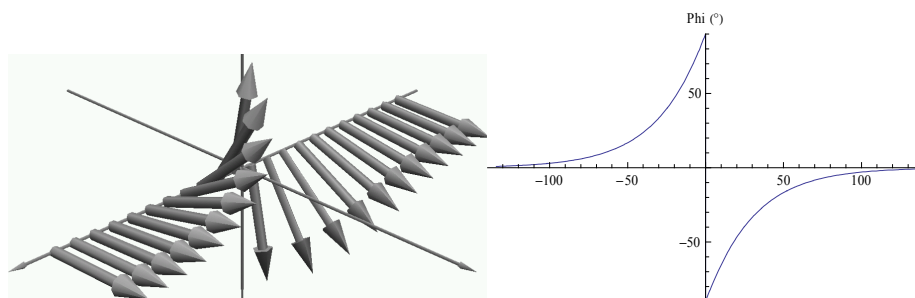
Figure 9.5.: *(a) APB wall. (b) Variation of the magnetization angle Vs position.*

9.2.4. Grain boundaries

Non collinear magnetization can appear in nanocrystalline materials containing grain boundaries. At these grain boundaries, it is possible that the exchange is reduced. Such a situation will be described in Chapter 12 in the case of a magnetic crystal.
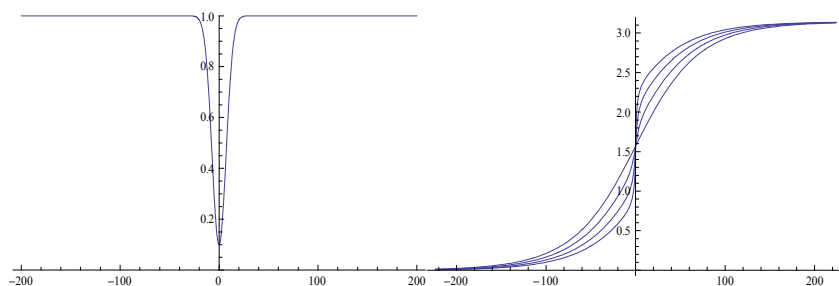
Figure 9.6.: *(a) Exchange constant A variation across an interface; (b) Rotation of the magnetization across the nterface.*

9.2.5. Anisotropy changes

It is also possible that the anisotropy is modified at the interface. This may have several origins: (i) a surface anisotropy K_s appears at the free interface, (ii) 2 magnetic materials

with different anisotropies are in contact with each other.

The detailed magnetic configurations are specific to every details of the system.

9.2.6. Bloch - Néel mixture

In some systems where the dimensions are reduced, Bloch and Néel configurations coexist. Analytical solutions are not tractable and analytical solutions are required. Several micromagnetic packages (OOMMF, NMAG, MAGPAR) are now freely available. They provide a very fast way to simulate complex micromagnetic configurations. The mixture of Bloch and Néel walls can be encountered in thin films systems such as thin FePt or FePd films with perpendicular anisotropy. This will be illustrated in the next chapter.

10. Non-collinear and chiral structures in magnetic thin films

10.1. Chiral effects in polarized neutron reflectometry

The full treatment of polarized neutron reflectometry was only published rather recently [34, 65, 33, 208]. However all the implications of the full calculation have not been fully explored. We discuss here some specific issues related to the spin-flip signals. It is usually assumed that the spin-flip reflectivity signals are symmetrical $R^{+-} = R^{-+}$. The first experimental report of non symmetrical spin-flip signal was made by Felcher and al [66, 67]. The prediction of the effects was mentioned in [34, 65]. In this section we describe the different effects which are likely to break the symmetry between the R^{+-} and R^{-+} signals in a reflectivity experiment. The first effect is related to Zeeman energy changes which can take place when the neutron flips during the reflection on a surface. If a sufficiently high magnetic field is applied on the sample and if the neutrons experience a spin-flip during the reflection, they will either gain or loose magnetic Zeeman energy. Since the reflection process is an elastic one, the energy is fully transferred as a gain or loss in kinetic energy. Both requirements (high magnetic field and spin-flip signal) are opposite since in usual situations, the magnetization will align with the applied field and the spin-flip scattering cross section will be zero. In practice, these effects are observed when the magnetic field is applied perpendicular to the sample and the demagnetizing field prevents the magnetization to rotate out of the thin film plane. These are the conditions under which the effect was quantified for the first time [66].
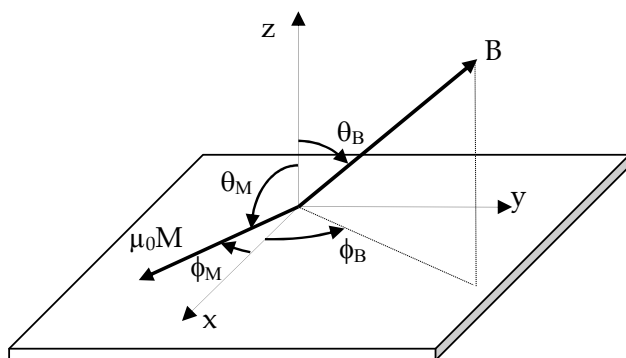
Figure 10.1.: *Notations for the polarization guide field B and the magnetization M in the layer.*

The Figure 10.1 describes the notations used in the following to describe the magnetic field and the magnetization directions. We use spherical coordinates. (Oz) is the axis

perpendicular to the surface. θ is the zenith angle between B or M and the (Oz) axis. If $\theta = 90°$, B or M are in the surface plane. If $\theta = 0°$, B or M are perpendicular to the surface. ϕ is the azimuth angle in the film plane.

If we consider the situation of an in-plane magnetization, if the guide field B is low (tens of mT), the spin-flip cross section is very large as soon B is non collinear with M (see Fig 10.2b, red curve). However, both spin-flip signals R^{+-} and R^{-+} are equal. The reflectivity does not depend on the fact that B is or not in the film plane. The three configurations of Fig. 10.2a) are equivalent. When the applied field is large (fraction of a tesla), significant asymmetry effects are observed in the spin-flip cross sections (see Fig. 10.2c, red and orange SF curves).
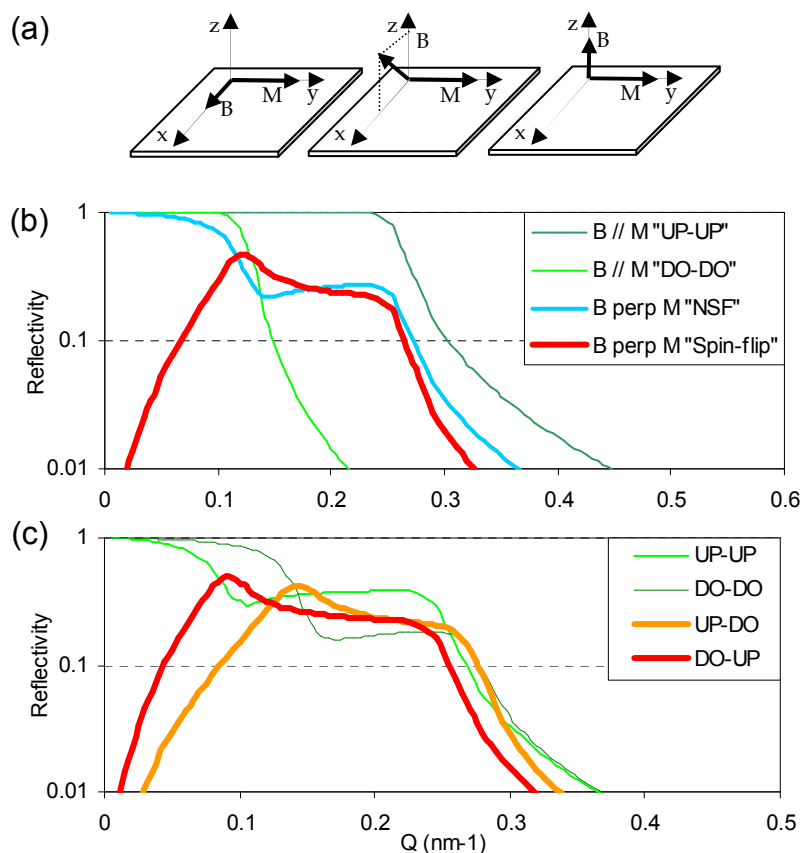
Figure 10.2.: *(a) Relative orientations of B and M giving the same reflectivity curves. (b) Spin-flip reflectivity with M⊥B in low fields. Both configurations lead to the same spin-flip signals (red curve). The reflectivity with B//M is plotted as a reference (green curves). (c) Reflectivity cross sections in high fields (0.5T). Note the very large splitting of the 2 spin-flip signals up-do and do-up (red and orange curves).*

The second geometry which can break the symmetry is the case where magnetic chiral structures exist in the magnetic film depth. We illustrate this situation with a Fe semi-infinite medium. We assume that we have a chiral structure at the surface of the thick Fe film in which the magnetization rotates in-plane from the direction (Ox) to –(Ox) over a

thickness of $40nm$ (see Figure 10.3). If the incident polarization is in the film plane, we observe of course a very large spin-flip signal. However, there is no asymmetry in the spin-flip reflectivity (see Figure 10.3b). When the incident polarization is perpendicular to the film plane, a large difference appears in the two spin-flip cross sections. The non spin-flip cross sections are identical. In an intermediate situation where the magnetization makes an angle of 45° with respect to the surface (see Figure 10.3c), the difference between the two spin-flip cross section becomes even bigger. The non spin-flip cross sections are again very different and close to the first situation. These effects are qualitatively very different from the Zeeman energy effects (both in their symmetries and in the configurations in which they play a role).

These effects are taken into account in the *SimulReflec* program (see Chap. 13) which is used for fitting reflectivity data.
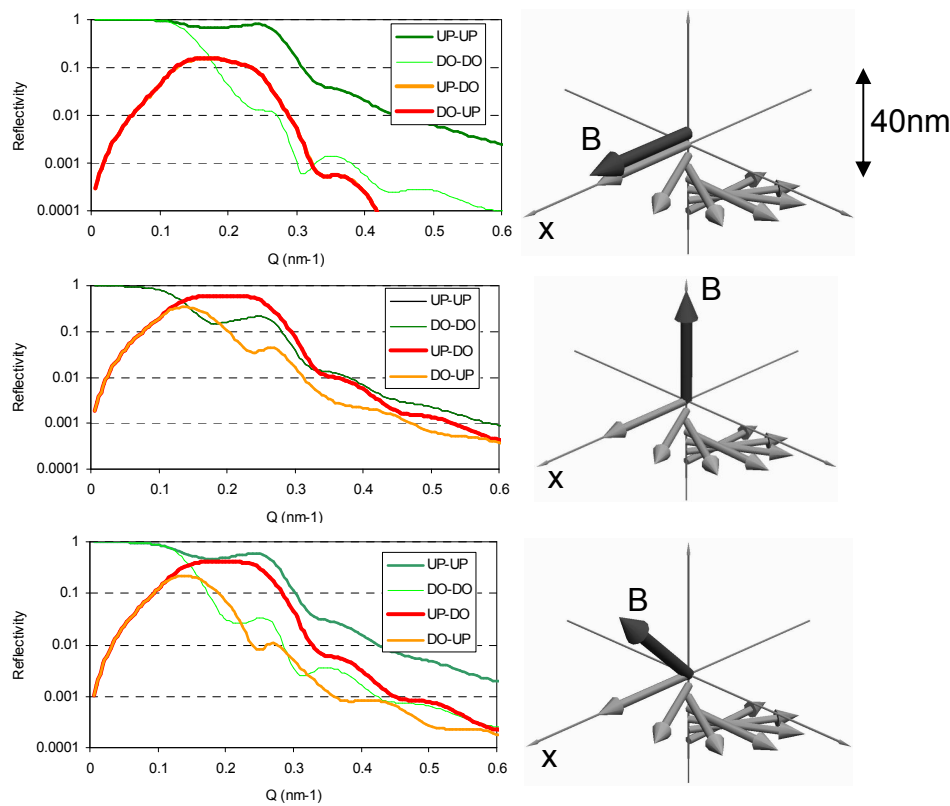
Figure 10.3.: *Effect of a magnetic chiral structure on the reflectivity signals. (a) Polarization in-plane. (b) Polarization perpendicular to the film plane. (c) Polarization at 45°.*

10.2. GMR systems

The optimization of multilayer stacks for magnetic sensors and more sophisticated spin electronics devices requires the precise knowledge of the magnetic properties of each layer together with their behavior as a function of the applied field. As presented in Chapter 2, Polarized Neutron Reflectometry can give vectorial measurements of magnetic moments.

We present here results obtained on GMR spin valves. The neutron reflectivity gives with a high precision, the thickness and magnetic moment configuration and reveals the mechanism of reversal of the soft magnetic layer. This piece of information is important for the optimization of very low noise GMR sensors. The studied GMR spin valve has a rather standard composition (Fig. 10.4):

$SiO_2/Ta(5nm)/NiFe(3.7)/CoFe(1.2)/Cu(2.4)/CoFe(2.4)/MnPt(35)/Ta(10)$.
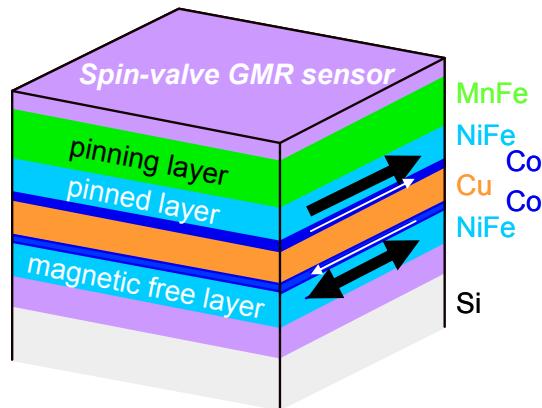
Figure 10.4.: *GMR hetero-structure. The bottom magnetic layer is free to rotate. The top magnetic layer is pinned by the contact with a AF layer.*
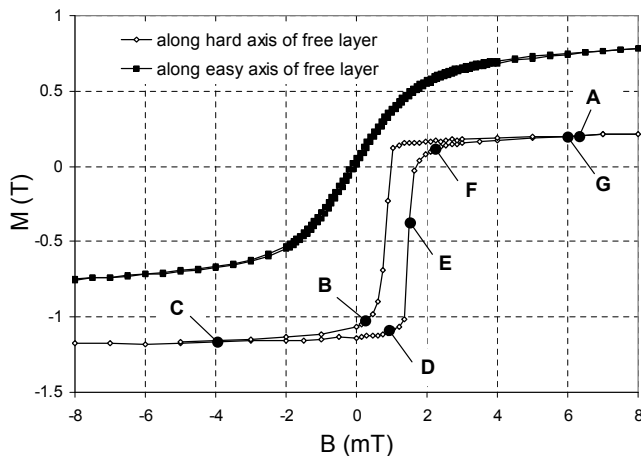
Figure 10.5.: *SQUID measurements of the spin-valve GMR01. The anti-ferromagnetic layer is aligned perpendicular to the easy axis of the free layer.*

The soft layer ($NiFe(3.7)/CoFe(1.2)$) can rotate in a field of several Oe as the hard layer ($CoFe(2.4)/MnPt(35)$) is blocked for fields as large as 1T. The GMR is built with an easy axis of the soft layer (created by an applied external field during the growth) perpendicular to the hard axis. Figure 10.5 shows SQUID measurements on a 9x10mm square sample. This sample has been chosen among others because it exhibits a larger coercivity of the soft layer and makes it possible to select points on the hysteresis curve. The GMR effect with current flowing parallel to the layer is increased when the thicknesses of the different layers are smaller. However, a too small NiFe layer gives rather bad GMR

spin valves. This GMR exhibit a reasonable effect of 9.18% and a very low 1/f noise. The reason for the good behaviour is the absence of domain formation during reversal process independently of the direction of the hard layer. In the presence of domains, 1/f noise can be several orders of magnitude larger which is prejudicial for sensor applications.
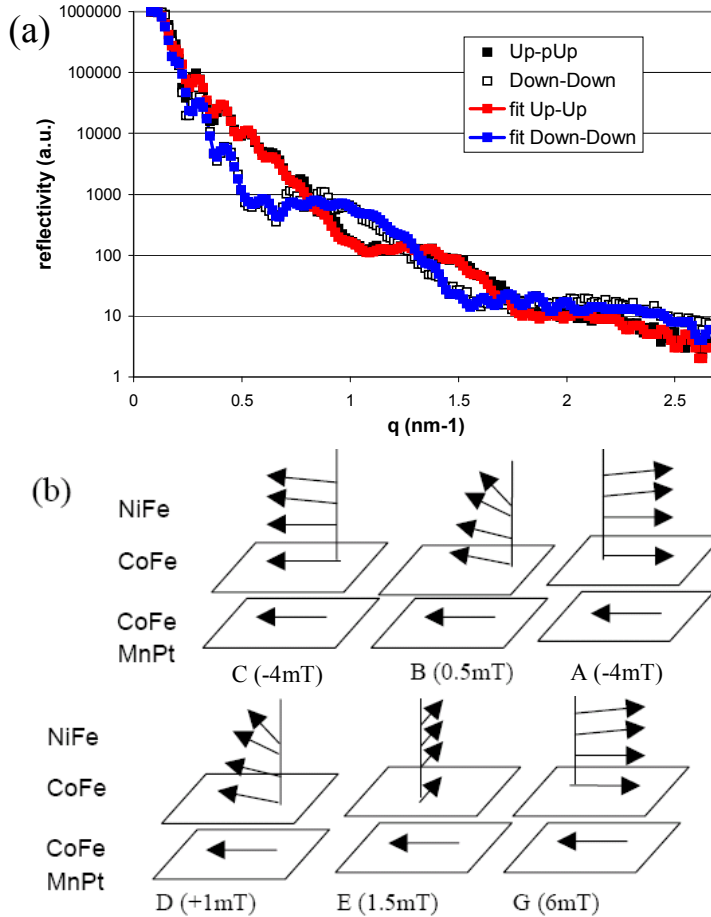
Figure 10.6.: *(a) Reflectivity of the system in a field of 15mT. The curves given correspond to an anti-ferromagnetic arrangement of the two CoFe layers (point A of Fig. 10.5). Black squares : R^{++}, white squares R^{--}, best fit in black line. (b) Evolution of the magnetization direction of the 3 magnetic layers as a function of the applied magnetic field. The letters refer to the positions on the hysteresis loop (see Fig. 10.5). At the points B and D, a magnetization rotation gradient up to 30° in the NiFe layer is observed.*

In order to follow the magnetic configuration as a function of the magnetic field, we have used the procedure described in reference [202]. A first measurement has been performed in a magnetic saturating field. The hard and soft layers are aligned. Spin-flip reflectivity is then very low due to the absence of non collinear magnetic moments. The reflectivity of the system in this magnetic state is given in Fig. 10.6a. We measure a very low roughness (< 0.5 nm RMS). We have then followed the magnetic configuration as a function of the applied magnetic field. The reflectivities have been measured for a small set of angles as a function of the applied magnetic field. Then, using the parameters deduced from

the saturated state, these reflectivities have been adjusted by varying a single parameter: the magnetic direction of the soft layer. It appears during the fit that a homogeneous magnetic configuration in the NiFe layer cannot account for the measured reflectivities.

One needs to consider that a small magnetization rotation occurs inside the NiFe layer. The fit of the curves have been made by cutting the NiFe layer into 3 homogeneous layers of 1.06 nm. The limited intensity in the neutron experiments does not allow a better precision of the NiFe rotation. The evolution of the magnetic configuration of the GMR system is given in Fig. 10.6b. The small rotation of the NiFe, almost non visible in the magnetization curve, is clearly revealed by the neutron reflectometry curves.

Even at 8 mT, the free layer appears to be not fully aligned with the external magnetic field. This effect appears clearly on the SQUID measurements under 6mT, (points A and C on Fig. 10.5) but between A and C a small magnetization rotation gradient exists in the Nife layer which is not detectable by SQUID measurements. The effect of that rotation is to induce a coherent rotation of the free layer, beginning from the bottom (Ta layer) to the top (CoFe layer) during the reversal. This effect avoids any domain formation and therefore leads to low frequency magnetic noise in the sensitive region of the GMR. The maximal angle of rotation of the magnetization in NiFe is fixed by a competition between the anisotropy and the exchange energy. This gives a maximum rotation gradient of about 5° / nm (like in NiFe domain walls) and then about 25° for the total NiFe layer, in reasonable agreement with the maximum rotation observed in the layer ($\sim 30° \pm 5°$). Off-specular neutron scattering did not reveal the presence of magnetic domains. The reflectivity values are also adjusted by using the full nominal moments of the layers suggesting that there is no significant magnetic domain formation even in unpatterned layers.

We have shown how precise can be the determination of the magnetic configuration using PNRPA. Very small rotations of magnetic moments in a specific layer can be determined allowing an in depth understanding of the magnetic evolution of the system under an applied field. In this specific situation, the anisotropies are such that they prevent the formation of magnetic domain and thus optimize the 1/f noise of the GMR sensor.

10.3. Artificial anti-phase boundary at a $Fe_3O_4/CoFe_2O_4$ interface.

The spinel ferrites have become of great interest to the magnetism community due to their potential applications in spintronics devices. Another widely studied topic, particularly in the case of Fe_3O_4, is the effect of antiphase boundaries (APBs) on the magnetic and magnetotransport properties. In the present work, we study the magnetic behavior of a particular $Fe_3O_4|CoFe_2O_4$ bilayer system which could potentially be used in fully epitaxial oxide spin-filter magnetic tunnel junctions. $CoFe_2O_4$ is the magnetic tunnel barrier or spin filter and Fe_3O_4 is the magnetic electrode. The heterostructures are grown by MBE by J.-B. Moussy and A. Ramos from the CEA/SPCSI.

The $Fe_3O_4(15nm)|CoFe_2O_4(5nm)$ hetero-structure exhibits a very specific magnetization dependence. Both magnetic layers switch at rather different magnetic fields (Fig. 10.7). The difference in reversal fields increases strongly when the temperature is decreased. More precisely, in $Fe_3O_4(15nm)|CoFe_2O_4(5nm)$ bilayers, the magnetization

reversal occurs in two steps. The $CoFe_2O_4$ layer reverses first at a magnetic field slightly lower than its usual coercivity, followed by Fe_3O_4 at a magnetic field nearly ten times greater than its intrinsic coercive field. The shape of the room-temperature and low-temperature M-H curves (Fig. 10.7) suggests that as the magnetic field is lowered from the saturated and "parallel" state past zero field, the $CoFe_2O_4$ layer switches quite readily. Once in the "antiparallel" state, a strong exchange field between $CoFe_2O_4$ and Fe_3O_4 stabilizes the system in this configuration, making it extremely difficult for Fe_3O_4 to switch. What is most unique in this system is therefore that the energetically stable or "blocked state" occurs after $CoFe_2O_4$ has switched, which is rare in exchange-coupled systems involving two ferromagnetic or ferrimagnetic layers. Furthermore, the intrinsic coercivities of the $CoFe_2O_4(5nm)$ and $Fe_3O_4(15nm)$ films alone on the order of 200–300 Oe for both are so close that it is impossible to predict which of the two layers should act as the "hard" and "soft" ferromagnets. Only when the two are put directly in contact with each other does it finally become clear that $CoFe_2O_4$ acts as the blocking layer after its own magnetic reversal. The bilayer corresponds to a ferromagnetic-ferromagnetic exchange-coupled system. We analyze here the nature of the magnetic configuration at the interface to shed light on the nature of exchange coupling at the interface of this unique system.
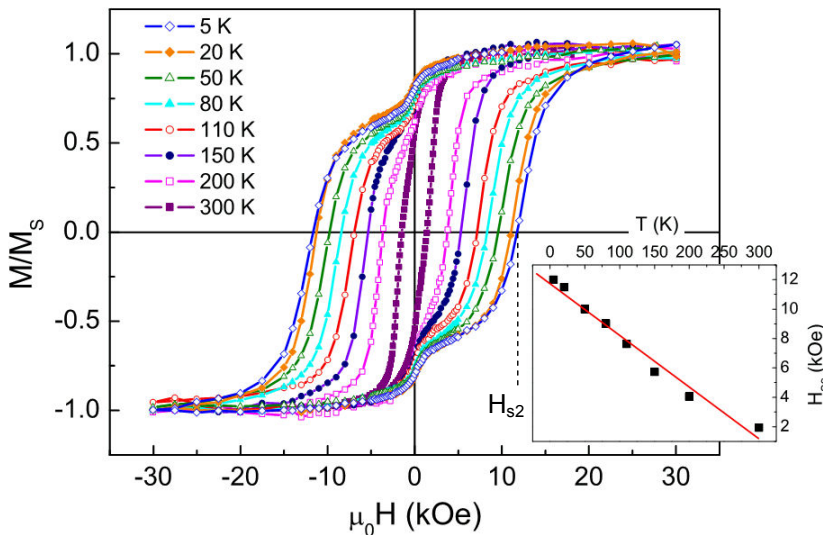
Figure 10.7.: *Magnetization curves for a $CoFe_2O_4(5nm)/Fe_3O_4(15nm)$ bilayer measured at various temperatures. The normalized hysteresis loops are superposed and reveal a linear evolution of H_{s2} as a function of T (inset).*

In this system, one can consider that an artificial APB boundary is created. In such thin films structures, the finite thickness of the layers has to be taken into account. I have performed numerical modeling of the expected magnetization structure at such an the interface. If we consider the case where the $CoFe_2O_4$ is much thinner than the Fe_3O_4 layer, the rotation of the magnetization angle takes mostly place in the thinner layer and the magnetization is barely perturbed in the thicker layer (see Fig. 10.8).

Besides characterizations by standard magnetometry and resistivity measurements, the structure of the different magnetic layers as a function of the applied field has been followed using neutron reflectivity. Figure 10.9 shows a reflectivity measurement during
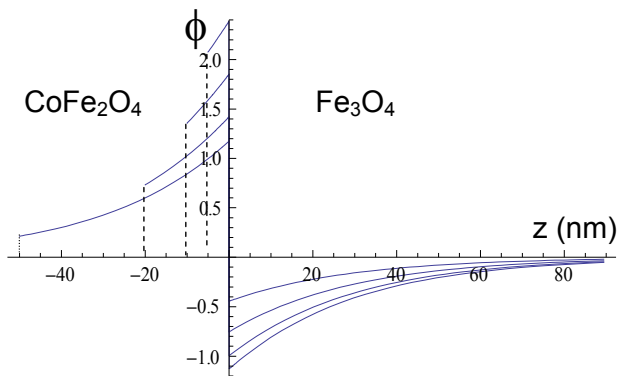
Figure 10.8.: *Rotation ϕ (radians) of the magnetization as a function of the CFO layer thickness (5, 10, 20, 50 nm).*

the reversal of the magnetization at a field of 0.05T coming from a field of -1.2T. The Table summarizes the fitting parameters and shows that we have a partial AF coupling between the $CoFe_2O_4$ and the Fe_3O_4 layer (the magnetizations are of opposite sign). The accuracy of the reflectivity measurements do not allow to be more resolved in the depth profile measurement. The magnetic configurations were measure all along the hysteresis curve and the results of the fitted magnetic depth profiles are presented on Fig. 10.10). It shows that the layer which reverses first is the CFO layer even though this layer has the highest coercivity when it is produced as a single film. During the reversal, between 0.05 and 0.15T, a hint of an AF coupling between the two layers can be observed. Note that the measured value of the magnetization is only the projection of the magnetization along the applied field direction. In this system, chiral structures are indeed expected and so also spin-flip signals. However, in these oxide materials, the in-plane magnetic domain size is smaller than 100nm so that the contributions of domains with different chirality cancel out and the spin-flip signal is zero. It was thus not possible to directly obtain information about the transverse component of the magnetization. The measurement nevertheless shows that the transition region at the interface spans over some 10nm.

H = +0.05 T	t (nm)	b (fm)	μ (μ_B)
$CoFe_2O_4$	1.9	45.1	+0.3
Interface	5.5	48.7	-0.9
Fe_3O_4	18.2	50.9	-1.8
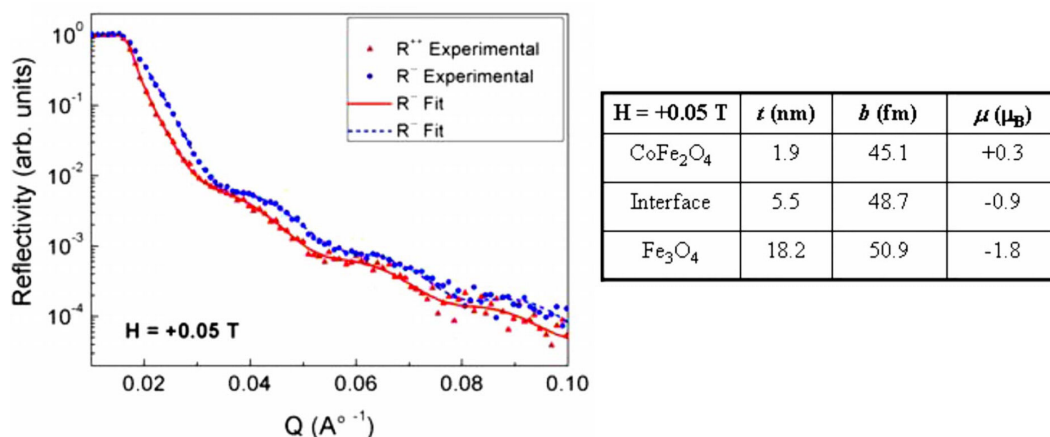
Figure 10.9.: *Room-temperature PNR curves for a $Fe_3O_4(15nm)|CoFe_2O_4(5nm)$ bilayer at +0.05T coming from a negative field $H = -1.2T$. The table shows the fitting parameters used to model the experimental curves.*
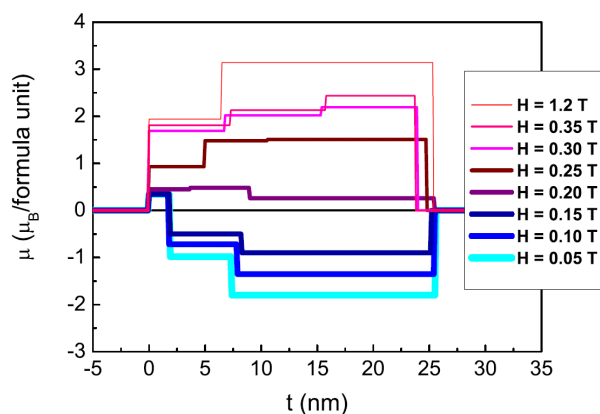
Figure 10.10.: *Magnetization depth profiles obtained from room temperature PNR measurements at different stages of the magnetic hysteresis cycle.*

It is possible to qualitatively explain the observed behavior. The first point to underline is the low coercivity of the $CoFe_2O_4$ layer. This can be explained by the large amount of APB defects in ultrathin $CoFe_2O_4$ films which are known to break the magnetocrystalline anisotropy, thus resulting in a significantly reduced coercivity. Let K_1 (resp. K_2) be the magneto-crystalline anisotropy of $CoFe_2O_4$ (resp. Fe_3O_4). It is first possible to plot the hysteresis cycle of the bilayer system in a simple model taking into account the Zeeman energy, the layer thicknesses and the magneto-crystalline energies. If one takes the bulk K_1 and K_2 values, the resulting hysteresis cycle is plotted as the black solid line on Fig. 10.11a. The coercive of the $CoFe_2O_4$layer is way too high. The value of K_1 has to be strongly reduced (by a factor 10) in order to reproduce the experimental coercive fields. In a second step, an exchange coupling between the layers can be introduced. The exchange constant is taken as $K \times t = 10^{-4} J/m^2$. We observe that H_{s1} shifts to the right and H_{s2} shifts to the left, while the entire magnetization loop remains centered around zero. This behavior is similar to what is observed in the experimental magnetization curves. This analytical model is of course largely simplified with respect to the real system. In particular, it does not take into account the presence of a domain wall at the interface. Nevertheless, by simplifying the analysis to one dimension and three parameters, we qualitatively see the effect of the anisotropy and exchange energies on the magnetization reversal behavior.

The next step is to define the local magnetic configuration at the bilayer interface. The interpretation becomes delicate as none of the experimental methods described above give direct access to this information. To begin, we observe that there is a positive slope in the magnetization curve with respect to the applied field in the range between H_{s1} and H_{s2} both at room temperature and at low temperature. This detail leads us to believe that a domain wall is present at the interface for this field range. In the case of our bilayers system, this would suggest that there exists a progressive rotation of the spins, coupled antiferromagnetically on either side of the interface, toward a parallel or antiparallel alignment depending on the magnitude of the applied magnetic field far from the interface.

65
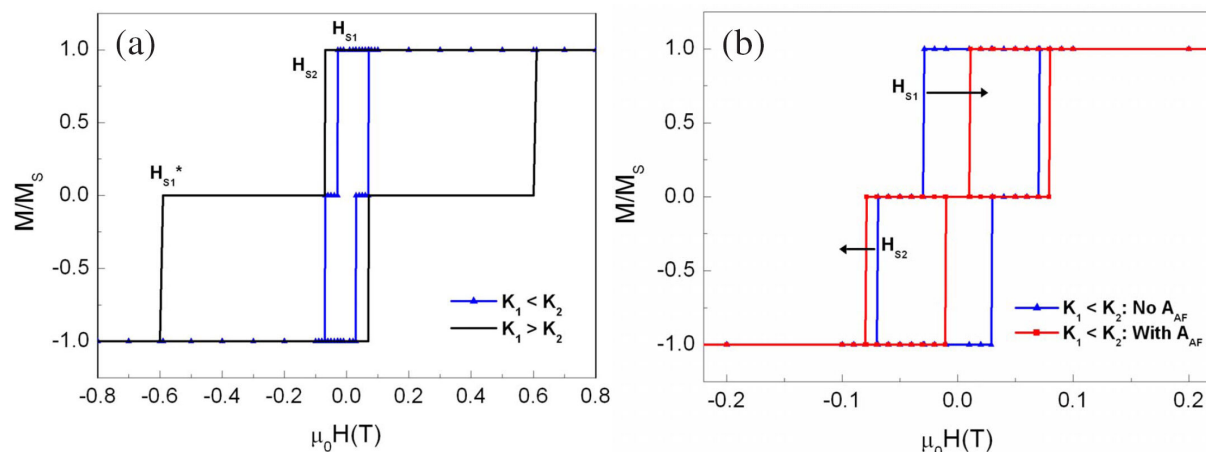
Figure 10.11.: *Magnetization loops obtained by using a simple energy model to calculate the magnetic configuration in $CoFe_2O_4|Fe_3O_4$ bilayers. (a) Effect of the magnetocrystalline anisotropy in $CoFe_2O_4$. (b) Effect of an exchange coupling at the $CoFe_2O_4|Fe_3O_4$ interface in the case of low anisotropy $CoFe_2O_4$. H_{s1} and H_{s1}^* are the switching fields for low and high anisotropy $CoFe_2O_4$ respectively. H_{s2} corresponds to Fe_3O_4.*
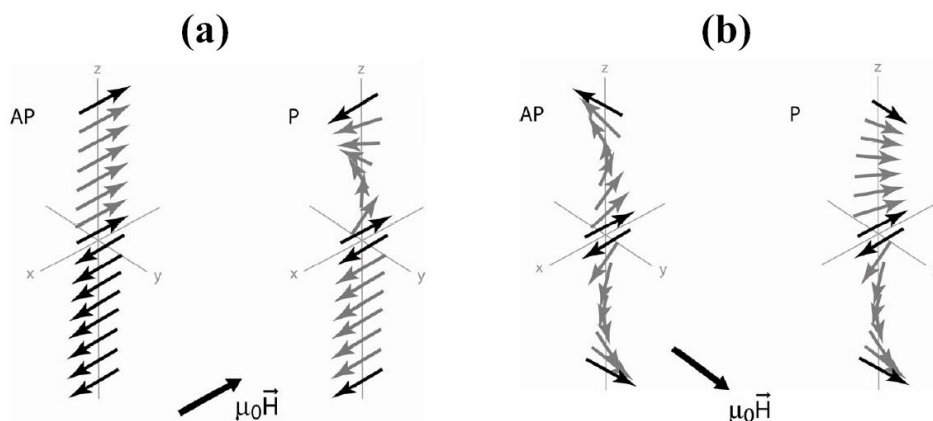
Figure 10.12.: *Schematic illustration of two possible scenarios for the alignment of an AF coupling at the $CoFe_2O_4|Fe_3O_4$ interface with respect to an applied magnetic field: (a) coupling parallel to H ; (b) coupling perpendicular to H. In both cases, the expected local magnetic configuration involves the formation of a domain wall on one or both sides of the interface in order to recover a P or AP state far from the interface.*

Assuming that the AF coupling at the $Fe_3O_4|CoFe_2O_4$ interface is associated to a domain wall on one or both sides and that this AF coupling appears as soon as the bilayer is deposited, there are two possible scenarios for the orientation of an AF coupling with respect to the applied magnetic field: an AF coupling parallel to H or an AF coupling perpendicular to H (see Fig. 10.12a and b). The most favorable configuration minimizing the magnetic energy is a coupling that is oriented perpendicular to the magnetic field (Fig.

10.12b). This is also the only scenario which is compatible with the PNR measurements (which measures the magnetization projection along the magnetic field direction). This configuration also corresponds to the classical APB situation. A quantitative modeling of the detailed spin-structure would however require to have a very good knowledge of the anisotropy constants and the exchange coupling at the interface.

This study was also complemented by detailed magneto-transport measurements. Details can be found in A. Ramos et al [203].

Careful analysis of the magnetic and magnetotransport measurements suggests that the local magnetic configuration at the $Fe_3O_4|CoFe_2O_4$ interface involves a domain-wall-type structure containing two AF-coupled half spin chains, thus generating an artificial antiphase boundary. The unique magnetic properties of this bilayer system therefore make it an interesting candidate for future theoretical studies, as well as spin-polarized transport measurements in spin-filter magnetic tunnel junctions.

10.4. Magnetic stripes in FePd and FePt layers

We present here the first example of a Grazing Incidence SANS experiment on a magnetic thin film [201]. FePt thin film layers self organize themselves in magnetic stripe domains (Fig. 10.15a). The stripes are almost perfectly ordered in a periodic pattern with a period of about $100nm$.

In order to study in-depth this magnetic pattern, we have performed two types of experiments. One of the system which has been studied is a system of $FePd(30nm)/FePd(30nm)$ bilayers is which the bottom layer has an in-plane anisotropy and the top layer has a perpendicular anisotropy. These anisotropies are induced during the MBE growth by tuning the growth parameters. These layers were grown by G. Beutier and A. Marty (CEA/Grenoble). When a single layer of FePt with perpendicular anisotropy is grown, a nicely ordered pattern is observed only in the virgin state. After application of a magnetic field, and return to the remanent state, the pattern is rather disordered. This often makes experiments on ordered stripes systems, one shot experiments. It has been found that using a $FePd$ layer with an in-plane magnetic anisotropy as a buffer for the growth of the perpendicular anisotropy $FePd$ layer not only improves the quality of the ordered state but also make the system reversible when magnetic fields are applied. This makes the system much more interesting for different studies.
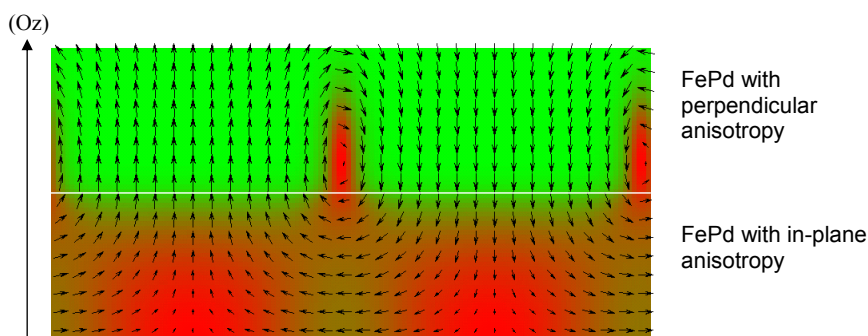
Figure 10.13.: *Simulated magnetic configuration for a bilayer FePd(30nm)/FePd(30nm), side wiew (courtesy of G. Beutier).*

10. Non-collinear and chiral structures in magnetic thin films

The bilayer structure is of course more complex since it mixes two types of magnetic anisotropies. It was thus interesting to study the interaction between the two FePd layers. The first approach was of course to perform micromagnetic simulations (see Fig. 10.13). From the simulations, it can be seen that the stripe pattern (up and down) is still very well defined in the top $FePd$ layer with sharp domain walls between the domains. One should also note that the stray fields from the domains in the top $FePd$ layer strongly disturb the magnetization of the bottom $FePd$ layer. The magnetization of the bottom layer is strongly non colinear and modulated by the above magnetic domains. The resulting magnetization in the bottom $FePd$ layer is rather reduced on average. In order to probe the magnetization in-depth in this system, we have performed polarized neutron reflectivity (PNR) measurements on this system. Figure 10.14 shows the reflectivity of such a system in the remanent state. The simple PNR measurements has limitations since it only probes the in-plane magnetization $M(z)$, averaged over the film surface, i.e. $\iint_{(x,y)} M_{||}(z)$. The magnetic domains are so small ($< 100nm$) that the PNR only probes an average value of the magnetization and is not sensitive to the domain structure.

The profile $M_{||}(z)$ can be calculated from the simulation (Fig. 10.13). $M_{||}$ is very small at the top of the system because only the Néel caps to the in-plane magnetization and the domains do not. At the bottom of the system, the average in-plane magnetization is maximum. The calculated $M_{||}(z)$ profile is plotted is blue on Fig. 10.14b. The PNR data were fitted by dividing the system into slices of 3.75nm. The magentization in these slices was let free to vary. The fit had very little free parameters since the bilayer system is seen as an chemical homogeneous 60nm layer since the change in anisotropy is induced by a small change of the crystallographic structure. One can see that the magnetization profile fit (Fig. 10.14b red) is very close to the simulated data. This is one of the few examples where micromagnetic calculations of in-depth structures can be experimentally probed in a thin film structure.
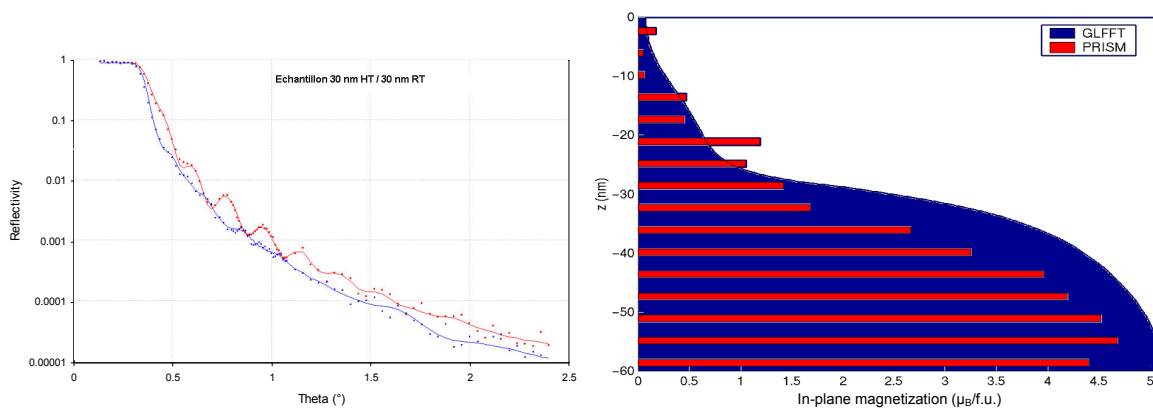
Figure 10.14.: *(a) Reflectivity of a FePd bi-layer 30nm/30nm measured on the spectrometer PRISM. (b) Fit of the PNR data of the average in-plane magnetization and comparison with the simulated magnetic configuration for a bilayer 30nm/30nm (courtesy of G. Beutier).*

Since the system exhibits a magnetic nano-stripe domain structure, it is tempting to perform GISANS experiments. The system was thus studied on the GISANS spectrometer PAPYRUS at the LLB. The neutron beam was sent at grazing incidence ($\theta_{in} = 0.7°$) on

the layer, the magnetic domains being parallel to the incidence plane (Fig. 10.15a). Diffraction from the magnetic domains can be observed. Fig. 10.15b details the different contributions of the Grazing Incidence SANS signal. An integration at fixed q_z has been performed and is presented on Fig. 10.15c. Three diffraction orders can be observed. Note that only odd modes can be observed because the magnetic potential is an even function in the plane of the layer. Mode 2 is extinct. In order to quantitatively model the system, we have shown that it is necessary to take into account both the Néel caps between the magnetic stripes as well as the magnetic stray fields (Fig. 10.16d).

A detailed discussion of this experiment can be found in [202].
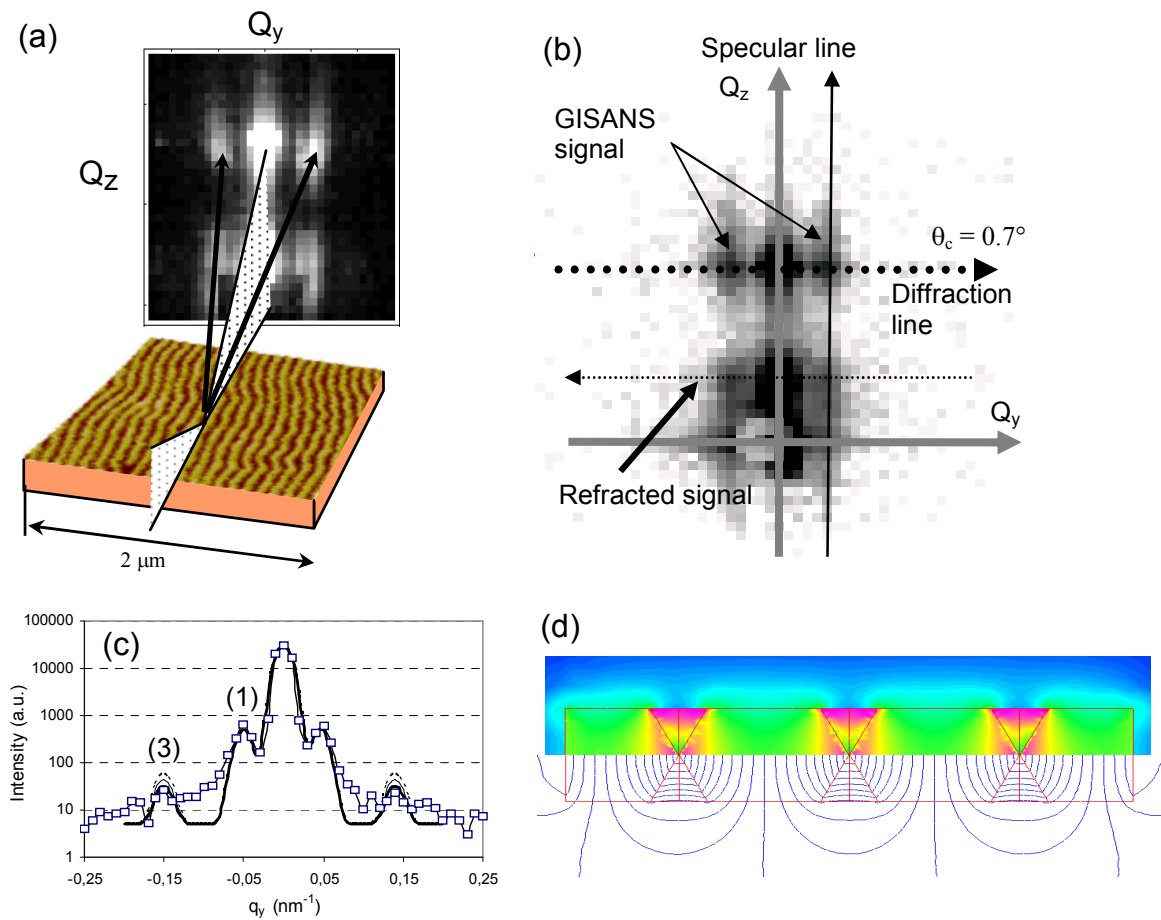
Figure 10.15.: *GISANS signal from a magnetic domains nanostructure. (a) Magnetic Force Microscopy image of the magnetic domain and scattering geometry. (b) GISANS signal on the detector for $\theta_{in} = 0.7°$. (c) Integrated GISANS signal at constant q_z (squares) and fits using different models (lines). (d) Distribution of the magnetic induction in the thin films. The stray field outside the layer are very large and need to be taken into account in the calculation.*
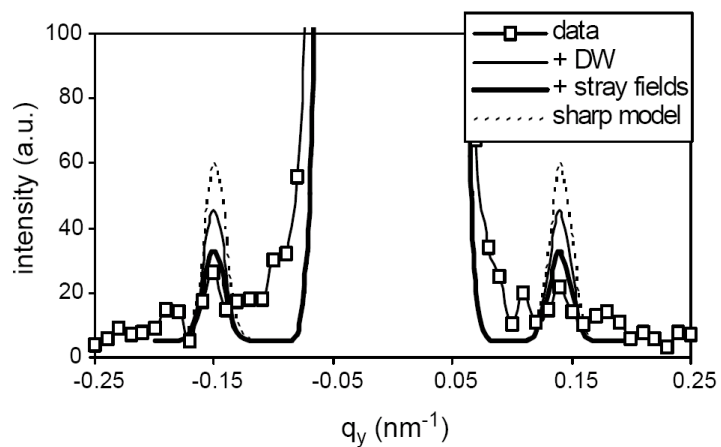
Figure 10.16.: *Cut along the Q_y direction for $\theta_{in} = 0.7°$; experimental points (squares) and simulations for a step function (sharp domain walls model), using the simulated micro-magnetic structure with domain walls (+DW), taking into account the stray fields outside the layer (+stray fields). The intensity ratio between the first and third order can only be accounted for by take into account the stray fields.*

11. Chiral structures in crystals: magnetic domain walls in $La_{0.22}Ca_{0.78}MnO_3$

We present here the characterization of the micromagnetic structure and its link with the magneto-transport properties in $La_{0.22}Ca_{0.78}MnO_3$ single crystals. We show that magnetic domain wall profiles can be measured using SANS scattering. By using a "hopping exchange model" we then show that it is possible to correlate the resistivity properties with the domain wall thickness. This evidences that a large part of the magneto-resistance finds its origin in local magnetic defects with a typical size of the order of a few nanometers.

11.1. Sample

The family of $La_{1-x}Ca_xMnO_3$ manganese perovskites exhibit a complex phase diagram as a function of the stoichiometry x. For $x < 0.17$, the compound is anti-ferromagnetic. For $0.17 < x < 0.25$, various experimental measurements suggest that there is a coexistence of insulating and conducting ferromagnetic phases. For $0.17 < x < 0.22$, the compound is macroscopically insulating. For $0.22 < x < 0.25$, the compound is macroscopically conducting. For $x > 0.3$, the compound behaves as a "good" ferromagnet. We have studied the compound with $x = 0.22$ which exhibits a very peculiar micromagnetic behavior. The $La_{0.22}Ca_{0.78}MnO_3$ compound has a Curie temperature of $189K$ (see Fig. 11.1). When the temperature is decreased, the resistivity increases strongly before the Curie temperature is reached then decreases again very quickly. At lower temperature it increases and decreases again. This second maximum is not associated with any well defined transition. It must be noted that the resistivity of this compound is very sensitive to its history. On the Fig. 11.1insert, the resistivity of a close compound $La_{0.2}Ca_{0.8}MnO_3$ measured for 3 different preparation state is presented. These evolutions suggest that the major part of the resistivity is not due to intrinsic electronic properties but to extrinsic effects and in particular to micro-structural defects. In the following we will show that this resistivity can be explained by the micromagnetic structure.
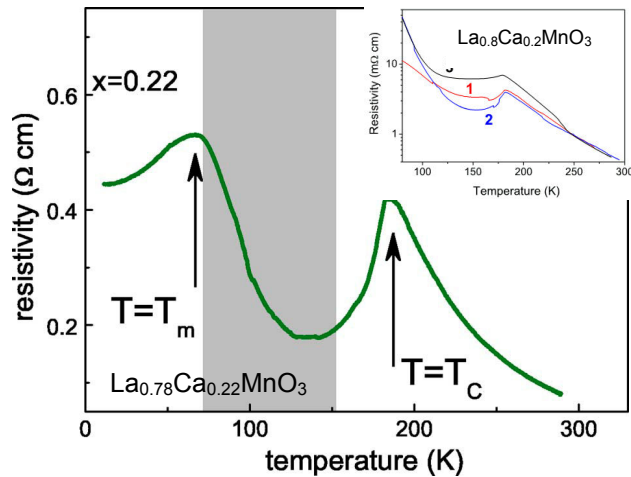
Figure 11.1.: Resistivity of the $La_{0.22}Ca_{0.78}MnO_3$ versus temperature (adapted from [165]). (insert) Resistivity of the $La_{0.2}Ca_{0.8}MnO_3$(adapted from [166].)
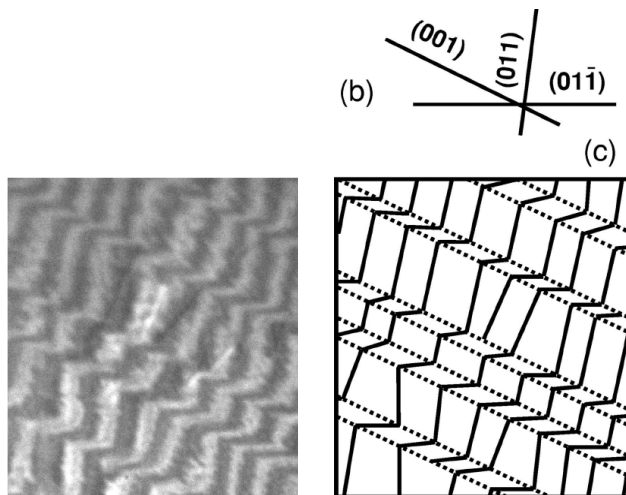
Figure 11.2.: (a) Micromagnetic structure as observed by Kerr imaging. (b) main crystal orientations. (c) mapping of the orientation on the image of the domains (adapted from [165]).

The magnetic micro-structure has been probed by Kerr imaging [165]. Zig-zag structures following the main crystallographic orientations are observed. The zig-zag structure strongly suggests that the magnetic microstructure is pinned on twin defects. The size of the domains is about $50\mu m$ (independent of the temperature). The fact that the size of the domain remains stable over a wide range of temperature suggest that they are connected to structural defects. It can be noted that a typical size for the twinning is of the order of $100\mu m$. When the temperature is lowered further, new mechanical strains appear and thus new defects. This gives rise to new micromagnetic sub-structures (not shown). The magnetic remanence of the system is zero. The micro-magnetic domains structure is perfectly reversible.

11.2. Experimental

The crystal was characterized by Small Angle Neutron Scattering (SANS) on the spectrometer PAPYRUS at the Laboratoire Léon Brillouin with the aim to probe the magnetic domain walls structure. The SANS signal was followed as a function of the temperature in a Zero Field Cooled procedure (ZFC). At $200K$, a small parasitic signal can be observed. At $T_c = 190K$, a strong diffuse scattering appears which concentrates over smaller and smaller Q values while the temperature is decreased. The scattering is rather isotropic. In order to perform quantitative comparison, the signal was circularly integrated.
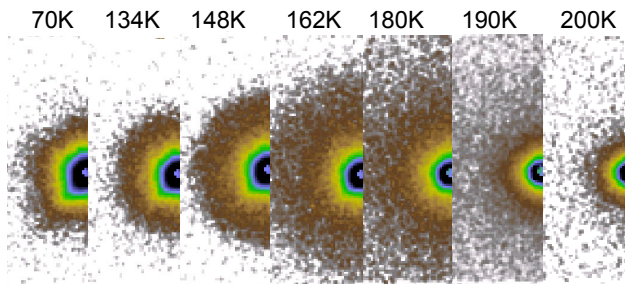
Figure 11.3.: Evolution of the SANS scattering under ZFC.
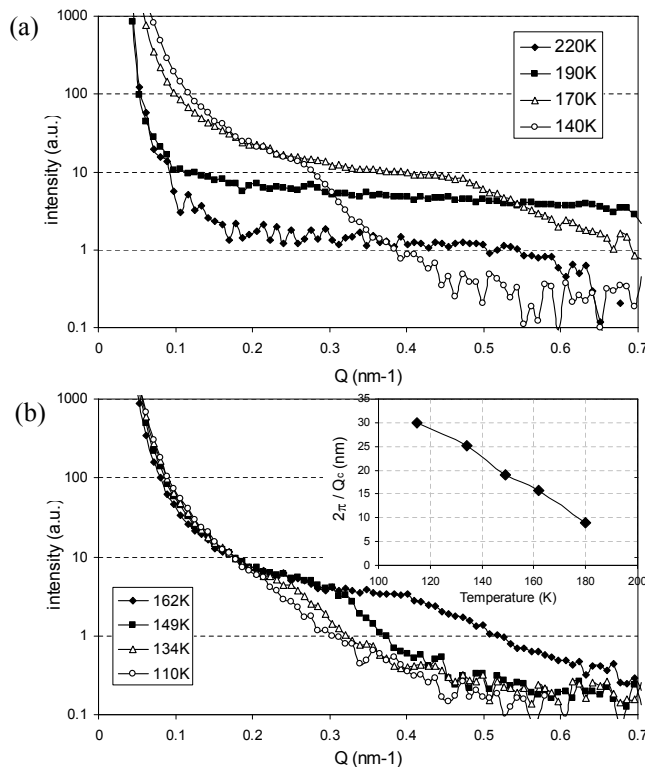
Figure 11.4.: Evolution of the scattering under ZFC (1D circular sum over the SANS data). (a) Around the Curie temperature. (b) Below the Curie temperature. (insert) Evolution of the inverse cut-off wave-vector as a function of the temperature. The dependence is linear.

Fig. 11.5a illustrates the situation when the Curie temperature is crossed during the ZFC. Above T_c, the scattering is very low. At T_c, magnetic diffuse scattering is observed which extends over the whole accessible Q range (up to $0.7\,nm^{-1}$). When the temperature is lowered well below T_c, down to $170K$, the diffuse scattering still increases but a cut-off scattering vector appear around $0.5\,nm^{-1}$. When the temperature is further lowered, the cut-off frequency shifts to lower values ($0.27\,nm^{-1}$ at $140K$). Fig. 11.5b illustrates the evolution of the cut-off frequency as a function of the temperature. The dependence of the inverse cut-off wave-vector $2\pi/Q_c$ is linear (see insert in Fig. 11.5b). For temperatures below $100K$, the SANS signal does not evolve anymore even though the resistivity measurements suggest that a second transition takes place.
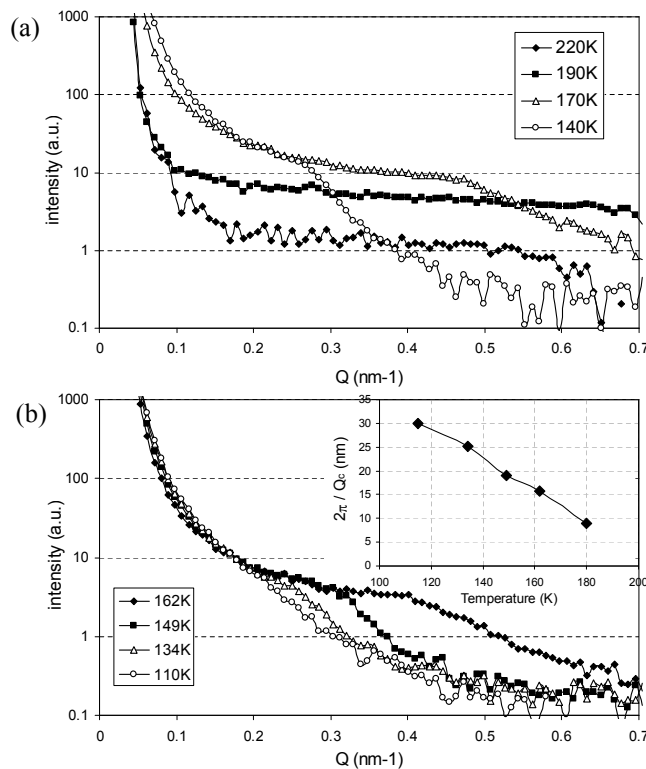
Figure 11.5.: Evolution of the scattering under ZFC (1D circular sum over the SANS data). (a) Around the Curie temperature. (b) Below the Curie temperature. (insert) Evolution of the inverse cut-off wave-vector as a function of the temperature. The dependence is linear.

At low temperatures, the signal asymptotically converges towards a $1/Q^4$ dependence (see Figure 11.6a) following a Porod law. This suggests that the scattering takes place on interfaces [169].

It is possible to calculate the scattering invariant $I.Q^2 = \int I(Q).Q^2dQ$ of the different curves. Over the whole temperature range, the scattering invariant is constant (Fig. 11.6b). This suggests that only the shape of the scattering structures evolves as a function of the temperature but not their topology [169]. That is, only the shape of the domain walls are modified with the temperature, not their number. The integrated surface of the interfaces is preserved when the temperature is varied.
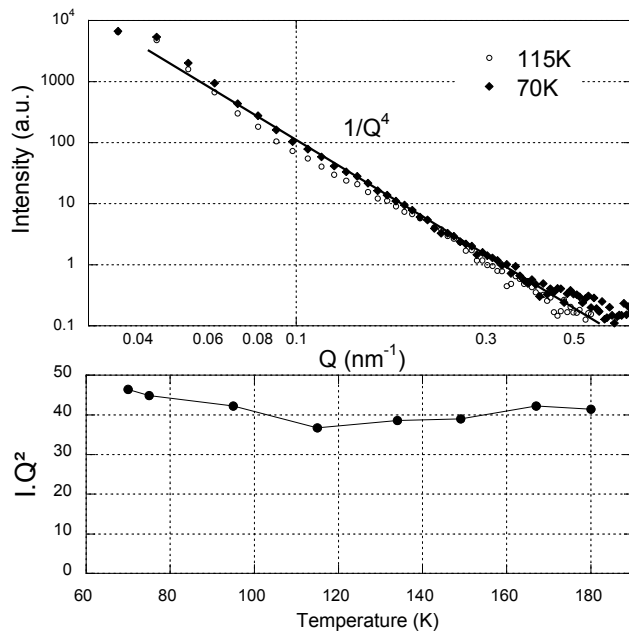
Figure 11.6.: (a) Intensity versus Q in a Log-Log representation for low temperature measurements. (b) Scattering invariant $I.Q^2$ as a function of the temperature.
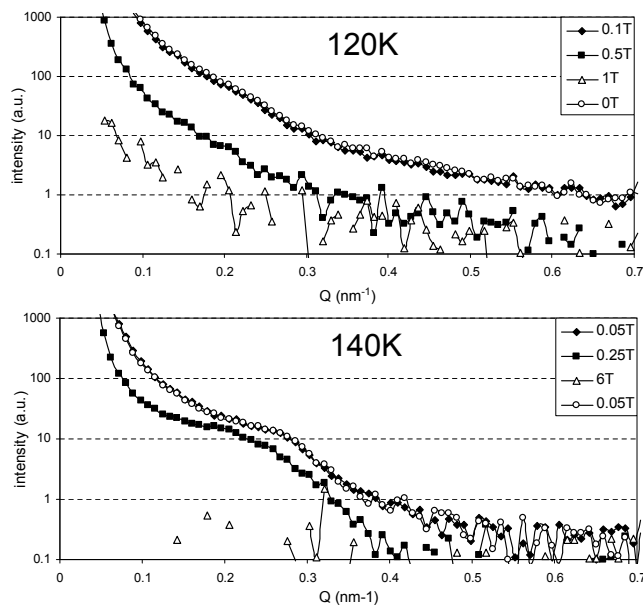
Figure 11.7.: Evolution of the SANS signal under an applied magnetic field at $120K$ (a) and at $140K$ (b). Note that after the application of a $6T$ field, the SANS signal is perfectly reversible (b).

The SANS signal was also measured as a function of the applied magnetic field (Fig. 11.7). The SANS scattering decreases when a field of a few kG is applied and disappears under a magnetic field of approximately $1T$ (Fig. 11.7a). It should also be noted that the scattering signal is perfectly reversible even after the application of a $6T$ field (Fig. 11.7b). This is coherent with the Kerr effect observations. The domain walls always reappear at

the same positions.

11.3. Discussion

We have gathered the following observations:

(i) A strong scattering is observed at the Curie temperature suggesting that it is of magnetic origin.

(ii) The scattering disappears and is reversible under an applied magnetic field. Thus the scattering does not originate from a chemical contrast.

(iii) The low temperature $1/Q^4$ dependence suggests that we have scattering *interfaces* which are likely to be the interfaces between magnetic domains.

(iv) The scattering form factor evolves as a function of the temperature.

All these observations prove that we are indeed measuring the local magnetic structure of the interface between two domain walls. A jump in scattering length exists between two domains of magnetization $+M$ and $-M$. The interface between two domains evolves with the temperature. When a magnetic field is applied, it overcomes the magneto-crystalline anisotropy and the magnetizations of adjacent domains becomes collinear. Thus the scattering contrast disappears.
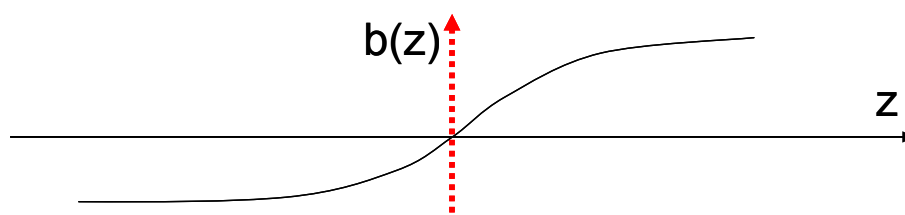
Figure 11.8.: Smoothly varying potential b(z) across an interface.

It can be shown that in the case of a non sharp interface perpendicular to (Oz) (Fig. 11.8), that is, with a scattering length $b(z)$ varying continuously across the interface, the scattered intensity can be expressed as [170]:

$$I(Q) \propto \frac{1}{Q^4}|F(Q)|^2 \ with \ F(Q) = \int_{-\infty}^{\infty} \frac{db(z)}{dz}e^{iQz}dz$$

$F(Q)$ is called the effective form factor of the interface and contains the information about the smoothness of the interface. For a sharp interface, $db/dz = \delta(z)$ so that $F(Q) = 1$, and we find the classical Porod law $I(Q) \propto 1/Q^4$. This is what is observed at low temperatures in our measurements (see Fig. 11.6a). Using our SANS data it is possible to plot the effective form factor of the domains walls $|F(Q)|^2 \propto I(Q).Q^4$ (see Fig. 11.9).

In the case where the variation of the SLD across a surface can be described by an *erf* function (which typically corresponds to a gaussian roughness), the SLD gradient is a gaussian $db/dz \propto e^{-(z/\sigma)^2}$ and thus the effective form factor is also gaussian $F(Q) \propto e^{-(Q\sigma)^2}$. In our case the effective form factor has a much more complicated shape since it has a clear peak at finite Q values suggesting that the SLD variation across the interface is rather complex. It is not possible to perform a direct inversion of this effective form factor. We have thus considered a first approach which consists in using reflectivity modeling to
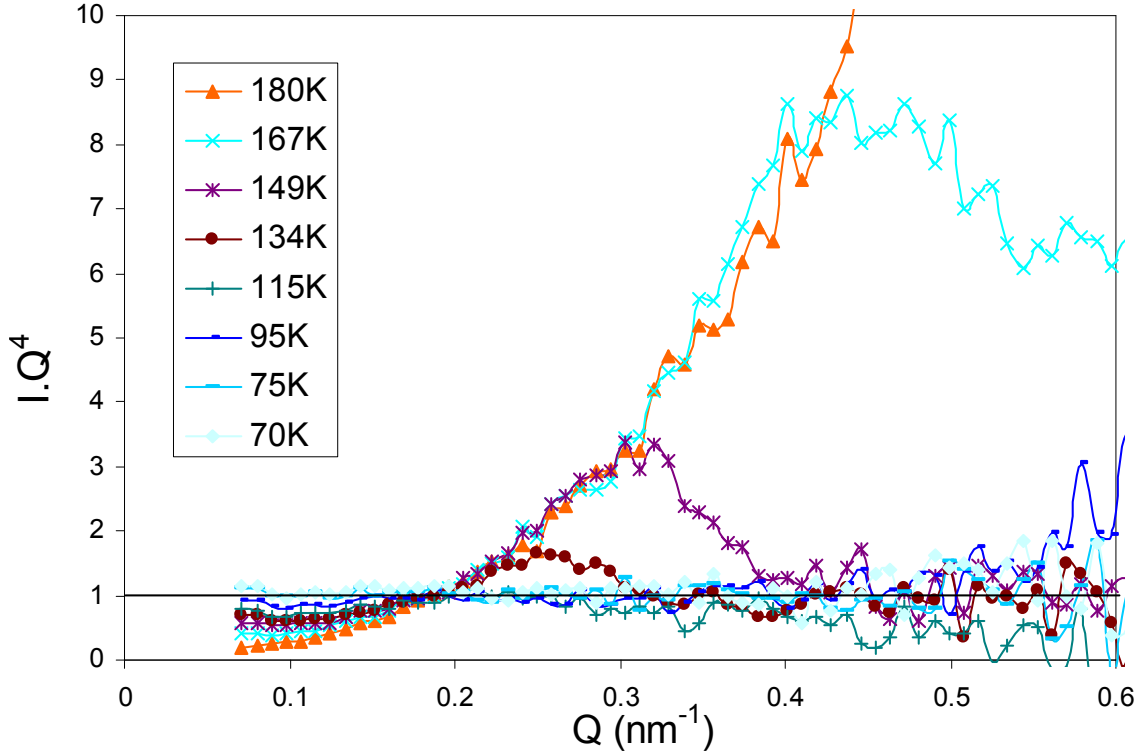
Figure 11.9.: Effective form factor $|F(Q)|^2$ of the domain walls for different temperatures.

account for the data. The $I(Q)$ signals were fitted using a model free stacking of layers. The fitted data are presented on Fig. 11.10a. For technical purposes, the experimental data points have been oversampled and the curves have been smoothed. The SLD profiles across the interface are presented on Fig. 11.10b. These curves should be considered as qualitative models since the data Q-range is very limited. Nevertheless, it provides 2 key information: (i) the width of the interfacial region ($9\,nm$, $13\,nm$, $23\,nm$ for $180\,K$, $167\,K$ and $149\,K$ resp.). These values are the same as the one determined by calculating $2\pi/Q_c$ (see Fig. 11.5insert); (ii) the variation of the SLD across the interface looks anti-symmetric. This suggests *an anti-ferromagnetic coupling at the interface*. The amplitude of the SLD modulation is of the order of $3 \times 10^{-6} \text{Å}^{-2}$ which is compatible with a variation from $+M$ to $-M$ with $M = 3.5 \mu_B/unit\ cell$.

Considering the previous data, it is possible to model the SLD variation across the interface using analytical functions. A first possible function could be $b(z) \propto {x}/{d^2}\, e^{-(x/d)^2}$ where d characterizes the thickness of the interface. The SLD gradient is then given by ${db}/{dz} \propto {1}/{d^2} e^{-(x/d)^2} - {2x^2}/{d^4}\, e^{-(x/d)^2}$. The normalization of the SLD profile $b(z)$ by the factor $1/d^2$ is such that $\int |b(z)|\, dz = Cte$. At this point, this has no physical justification except for the fact that it is required so that the calculated effective form factor follows the experimental measurement. Another possibility is to consider the functions $b(z) \propto {x}/{d^2}\, e^{-|x|/d}$ and ${db}/{dz} \propto {1}/{d^2} e^{-|x|/d} - {|x|}/{d^3}\, e^{-|x|/d}$. The typical variations of these functions is presented on Figure 11.11. The d parameters have been chosen so that the calculations reproduce the experimental data presented on Figure 11.9. Both analytical models provide very similar results which catch most of the features of the experimental data. It is possible to reproduce the peak position, the overlap of the curves for small Q values, and

the relative intensities between the different curves (within 50%).
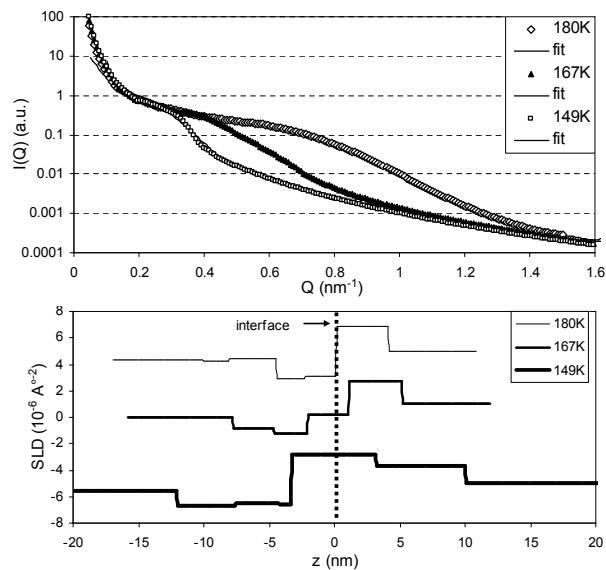
Figure 11.10.: (a) SANS signal at different temperatures fitted using a reflectivity model. Note that the experimental curves have been resampled and smoothed. (b) Profiles of SLD across the interface in the reflectivity fits.
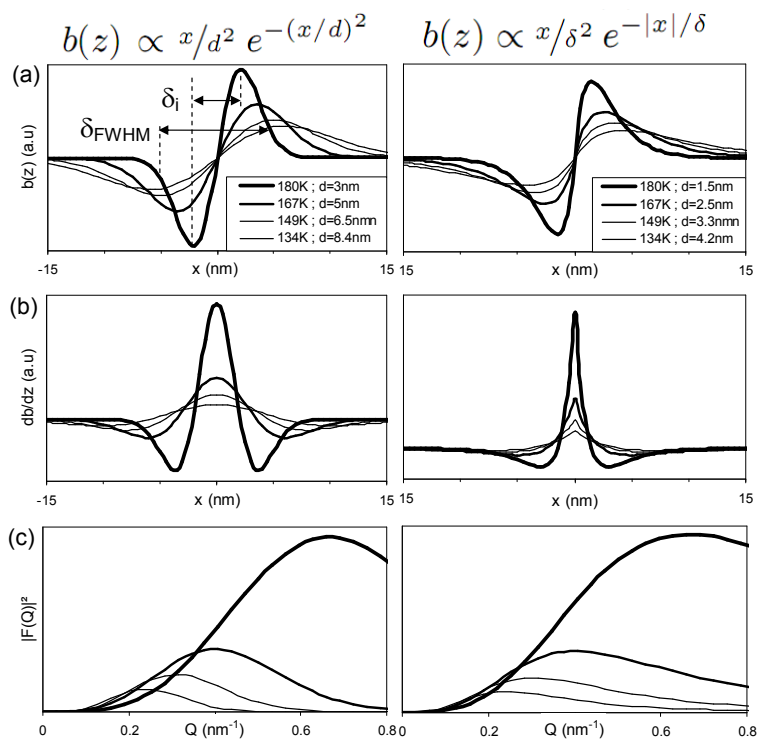
Figure 11.11.: (a) Model of the SLD profile across an interface; (b) SLD gradient across the interface; (c) Effective form factor calculated using these models of the domain wall. (left column) for the model $b(z) \propto x/d^2 \, e^{-(x/d)^2}$; (right column) for the model $b(z) \propto x/\delta^2 \, e^{-|x|/\delta}$.

The first analytical form provides a symmetrical variation of the magnetization. The second form provides a sharper interface and magnetization variations which extend deeper in the material. This last model is close to an anti-phase boundary model. However, we should mention that the simple analytical form $b(z) \propto sign(x)/d^2\, e^{-|x|/d}$ leading to $db/dz \propto -1/d^3\, e^{-|x|/d}$ which is usually used to model anti-phase boundaries does not reproduce at all the peak in $|F(Q)|^2$ at finite Q values. This emphasizes the fact that one of the key feature is the interfacial region in which a sharp change of the magnetization occurs.

We define the width δ of the transition region by the FWHM of the $b(z)$ profile. We define the width δ_i of the transition region by the peak to peak distance of the $b(z)$ profile. δ_i is related to d by $\delta = 1.4d$ for the first model and $\delta = 2d$ for the second model. The characteristic sizes of the domain walls are plotted on Figure 11.12. One can note that the value given by the maximum peak position $2\pi/Q_c$ corresponds to the domain width δ. The interfacial region is much more narrow ($2.5\times$) but follows the same variations.
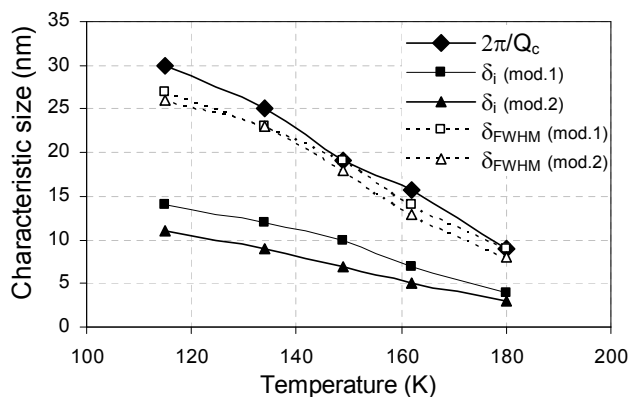
Figure 11.12.: Characteristic widths of the model as a function of the temperature.

The measured characteristic sizes for the interface profiles (ranging from 3 to $20\,nm$) are not compatible with pure Bloch walls which have a typical size of $100\,nm$. In order to explain such short length-scales it is necessary to consider that the magnetic exchange is significantly reduced in this interfacial region. This is very plausible since it has been observed that interfacial regions in manganites are magnetically very disturbed [86]. The characteristic size of the domain walls follows $\delta \propto \sqrt{A/K}$. When the temperature is decreased, the exchange increases and thus the characteristic size of the domain wall increases. Any change in the magneto-crystalline anisotropy is likely to be dominated by changes in the exchange constants. We could also underline the possible role of the mechanical constraints on the twins when the temperature is varied. When the temperature decreases, the mechanical constraints on the twin increases so that the magnetic exchange is more disturbed and so the thickness of the wall increases.

We have shown that a complex, localized magnetic structure is established in the compound at twin boundaries. The characteristic length of such defects being of the order of a few nanometers is such that it plays a significant role on the electrical tunnel transport.

Figure 11.13 shows possible configurations of the magnetization at the domain wall interfaces. The local coupling at the domain wall interface is supposed to be anti-ferromagnetic.
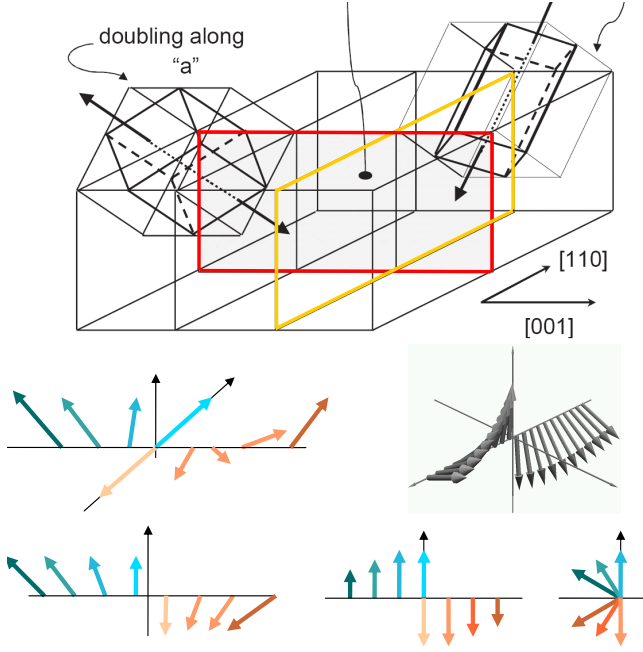
Figure 11.13.: Sketch of the magnetization variation at a domain wall boundary.

11.4. Magneto-resistance of a domain wall

We will now correlate the measured domain wall configuration with the magneto-transport properties. In manganese oxides, the electrical transport is governed by a Variable Range Hopping mechanism (VRH). The electrical resistivity follows the dependence $\rho = \rho_0 \, exp \, (T_0/T)^{1/4}$ with $k_B T = 171\alpha^3 U_m \nu$ where U_m is the Hund potential, and α is a localization parameter [168]. It is possible to model the resistivity of the compound above T_c with a VRH dependence using the parameters $T_c^{1/4} = 63$ and $U_m = 0.5 \, eV$ (Fig. 11.1blue line). In the case of the ferromagnetic compound $La_{0.3}Ca_{0.7}MnO_3$, the parameters are $T_c^{1/4} = 90$ and $U_m = 2 \, eV$, suggesting that the parameters that we have obtained are realistic.

Below the Curie temperature, the drop in resistivity cannot be explained by a simple double exchange model because the measured resistivity is dominated by extrinsic effects. The previous discussion suggests that the electrical transport is dominated by tunnelling effects across magnetic interfaces. We propose to model the tunnel transport across the magnetic interface using a *hopping exchange* model [167]. If one considers two Mn^{4+} ions whose magnetizations make a relative angle θ_{ij}, in a double exchange model the hopping probability is proportionnal to $(1 - cos \, \theta_{ij})$ and the localization potential is given by $E_m = \frac{1}{2}U_H \, (1 - cos \, \theta_{ij})$.

The measured domain wall profile is rather complex (Fig. 11.11) and the variation of $\theta_{ij}(z)$ across the interface is non monotonous. In order to simplify the problem, we will consider the model Nr. 2. In this model, the magnetization variation is the sharpest between the 2 peaks (over the width δ_i) and this part of the domain wall will dominate the resistivity properties (to the first order) since the hopping process has an exponential dependance upon the magnetic potential. Let $\Delta\theta$ be the angular change of the magnetization from one peak to the other and a the distance between adjacent Mn ions (Fig.
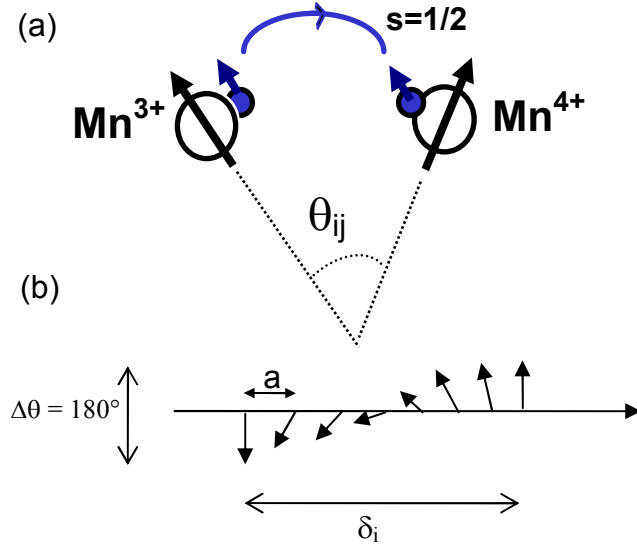
Figure 11.14.: (a) Hopping exchange mediated by a free electron hopping from site to site. (b) Across the magnetic interface, the magnetization angle between Mn ions varies continuously.

11.14b).

Across the domain wall, the change in magnetization angle between Mn^{4+} ions can be approximated by $\theta_{ij} = \Delta\theta\ a/\delta$. The magnetic localization potential is thus $E_m = \frac{1}{2}U_H\left(1 - cos\left(\Delta\theta\ a/\delta\right)\right) \approx \frac{1}{4}U_H\left(\Delta\theta\ a/\delta\right)^2$. The approximation is justified by the fact that the angular variations between Mn ions are not too large since the magnetization varies continuously. Following the VRH model, we thus propose that the hopping transport across the interface can be described by the following formula:

$$\rho = \rho_0\ exp\left(T_0\left(\Delta\theta\ a/\delta\right)^2/T\right)^{1/4}$$

In this model, if δ increases, the resistivity decreases. It corresponds to the resistivity versus temperature dependance. If the magnetization angle between adjacent domains decreases, the resistivity decreases. This corresponds to the negative magneto-resistive effect (see Fig. 11.16).

We have used the above model to reproduce the resistivity data measured between the second transition (above $T_m = 70K$) and the Curie temperature. We have considered too effects: (i) a magnetic hopping transport following the above equation to account for the drop in resistivity below T_c which arises from the fact that the domain wall width δ increases when the temperature is decreased; (ii) a VRH behavior above T_m to account for the increasing resistivity at low temperature $\rho_c = \rho_0'\ exp\left(T_0/T\right)^{1/4}$. A reasonable modeling of the data could thus be obtained (see Fig. 11.15).

When a magnetic field is applied on the system, the magnetization angle difference between the domains decreases so that the height of the interfacial step decreases. The magneto-resistivity data are not very sensitive to an applied magnetic field. The coupling angle barely changes (from 180° to 170°) for fields up to 2T. This is also only compatible with an AF coupling at the interface. When a magnetic field is applied, the domain walls
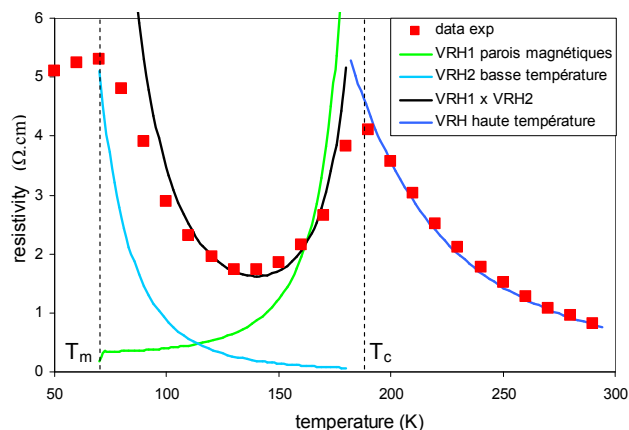
Figure 11.15.: Modeling of the resistivity variations. Above T_c, the resistivity can be modelled using a VRH dependance (blue line). The resistivity decrease above T_m is also modelled using a VRH dependance (cyan line). The hopping transport model using the measured variation of the domain wall width δ gives the green variation. The product of the two VRH contributions below T_c can reasonably account for the temperature resistivity dependance (black solid line).

are not destroyed, but as soon as the applied field becomes higher than the anisotropy (a few kG), the magnetic moments are aligned. This leads to a decrease of the contrast between the magnetic domains that is a decrease of the $1/Q^4$ signal. However, the interface continues to exist and the shape of the effective form factor is unchanged (see Figure 11.16b). The position of the maximum is slightly shifted to smaller Q values suggesting that the interfacial region increases in size. This can be explained by the fact that the magnetic moment in adjacent domains have to perform a larger rotation. Under zero field, the magnetization has to rotate by 45° at the interface (see Figure 11.13); when the magnetic moments in adjacent domains are aligned by the magnetic field , they have to rotate by 90°at the interface leading to an overall wider magnetic interfacial region.

11.5. Conclusion

Using SANS we have been to measure the localization and extension of magnetic defects in a magnetic crystal. We show that the disorder at the twin domain boundaries leads to an anti-ferromagnetic coupling of the magnetization between the grains. We have been able to quantitatively model the resistivity of the compound by considering the magnetic hopping through the magnetic domain walls. We think that this is the first report of the direct measurement of the magnetic domain wall structure in a magnetic crystal.
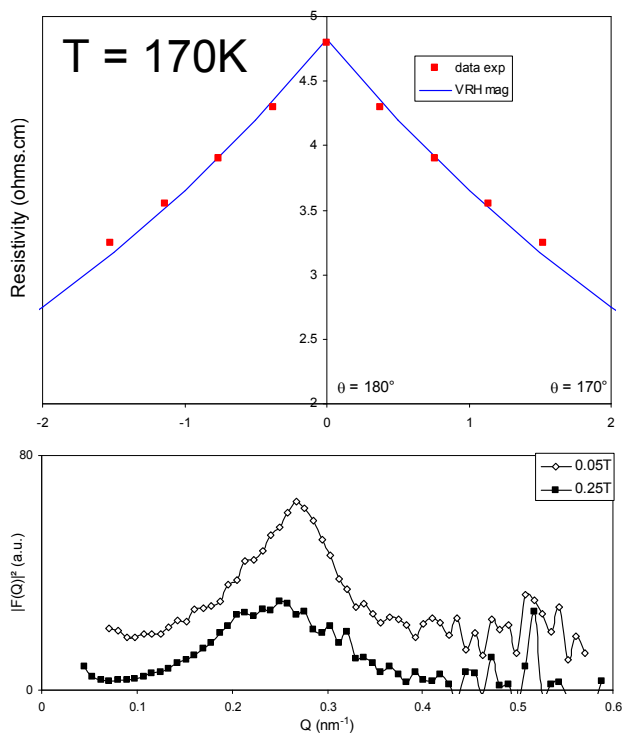
Figure 11.16.: (a) Magneto-resistance. (b) Effective magnetic form factor at $140K$ after application of a magnetic field of $0.25T$. The shape of the form factor is not affected by the applied field.

11. *Chiral structures in crystals: magnetic domain walls in $La_{0.22}Ca_{0.78}MnO_3$*

Part III.

Instrumentation and software developments

12. Instrumentation developments

During the 1990s and 2000s, the reflectometers have been developed following traditional schemes, either using dispersive $\theta/2\theta$ mode or the Time of Flight technique. Most reflectometers have or will soon converge towards optimized versions in these modes. Further progresses will then be asymptotic since in their present configuration, almost all the phase space is used and thus very little flux gains can be further expected.

Specular reflectivity measurements are now performed in a matter of hours. Typical experimental runs last between a few days to 7 days and allow to gather two dozens of experimental measurements. Shortening the acquisition times on neutron reflectometers would provide several improvements : (i) it could be used to perform more experiments and increase the number of users but this would however have limits since the sample environments are often complex to set-up; (ii) measuring reflectivities up to large Q values in order to probe very thin structures (down to the nm); (iii) a higher flux could be used to study the behavior of materials in-situ, following their properties or conformation as a function of external parameters such as the temperature, the magnetic/electric field, the shear, the pressure, the humidity etc... and possibly to study slow kinetic effects.

During the last years I have been evaluating different technical principles which could provide gains of one to two orders of magnitude in flux on neutron reflectometers.

In a first part I will present the SimulSpectro modeling tool which has been developed to quantitatively evaluate these new instrumental concepts. I will then quickly describe the general principles of the different concepts and conclude with a discussion of the merits of the different proposed solutions.

The developments of these new implementations will be supported in 2008-2012 by a European Research contract "Neutrons Optics" which I am coordinating. This research network gathers most of the European neutron facilities (FRM2, HMI, ILL, JCNS, BNC).

12.1. Monte-Carlo modeling tool

Several neutron Monte-Carlo simulation packages are nowadays available for users: McSTAS [171], Vitess [172], ResTRAX [173]. They are all based on a "pipeline" description of spectrometers. The neutrons are created in a source, then travel through successive optical elements and are eventually detected. This is fine as long as the design of the spectrometer is restricted to standard optical elements. Creating new optical elements requires to write specific C-code. The main drawback is the sequential philosophy which prevents a neutron coming from the optical element 1 and interacting with element 2 to interact back with element 1. This fundamentally prevents the simulation of complex assemblies of mirrors for example (Fig. 12.1c).

Thus in order to perform Monte-Carlo simulations of advanced spectrometer concepts, I have developed a specific 2D Monte-Carlo ray-tracing program. Since this program was to be used for reflectometry problems, it is limited to a 2D geometry. In the *SimulSpectro*
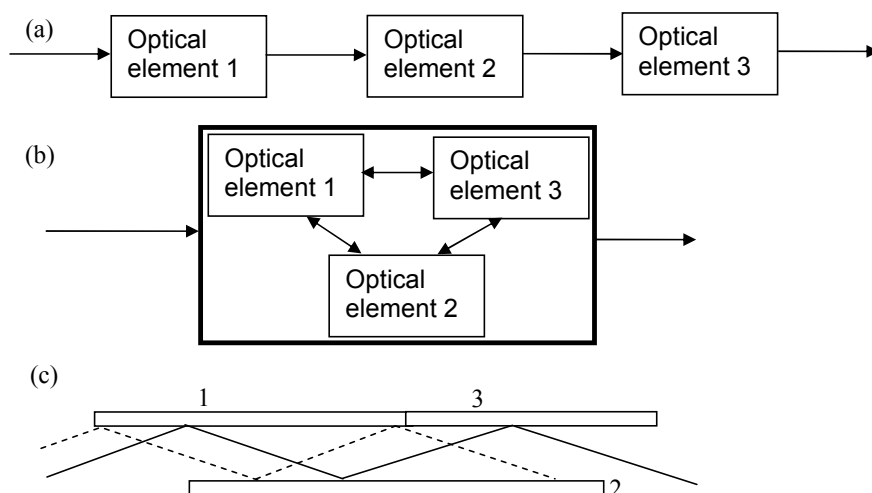
Figure 12.1.: *(a) Pipeline philosophy. The neutrons travel from one element to the other. (b) Multiple interaction description. The* SimulSpectro *program calculates what is happening in the bold rectangular box. (c) Very simple case illustrating the limitation of the pipeline philosophy. The solid line trajectory is fine since it goes from element 1 to 2 and then 3, however, the dotted trajectory travels from 1 to 2, back to 1 and then to 2 which cannot be described using method (a).*

package, the basic concept which defines optical elements are frontiers. Each optical element is a segment with a front side and a back side separating two mediums with different scattering lengths. A neutron incident on this segment is scattered following the scattering function $S(Q)$. It is thus possible to use a unified description for a large range of optical elements: slits, reflection mirrors, transmission mirrors, prisms, samples, detector, entrance in a magnetic field region. The core Monte-Carlo code is thus very simple since it is a simple recursive algorithm which at each step figures out which is the next optical element with which the neutron will interact.

The *SimulSpectro* package provides features not available in other existing programs : refractive optics, graded mirrors, handling of magnetic fields, possibility to design very complex assemblies, scattering function $S(Q)$ for any optical element. In addition, for specific cases, it is possible to use a time dependent $S(Q)$ function which can be used in problems involving choppers or more complex time dependent effects. The scattering function $S(Q)$ simply needs to be loaded either from experimental measurements (reflectivity of supermirrors for example) or from external calculations if the optical element does not yet exist. It is possible to input a 2D $S(Q)$ function which is usually used to describe off-specular scattering from reflective optics.

The description files are saved as Excel sheets. Complex macro commands can thus be used to generate very complex assemblies of objects (gathering tens of segments). This is for example the case of Clessidra type lenses [174] which can be automatically generated using a properly written Excel macro-command. This permits quick prototyping of complex geometries. The program provides a visual output of the ray-tracing which permits to immediately spot issues either in the model or in the concept. For example, in the case
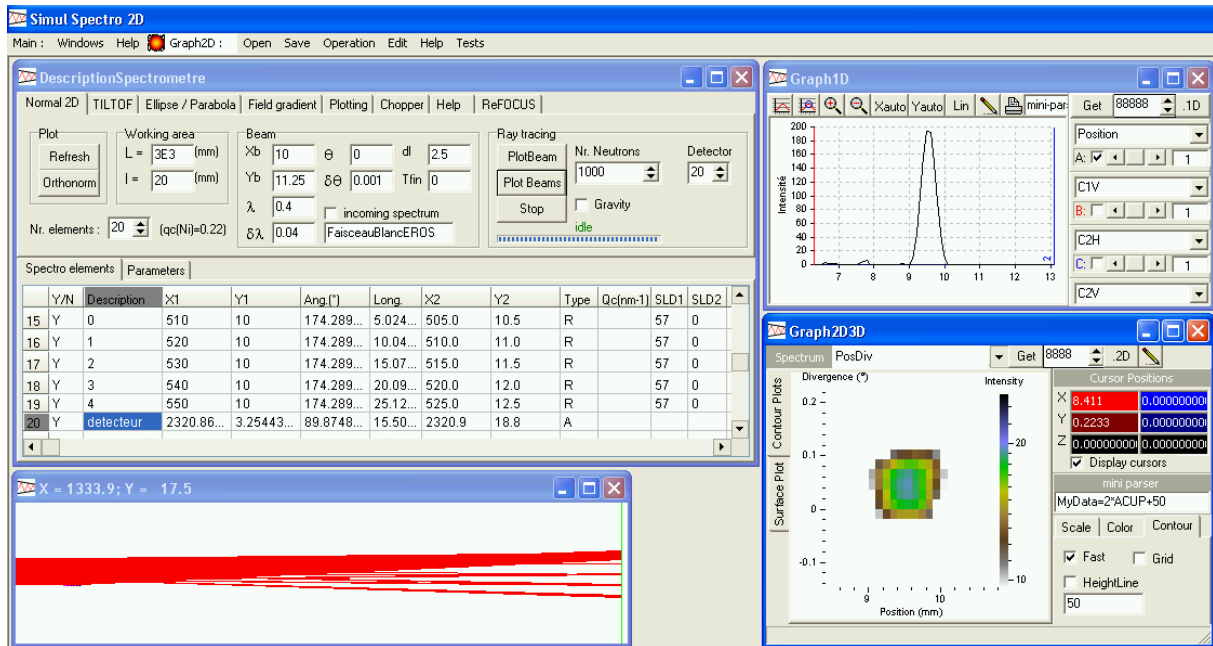
Figure 12.2.: *SimulSpectro interface. (upper-left) A table describes the different segments; (down-left) a ray-tracing window shows the neutrons trajectories; (upper-right) 1D plots of the neutron distribution as a function of the position on the detector, the divergence, the wavelength or the time are available, (down-right) 2D plots can display correlations between the previous parameters.*

of the Clessidra lenses, parasitic reflections at the base of the prisms are observed.

The *SimulSpectro* package is freely available on the Web [175].

I have used it to simulate and evaluate the performances of the different concepts of high flux reflectometers which are presented in the following.
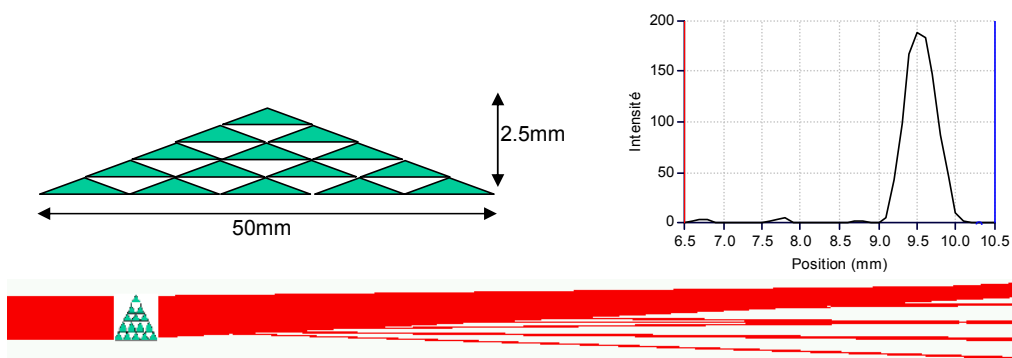
Figure 12.3.: *(left) Clessidra lens; (right) Monte-Carlo simulation for $\lambda = 0.4$ nm, focal point at 1800 mm. The size of the focal point is 0.5 mm (height of a prism).*

12.2. High flux specular reflectometers

The objective is to increase the available flux for specular neutron reflectivity measurements. Significant gains in flux could be used for: (i) very fast measurements on usual systems, (ii) kinetic studies, (iii) systematic studies versus external parameters (temperature - pressure - magnetic field - partial vapor pressure), or (iv) measurements on very small samples.

In specular reflectivity measurements, the neutron phase space is drastically reduced: the beam is highly collimated and either monochromatized on fixed wavelength spectrometers or chopped on time-of-flight reflectometers. Both methods lead to an important and similar waste of flux. The reflectivity geometry is however very specific compared to other scattering experiments since the beam is scattered only in a very small volume of the space. This gives an extra degree of freedom which can be used to redesign neutron reflectometers so as to maximize the use of the neutron flux.

There are several ways of using this space so as to improve the use of the neutron flux available at the guides output.

- The first technique consists in using a $spin-space$ encoding. Instead of collimating the neutron beam incident on the sample, the incidence angle is coded by Larmor precession. In principle, a very broad incidence divergence can thus be used leading to significant flux improvements. This technique is often referred to as $SERGIS$ [176]. The principle is very appealing but the implementation is rather complex since it requires the use of spin-echo techniques. It is still under development.

- A second technique consists in performing a $time-space$ encoding. In a traditional ToF experiment, only a single pulse of neutron is used at a time since it is necessary to wait for the whole pulse to have been detected before the next one arrives. I have devised a method in which it is possible to have a large number of neutron pulses coexisting at the same time [178]. I have named this technique $TILTOF$ since it is a tilt modulation of the sample which is used to create the parallel pulses. In this technique it is possible to get rid of the chopper and thus a significant flux increase is achieved.

- The third class of techniques consists in performing an $energy-space$ encoding. The first variant is very simple since it consists in analyzing the neutron wavelength with an energy dispersive device after reflection on the sample. I am proposing two devices: $GRADTOF$ [179] based on quadrupolar magnets and $EASYREF$ [184] based on reflective optics. In a second variant, based on advanced reflective optics, the neutron energy is correlated with the incidence angle. I have named this technique $REFOCUS$. It is based on advanced reflective optics. In both variants, no chopper is required and thus very large gains in flux are achieved.

In the following I will briefly describe the different techniques which I have developed and conclude with a discussion on the merits and shortcomings of the different methods.

12.2.1. Time-Space encoding: TILTOF

On a classical ToF reflectometer, the beam is shaped into short pulses which are reflected on the sample, the neutron wavelengths are determined by measuring the neutron arrival

time on the detector. The typical wavelength bandwidth on a continuous neutron source ranges between 0.25 to 2.5 nm. A key constraint is that it is necessary to let the whole pulse arrive on the detector before sending a new one in order to avoid frame overlap, that is mixing slow speed, long wavelengths neutrons from pulse n and fast speed, short wavelength neutrons from pulse $n + 1$. In practice this limits the repetition rate of the pulses to about 30 Hz. The actual fraction of the neutron beam which is sent on the sample is as low as a few percents.

In the TilTOF technique, I propose to remove the chopper and to use a fast periodic tilt modulation of the sample to create the time shaping of the beam (Figure 12.4). The principle consists in spreading neutron time slices in different spatial directions. At time t_0, the incidence angle on the sample will be θ_0. The sample reflects a first fraction of the beam on the detector in the direction $2\theta_0$. At the time $t_0 + \Delta t$, with Δt being the typical length of a time frame, the incidence angle on the sample is increased to $\theta_0 + \Delta\theta$. The sample reflects the next fraction of the beam on the detector in the direction $2(\theta_0 + \Delta\theta)$. The principle thus consists in sending in parallel different neutron pulses in different spatial directions. This circumvents the problem of the frames overlap.
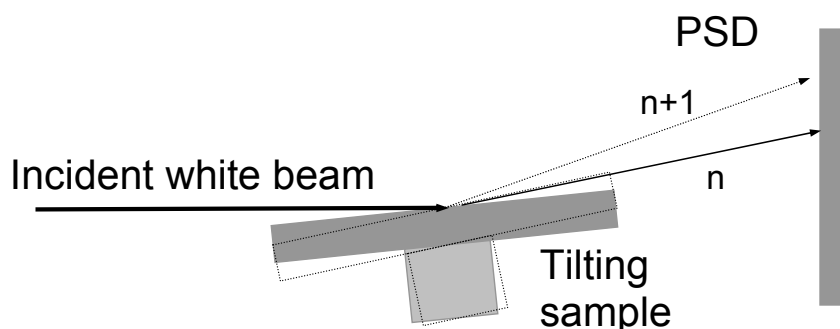
Figure 12.4.: *Reflectivity measurements in the TILTOF geometry. The sample is tilted at a regular pace between each neutron frame.*

The different neutron pulses P_i corresponding to an incidence angle θ_i are sent onto a Position Sensitive Detector (PSD). In each cell of the detector a time-of-flight analysis is performed which provides the reflectivity of the sample for an incidence angle θ_i. Figure 12.5 presents typical raw data measured on a Cu(30nm)//glass sample. Each horizontal line corresponds to a ToF measurement of the reflected pulse P_i for a given incidence angle θ_i. At the top of the picture, the incidence angles are small and thus the average reflectivity is high, giving rise to a high intensity; at the bottom of the picture, the incidence angles are large, the reflectivity and intensity are lower. The vertical "waves" correspond to the Kiessig fringes in the reflectivity of the Cu layer. The data processing is rather complex but is implemented in the program $SpectraProcessor$ [177]. The following steps must be performed :

- Calibration of the sample angle as a function of the position on the detector.
- Fine time calibration of the tilting trajectory.
- For each of the spatial position on the detector, definition of the initial ToF pulse (represented as a continuous line on figure 12.5).

Then for each pixel in the detector, a reflectivity curve is deduced. These curves are eventually summed up. A more detailed description of the test of the device on the

reflectometer EROS can be found in [178]. The practical implementation of the device is however non trivial. Unforeseen complications such as the Doppler effect during reflection are still under investigation.

It should also be mentioned that in this device, parasitic diffuse scattering or incoherent scattering from the sample is integrated on the detector. This reduces the performances of the set-up in the minimum reflectivity that can be measured. Nevertheless, in the case of the diffuse scattering from a "typical" sample, Monte-Carlo simulations have shown that it should be possible to obtain reasonably good data down to $R \sim 10^{-6}$.

The whole set-up has been modeled using the *SimulSpectro* package. Improvements such as the implementation of off-specular noise suppression slits have been modeled (though not implemented yet).
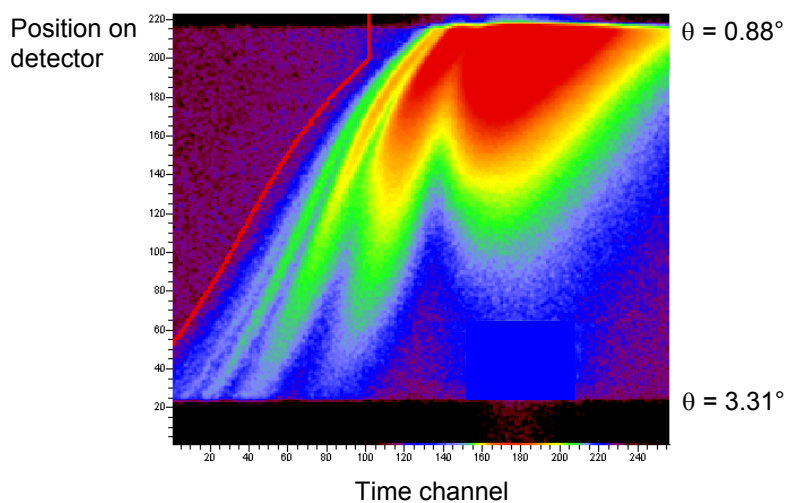
Figure 12.5.: *Raw TilToF data. Only the data of the increasing incidence angle part of the tilt trajectory are presented. The incidence angles on the sample are increasing from the top to the bottom from a value of θ_i = 0.88° at pixel Y = 215 to θ_i = 3.31° at pixel Y = 25.*

12.2.2. Energy-Space encoding: energy analysis after the sample

This class of concepts uses *energy-space* encoding. The principle is very simple since it consists in analyzing the neutron wavelengths after reflection on the sample with an energy dispersive device (Fig. 12.6a).

12.2.2.1. Refractive devices

The energy analysis device can consist either of a refractive crystal (Fig. 12.6b) [180] or of a magnetic field gradient (Fig. 12.6a) [179]. The different wavelengths λ entering the dispersive device are deviated by an angle $\alpha(\lambda)$. After a traveling path of a few meters, the different wavelengths arrive at different positions on a Position Sensitive Detector (PSD). The reflectivity of the sample is thus measured at once on the detector : $R(\lambda) \sim I(x)$. All incoming neutrons can be used without monochromatization or chopping. A gain in flux of more than one order of magnitude can be achieved.
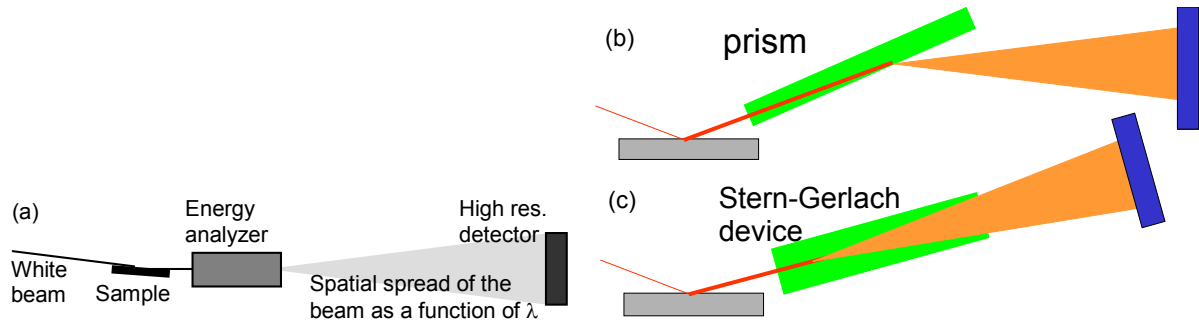
Figure 12.6.: *(a) Principle of specular reflectivity measurements using an energy analysis device. A white beam is sent onto a sample. After reflection, the different wavelengths are spatially spread in an energy analyzer. The reflectivity signal is measured at once for all wavelengths on a position sensitive detector. (b-c) The energy analysis can be performed using refractive optics (either in a prism crystal or in a magnetic field gradient)*

The figure 12.7 shows a Monte-Carlo simulation of a set-up using a field gradient energy analysis [179]. The plot represents the arrival positions of the different wavelengths on the detector. The main feature of the plot is the section of arc which corresponds to the specular reflection on the sample. The whole wavelength range is spread over more than 200 mm on the detector which allows an easy discrimination between the different wavelengths. The spread is non linear because of the λ^2 dependence of the deflection. This makes the device very efficient at long wavelengths and far less efficient at short wavelengths (below $0.5nm$).
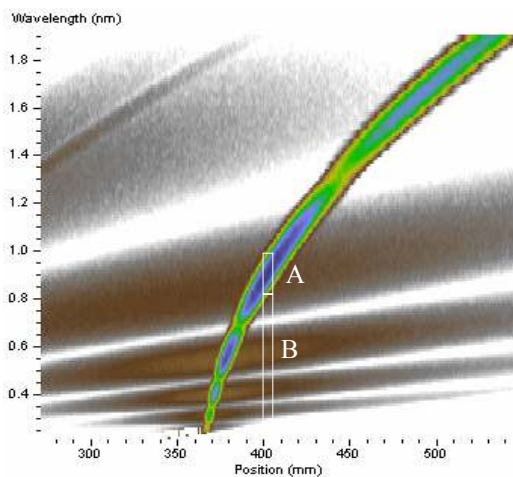
Figure 12.7.: *Wavelengths versus position on the detector. In the experiment, only the projection of the signal on the position axis is measured.*

The off-specular diffuse scattering of the sample can in principle be eliminated by collimating the beam at the entrance of the energy analysis device. Nevertheless, since the collimation would have a finite angular acceptance, the issue of off-specular scattering from the sample has been also been quantitatively assessed in Monte-Carlo simulations 12.7[179]. If one considers for example a wavelength of 9Å, its arrival position on the

detector will be around $X = 400mm$. The specular signal is the integral signal in box A. On the detector, one will also measure the diffuse signal in box B. The simulations show that for a "not too rough" sample, the off-specular scattering (in box B) only amounts to 10^{-3} of the specular reflectivity signal (in box A). Diffuse off-specular scattering is thus not an issue.

Surprisingly, the refraction efficiency of solid prisms and magnetic fields is almost equivalent. With a prism, diffuse scattering and flatness of the prism are an issue. With Stern-Gerlach devices, the field gradient amplitude and volume is limited. These solutions look simple in principle but refraction effects are very small for neutrons. These solutions are satisfactory only for rather long wavelengths ($\lambda > 0.5$ nm) and small samples and thus only a limited Q range can be probed. This is why I propose to use hybrid setups combining energy analysis and a very fast chopper system. This is discussed in section 13.2.4.

12.2.2.2. EASYRef

The first proposed solution for $energy - space$ encoding has limitations since it is intrinsically limited by the maximum field gradients which can be technically achieved. I am thus proposing an optical device which performs the equivalent of an energy analysis on a white neutron beam. A very similar idea was already proposed by C.F. Majkrzak some time ago [181]. The design is based on reflective optics. It combines multi-layer monochromator mirrors and a Position Sensitive Detector (PSD) (Fig. 12.8). Ideally, each monochromator (index i) reflects a wavelength band $\{\lambda_i - \delta\lambda/2; \lambda_i + \delta\lambda/2\}$. The diffracted beams are spatially spread on the PSD and the wavelength is directly determined by the position on the detector. The reflectivity is thus measured at once for all wavelengths.
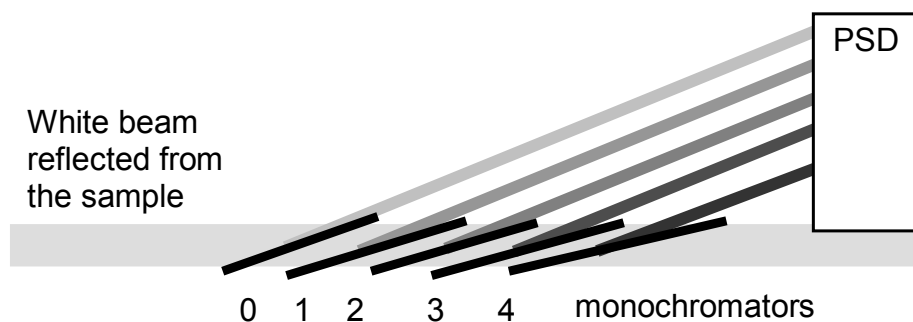
Figure 12.8.: *The reflected beam is sent on stacked monochromators. The incidence angle on each monochromator varies so that each monochromator diffracts a different wavelength band. The wavelength is directly determined by the position on the detector.*

Monte-Carlo simulations were performed on this design using SimulSpectro [175]. The monochromators were taken with a realistic reflectivity and a bandwidth of about 7% (Fig. 12.9a). The detector was set at 1500 mm after the device. Figure 12.9b represents the neutron position on the detector (X-axis) as a function of the wavelength (Y-axis). The signal of interest is along the region A. A wavelength can be associated to each position of

the detector. Figure 12.9c shows the raw reflectivity signal as measured for a Ni(10nm)//Si film illuminated with the spectrum of the guide G3bis at the LLB at an incidence angle of 4°. The finite size (2 mm) and divergence (0.06°) of the incident beam are taken into account as well as the full reflectivity of the monochromator mirrors, including the total reflection region. In order to retrieve the actual reflectivity of the sample, it is necessary to divide the raw spectrum by the white incident spectrum. Experimentally, this signal is measured by sending the white beam through the device. After that, a wavelength must be attributed to each peak, which in practice can be calibrated by ToF.
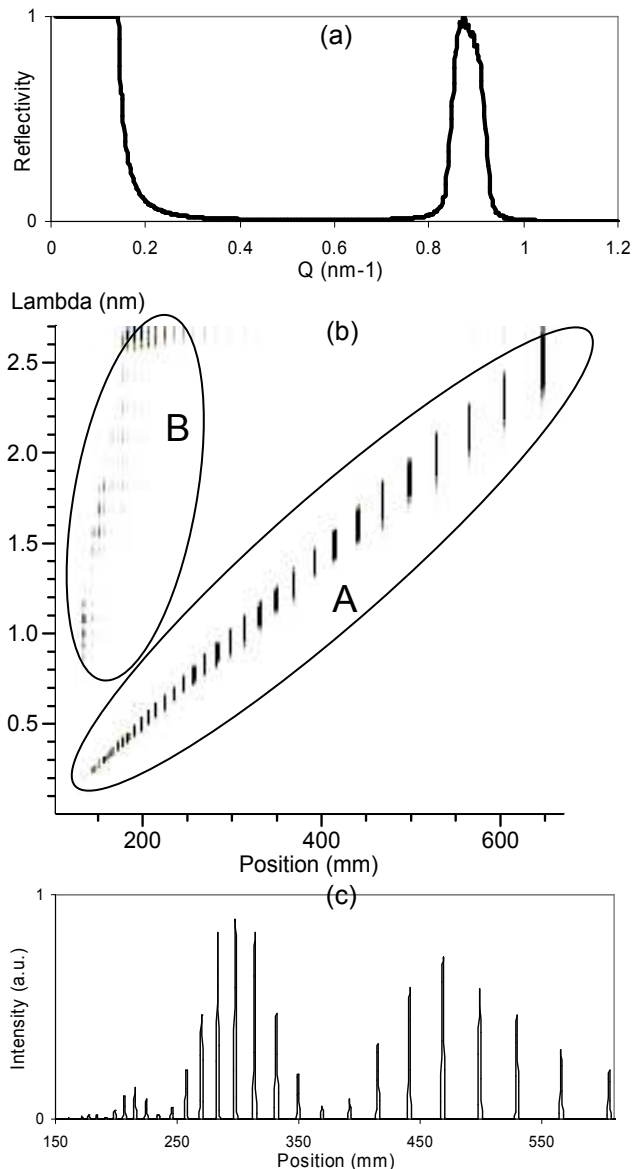
Figure 12.9.: *(a) Reflectivity of the monochromator used for the simulations. (b) λ versus position on the detector. (c) Raw reflectivity signal as measured on the detector (projection of the 2D signal of figure (b) onto the position axis.)*

Figure 12.10 compares the measured reflectivity in a classical ToF measurement, a raw integration of the Figure 12.9c data, an integration after having filtered the parasitic

neutrons from the region **B** on Figure 12.9b which spoil the signal of the short wavelength neutrons. These parasitic neutrons come from the fact that (i) the monochromators are not perfectly reflecting, (ii) that the overlap between the monochromators bands is not perfect, (iii) that there are some total reflections below the Si critical edge. In practice, the filtering of these long wavelengths neutrons can be performed with a simple nickel mirror deposited on silicon. Without long wavelength filtering, the signal is spoiled above $Q = 3nm^{-1}$. And the lowest measurable reflectivity is a few 10^{-6}. If long wavelength neutrons are filtered out, signals down to a few 10^{-7} could be measured. Surprisingly, the oscillations in the EASYREF setup are more pronounced than in the classical ToF measurement. This is due to the fact that in the case of the EASYREF setup, the 7% resolution distribution function is almost square. In the case of the ToF measurement, the resolution was taken as a Gaussian.

A detailed technical description of the device can be found in [182].

A similar concept in being proposed at NIST [183].
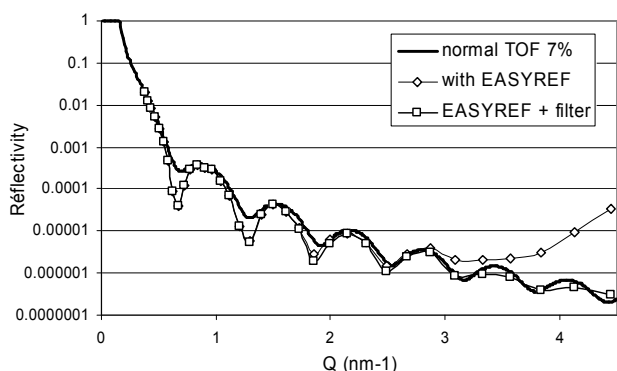
Figure 12.10.: *Reflectivity on a Ni(10nm)//Si sample. (solid line) Classical ToF measurement, (diamond) after integration of the signal of Figure 12.9c, (square) after having filtered out the parasitic long wavelength neutrons. General principle of the ReFOCUS design; (short to long dashes) short to long wavelengths.*

12.2.3. REFOCUS

The last concept is using a correlation between the neutron energy and the incidence angle. The principle of the ReFOCUS technique is presented on Fig . 12.11a. Let's consider a divergent neutron point source, typically a slit at the exit of a guide. The sample can be considered as a point source. We propose to implement a graded multilayer monochromator with an elliptical shape. The elliptical profile ensures that the optical device has two foci so that the source is imaged on the sample. All neutrons exiting the point source are reflected at the sample position. In order to correlate the position and the wavelength, the elliptical mirror is coated with a multilayer monochromator whose periodicity varies along the elliptical mirror.

The elliptical focusing device may be used in different configurations to perform reflectivity measurements (Fig. 12.11b and c). The First mode can be seen as derived from the monochromatic operation mode. The system is set-up so that for each sample position
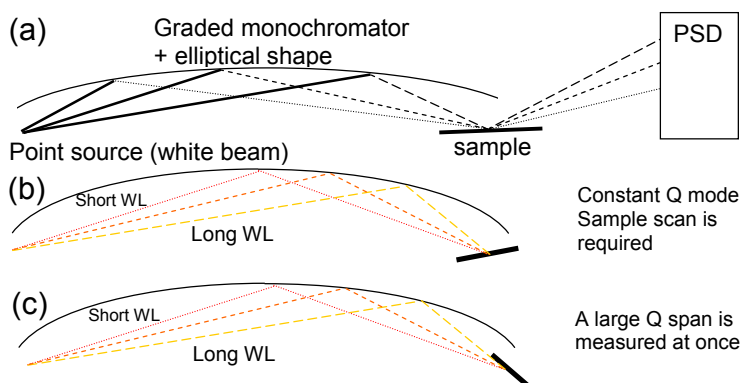
Figure 12.11.: *(a) General principle of the REFOCUS design; (short to long dashes) short to long wavelengths. (b-c) The different operation modes to perform reflectivity measurements.*

one operates at a fixed scattering wave-vector. Short wavelengths are incident on the sample with a small angle, long wavelengths are incident with a large angle so that the scattering wave-vector $Q = 4\pi\theta/\lambda$ is kept constant. In order to scan the reciprocal space, the sample angle is varied. In this mode, it is thus possible to use the full white beam while keeping a good resolution in Q space $\delta Q = 4\pi\delta\theta/\lambda$. The δQ and $\delta\theta$ parameters are defined by the focusing device construction. In this configuration, the REFOCUS setup can be compared to a monochromatic spectrometer. But in practice, a typical monochromatic spectrometer operates at 4Å with a wavelength resolution of 2%, which corresponds to a bandwidth of 0.08Å. With the REFOCUS geometry, it is possible to use the full white beam which corresponds to a gain in flux of 50 to 80 (depending on the guide system). This mode is very efficient in terms of used neutrons. It is also very simple to operate since the integrated flux on the PSD directly corresponds to the reflectivity. However, it requires scanning the sample angle.

In the second mode, short wavelengths are incident with a large angle, long wavelengths are incident with a small angle. In this configuration, since long wavelengths are incident with a smaller angle, the reflectivity of the sample is higher and the wavelengths are more efficiently reflected. This mode is close to the ToF mode where the shape of the reflectivity curve inversely matches the shape of the incident spectrum. In this geometry, the total reflectivity of the sample can be measured at once without moving the sample.

Monte-Carlo modeling has been performed for the TOF mode. We optimized the ellipse grading using a quadratic dependence for $\lambda(X)$. The wavelength varies between 0.35 and 2.5nm along the ellipse. The sample angle was set at 6°. Figure 12.12a shows the distribution of the intensity after reflection on a Ni(10nm)//Si sample. The calculation has been performed by considering a perfectly reflecting sample. For a given position on the detector the wavelength resolution is of the order of 5-10%. After integration of the signal on the detector, (Fig. 12.12b; squares), one can observed that it is possible to resolve the Kiessig fringes up to the 4th order which corresponds to reflectivities of 10^{-6}. The flat region above 280mm correspond to the total reflection region. The intensity on the detector is rather smoothly spread (only 2 orders of magnitude of variations). This is very important to ensure that the data on one part of the detector are not polluted by some very intense scattering on another part of the detector.
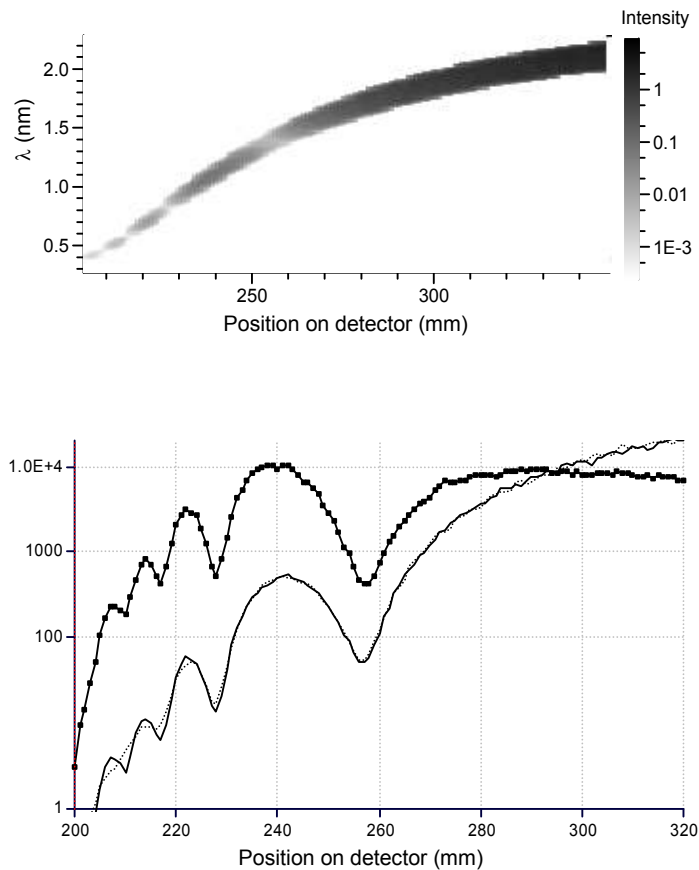
Figure 12.12.: *Reflectivity on a Ni(10nm)//Si sample. (a) Reflected intensity versus wavelength and the position on the PSD. (b) Total intensity as measured on the detector: (lines) Signal with a flat input spectrum (with an input slit of 2mm (solid line) and 4mm (dotted line)); (squares) signal with a real input spectrum (G3bis) and an input slit of 2mm.*

The proposed design combines several advantages. It does not require any complex mechanics. It is simple and cheap. It can be implemented rather easily on existing spectrometers. It is a general purpose set-up which can be used in any experimental situation: small samples, very large samples or small magnetic samples, contrary to other solutions. It may even be used for liquid samples in Mode 2, if the whole focusing ellipse can be tilted. We have presented a design which is using a 3m elliptical focusing optics coated with $3\theta_c$ monochromators. This choice was made to demonstrate that existing technology is advanced enough to implement the concept right now and that it can be readily tested on existing spectrometers provided there is about 10-12 m of free space after a guide end. However, it is easily possible to improve the design by considering larger focusing optics. By doubling the size of the device, the solid angle will also be doubled and thus the flux multiplied by a factor 2. By using $4\theta_c$ or $5\theta_c$ monochromators, the solid angle can also be increased for short wavelengths. An extra flux gain would again be obtained. Other designs can be derived from the REFOCUS principle. Instead of using a graded monochromator coating on the ellipse, it is possible to associate a focusing ellipse coated with super-mirrors and couple this device with a chopper in order to perform ToF

measurements with continuously varying incidence angles. In theory the performances should be close to the REFOCUS design.

A detailed technical description of the device can be found in [184].

A similar concept in being proposed at NIST [185].

12.3. Hybrid solutions: GRADTOF

In the different solutions proposed above, the most challenging problem is to handle short wavelengths neutrons ($\lambda < 0.4\,nm$). In the case of the energy analysis using refraction, the deflection angles are so small that only a coarse Q resolution can be achieved. In the case of the EASYREF device, it is difficult to produce very efficient, high m multilayer monochromators so as to keep the device compact. In the case of the REFOCUS setup, the design is also constrained by the m index of the graded mirror.

To overcome these difficulties, I propose to combine the above setups with a high speed chopper in order to perform classical TOF measurements for short wavelengths while using the energy analysis for long wavelengths. On a typical TOF reflectometer, the wavelength band which is used extends from 0.2 to 3 nm, the frame overlap limit being set at $\lambda < 3\,nm$. By using a disk chopper set for a wavelength band ranging from 0.2 to 0.5 nm and an energy analysis device for long wavelengths, it is possible to increase the repetition rate up to $200\,Hz$ without frame overlap issues. Since the repetition rate of the TOF pulses can be increased from 30Hz (typical set-up) to 200Hz, there is an immediate gain in flux of a factor 7 that can readily be achieved on any existing TOF reflectometer provided the chopper can rotate fast enough. In such a set-up, there is no compromise in resolution since the regular TOF operation is used for short wavelengths and since for long wavelengths (above 0.5nm) the performances of the proposed energy analysis devices are good.

12.4. Merit of the different technical solutions

In the field of neutron instrumentation, one should always keep in mind that eventually a non expert user should be able to handle the spectrometer. Presently it is not clear which technical solution will provide both performances and flexibility such that a "casual" user can take benefit of it. The different solutions which have been proposed above have the advantage that they can in principle be implemented on any existing ToF reflectometer operating on a continuous neutron source. They however strongly differ in their implementations.

TILTOF: The required equipment is very limited and costless (only a few k€ are required for the mechanical tilt system). Most of the investment has to go into software and expertise. This solution is however rather difficult to hand over to a non expert user since it requires complex calibration and data processing (which is at the moment very far from transparent for the user). Moreover, since the sample is moving, it prevents the use of a wide range of standard ancillary equipments (no cryostat, no furnace, no humidity cell, no solid-liquid interfaces, no Langmuir cell, no free liquid surfaces). This means that it is restricted to very standard measurements at room

temperature. The gain in flux cannot thus be used to perform new, more complex experiments. In my opinion this solution is not general purpose and does not suit the needs of users.

REFRACTION: This solution is appealing since it only requires the insertion of the device after the sample on any existing spectrometer. The data acquisition is almost unchanged and the data processing is hardly more complex than usual. The solution is very flexible since the device can very easily be switched in or out. However there are technical limitations in the refractive effects that can be achieved over a reasonable cross section. This makes the device only suitable for small samples (of the order of 1cm\texttwosuperior{}) or small incidence angles, which limits the accessible Q range. This however corresponds to the typical magnetic thin films substrate sizes. In the case of the magnetic refraction, no material is introduced in the beam and an extra advantage is that the device performs a perfect spin analysis.

EASYREF: This solution is very appealing by its simplicity of use. The data processing should be straightforward since the user will simply have to switch the beam on and off and will immediately get the reflectivity curve. It has however not been tested in practice. Several technical issues may appear but the rapid progress of neutron reflective optics are such that I can hardly imagine anything which could prevent the device to eventually be implemented. One of the drawback is that some material is put in the beam after the sample which generates some absorption. However I am confident that usable devices will be fabricated and implemented in the short term.

REFOCUS: This solution departs rather radically from the usual way of operating a neutron reflectometer. It has the highest potential to increase the flux on neutron reflectometers by up to 2 orders of magnitude. However, extensive developments in neutron optics are still required. I think that this solution might be implemented in the medium term since it will require to gather a significant amount of expertise and technical developments.

GRADTOF: The hybrid solution combining energy analysis for long wavelengths and very high repetition rate TOF is interesting since a significant gain in flux is obtained while keeping good performances in resolution at short wavelengths.

SERGIS: Solutions based on spin encoding are by far the most innovative. They offer the biggest potential of improvement in neutron instrumentation. However, they are also the most complex to set-up. Presently a number of groups around the world are evaluating the technique and gathering expertise in the operation of spin-echo based reflectometers. I am convinced that these efforts will eventually provide significant results. The technique will however always have strong limitations in the field of magnetic scattering which represents a significant domain of applications in reflectometry. This technique also requires to develop a specific spectrometer.

In the future, I will personally focus my work on the *EASYREF* and *REFOCUS* techniques and demonstrate their usability. The cost of these solutions is rather limited and generally represent only a tiny fraction of the cost of a whole spectrometer.

The gains in flux that will be achieved will be used to perform either :
- ultra-fast reflectivity measurements (within seconds) or kinetic experiments
- in-situ measurements versus external parameters such as the temperature, the humidity, the UV illumination...

However, even though the total flux will be increased, we do not think that these solutions will make it possible to achieve measurements at very low reflectivities ($R < 10^{-6}$) so that the measurable Q range will not be extended compared to existing instruments.

These limitations arise from several issues which need to be quantitatively assessed. The first one which is obvious is the issue of the diffuse scattering from the sample. In most of the Monte-Carlo simulations it has been taken into account and has been shown to be negligible. In practice, the diffuse scattering from the optics is more likely to be an issue.

The second point is that in the study of soft matter systems, the incoherent scattering might be an issue since it is proportional to the incident flux. In the case of the energy analysis systems set after the sample, they behave as collimators so that the level of incoherent scattering should not be different compared to a regular setup. However, in the case of the REFOCUS setup, incoherent scattering is an issue since after the sample the solid angle is wide open so that the incoherent scattering is integrated on the PSD.

We have shown that significant gains in flux are possible on neutron reflectometers for specular reflectivity measurements ($\times 5$ with low risks and up to $\times 50$ if advanced optical techniques are used). One of the key advantage of the proposed set-ups is that they can be tested and implemented on almost any TOF reflectometer so that the transition from one technique to the other can be made with a very low risk. In the case where off-specular would need to be measured, it would always be possible to operate in the regular TOF mode. The proposed spectrometers would use a large fraction of the neutron flux available in the guides and since the integrated neutron flux is still 10 to 100 times higher on nuclear reactors compared to spallation sources (long pulse or short pulse), they would provide performances which are equivalent or even better than the reflectometers that are being implemented on the new spallation sources (such as JPARC or SNS).

Method	TilTOF	REFRACTION	EASYREF	REFOCUS	GRADTOF	SERGIS
Complexity	Medium	Simple	Simple	Medium	Medium	High
Data acquisition	Difficult	Simple	Simple	Medium	Medium	High
Data processing	Difficult	Simple	Simple	Simple	Simple	Difficult
Efficiency	x10	x10	x20	x50	x50	x100
Flexibility	Low	Medium	High	High	High	Low
Cost	€5000	€20000	€20000	€100000	€50000	€300000

Table 12.1.: *Merit of the different solutions.*

12. Instrumentation developments

13. Software developments

In parallel with instrumentation developments it is necessary to propose advanced data acquisition tools, data processing tools and modeling tools. I have developed different software packages, *SpectroDriver, SpectraProcessor, SimulReflec* which are aimed at these respective tasks. These programs share a common user interface for basic tasks (1D, 2D, 3D, 4D plotting, Input/Outputs, scripting capabilities..). The different packages simply depart by the fact that they each provide some specialized modules for some specific tasks (data acquisition, data processing and fitting, reflectivity fitting).

I will quickly browse through the functionalities of these different programs.

13.1. SpectroDriver

This piece of software was the original starting point of the different projects and is developed together with Claude Fermon (IRAMIS/SPEC).

The software offers the possibility to control a very wide panel of devices. It has been designed in a modular way so that it is being used to drive neutron reflectometers, a SANS spectrometer, an X-ray reflectometer, two Kerr effect set-ups, an NMR spectrometer, different resistivity benches, a detector test bench.

In the case of neutron scattering, it can be interfaced with any type of detector and allows to perform acquisition on a PSD detector in time of flight mode (4D mode). It provides advanced scripting facilities which enable very complex acquisition sequences to be performed.

13.2. SpectraProcessor

This program provides 1D, 2D, 3D data processing and visualization. It is mostly used to process 2D data sets (usually measured on SANS spectrometers). It provides advanced grouping and masking functionalities. It provides a 2D fitting module which may be used for magnetic SANS or GISANS data fitting. The *SpectraProcessor* package is freely available on the Web [177].

13.3. SimulReflec

This program is an essential piece of software to model reflectivity data. It was originally intended to process polarized neutron reflectivity data but has been upgraded with various additional modules. Its features are:
- Fitting of X-ray reflectivity data
- Fitting of magnetic reflectivity in the most general situations (including Zeeman effects and non collinear configurations)

13. Software developments
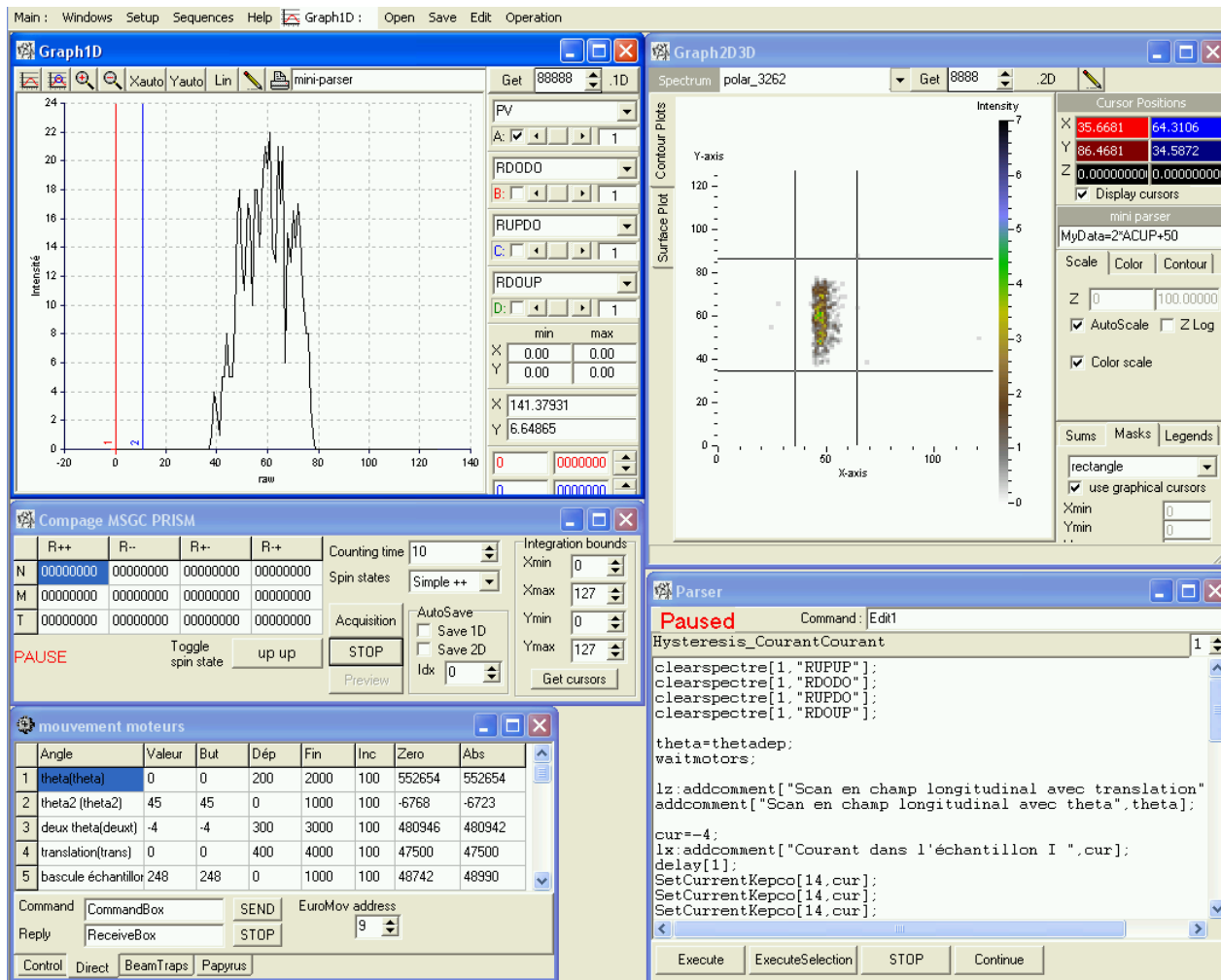
Figure 13.1.: SpectroDriver *interface, a wide range of graphical windows are available.
(upper-left) 1D plot of the acquisition scans; (bottom-left) Control of the
motors of the spectrometer; (top-right) 2D plot measured on a PSD; (bottom
right) scripting window.*

- Calculation of magnetic off-specular data (via the SDMS module of magnetic off-specular scattering written by E. Kentzinger based on the formalism developed by B. Toperverg.)

The program provides a user friendly interface so as to be very easy to use for casual experimentalists.

The *SimulReflec* package is freely available on the Web [186].
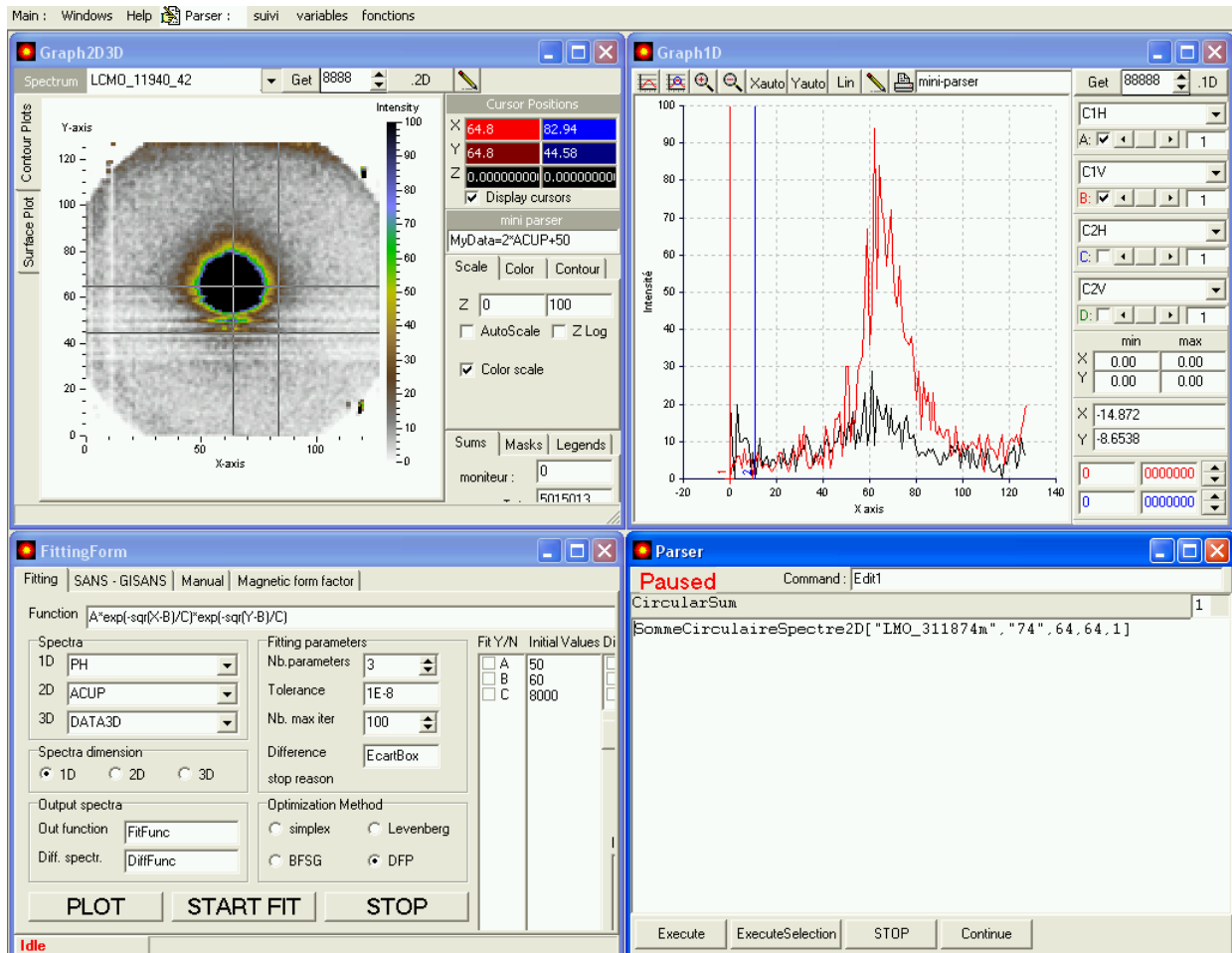
Figure 13.2.: SpectraProcessor *interface. (upper-left) 1D plot of the acquisition scans; (bottom-left) Fitting/simulation windows; (top-right) 2D plot measured on a PSD; (bottom right) scripting window.*
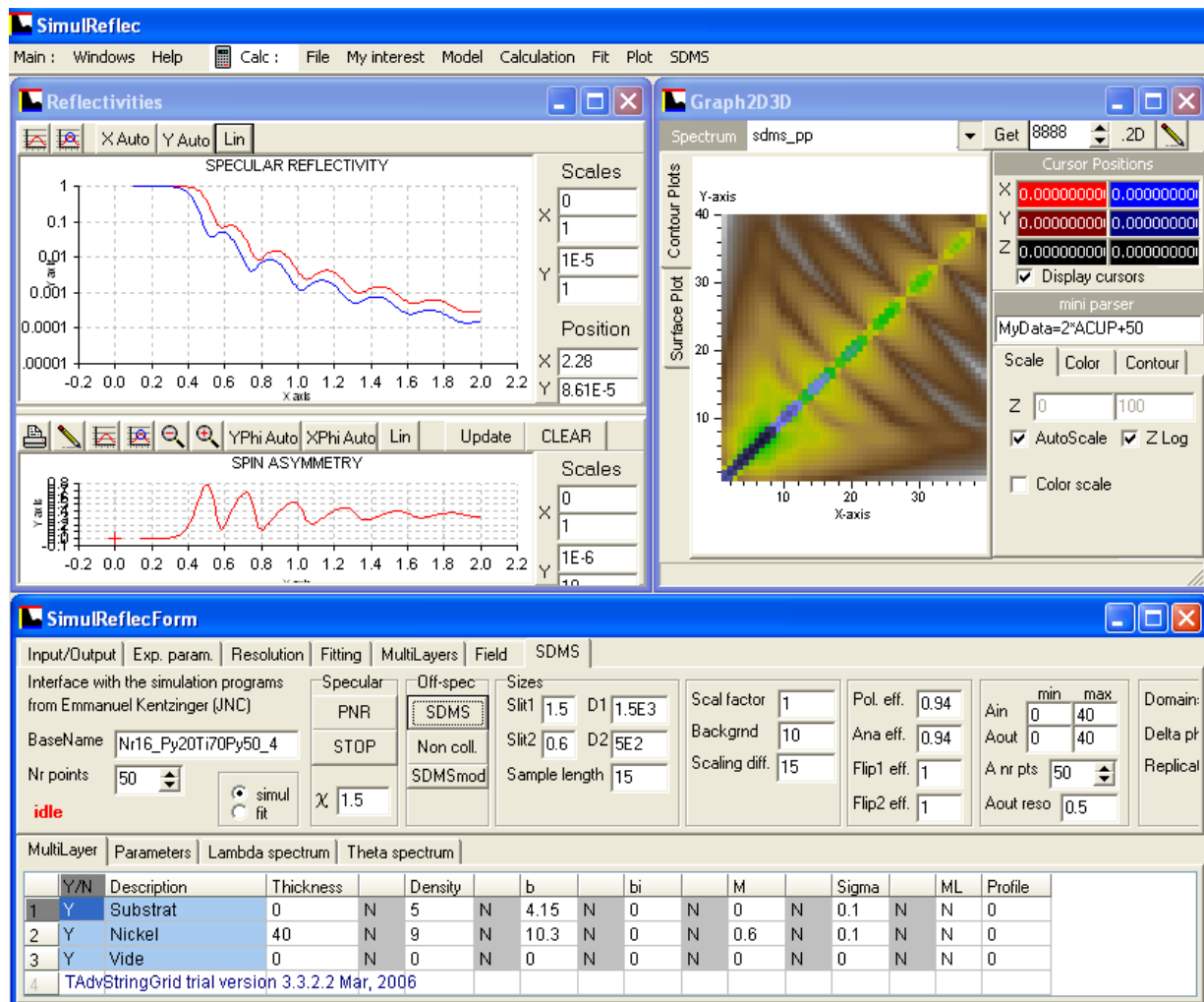
Figure 13.3.: SimulReflec *interface.* *(upper-left) Reflectivity calculation and spin-asymmetry. (bottom) Description of the multilayer system. (upper-right) 2D off-specular scattering.*

14. Perspectives

14.1. Use of neutron scattering to study magnetic nanostructures for the next decade

The neutron scattering techniques have been used for about 15 years for the study of magnetic nanostructures. In the early studies of magnetic superlattices, new types of magnetic orders were directly and unambiguously probed. Since then they have been systematically been used for the study of magnetic thin films heterostructures. They are even used to characterize industrial systems.

14.1.1. Spin electronics

Presently, one of the most active field of research in magnetism is "spin electronics". The hottest topics in the last couple of years have been spin injection via tunnel barriers and spin torque excitations. In the case of spin injection, the relevant length scale is the atomic layer which governs the behavior of the electrical transport in tunnel junctions (Fe/MgO/Fe is the industrially most promising structure). Presently no technique besides electrical measurements is sensitive enough to characterize the interfaces down to the atomic plane. It is necessary to measure the orbital configuration of a single atomic layer. In the case of spin torque excitations, the relevant energy excitations are of the order of a few GHz and the total emitted power of the order of 1 nW. These energy scales are well beyond any neutron spectroscopic measurements.

It is thus difficult to figure out how neutron scattering could contribute significantly to these fields.

14.1.2. Magnetization "imaging"

In a number of magnetism studies, the ultimate objective is to determine a 3D magnetization distribution. Neutron scattering can significantly contribute to the field of imaging of magnetic structures (in the broadest sense). Neutron imaging can be performed either in the direct space or in the reciprocal space.

At the atomic scale, this is routinely performed using neutron single crystal diffraction with the highest possible degree of refinement since it is possible to determine atomic resolved spin density maps.

At millimetric scales, direct space methods can be used. It has recently been demonstrated that neutron imaging combined with spin precession could be used to image magnetic stray fields [190].

At micrometric scales, it is difficult to say whether direct space or reciprocal space techniques are more efficient. Direct space imaging techniques certainly have the potential to reach sub-millimeter resolutions. This requires nevertheless significant instrumental

developments. At micrometric scales, off-specular scattering can be used. One must however bare in mind that this is justified only in the case of buried structures since simple optical techniques can easily reach sub-µm resolutions.

At nanometric scales, I have illustrated in the previous chapters how neutron scattering has the potential to measure complex magnetic configurations. We must however mention that instrumental developments are very rapid in the field of electronic magnetic imaging which now achieves resolutions of a few nm. X-ray imaging of magnetic structures achieves resolution of a few tens of nanometers and also allows to image anti-ferromagnetic structures. The two previous techniques operate in the direct space so that individual objects can be probed. In the case of neutrons, the constraint is that the studied systems need to be extended (thin films, crystals or powders) so that enough neutron flux can be captured. It will never be possible to study individual nano-objects.

This strong competition means that neutron scattering studies should be focused on the study of "bulk" materials. On the other hand, other techniques such as electronic and x-ray imaging will always remain surface techniques.

14.1.3. Magnetic nano-materials

The field in which neutron scattering is the most likely to make significant contributions in the future is the study of "functional" materials.

A number of "complex" magnetic materials have intrinsic interesting properties. During the last decade, a wealth of research has been performed on manganite materials whose physics is often defined by nanometric scale properties (magnetic phase separation, extrinsic colossal magneto-resistance). More recently, one of the hot topic has been the study of magneto-electric compounds which are usually magnetic oxide and which exhibit coupled ferromagnetic and ferroelectric properties. The long range helical order in magneto-electric compounds (such as $MnSi$, $BiFeO_3$) plays a key role in the properties of these materials. In this field, magnetic SANS scattering can bring a significant input.

The wealth of magnetic nano-objects which are being developed (spherical particles, nanorods, nanowires, cubes, spheres, tubes) will eventually find applications only when they are associated with other materials. In the field of polymer reinforcement, the particles are mixed with polymers and it is the mixture at the nanometric scale which plays a key role. In the case of hyperthermia, the magnetic particles must be coated with bio-compatible materials so as to be efficiently transported inside the human body. In Hyper-Frequency devices using arrays of nanowires, the magnetic coupling between objects will play a key role in the resonance properties. In all these fields, polarized SANS can be an invaluable tool.

14.2. Neutron instrumentation for surfaces and nanostructures studies

As a whole, neutron scattering techniques are making steady progress. The instruments efficiency has been increasing by about one order of magnitude per decade during the last 30 years. This may however look as a slow pace compared to other techniques such as X-rays scattering. Nevertheless technical progress are such that this rhythm is likely to

be sustained at least for another two decades. We are presently designing the instruments for the next decade and dreaming about the instruments for 2020.

I will discuss in more details the present status and the evolution in instrumentation as I see it for the next decade. I shall also discuss more remote possibilities.

14.2.1. Present status and medium term evolution

Neutron scattering on thin films suffers from the weak interaction of neutrons with matter but *specular neutron reflectometry* is very competitive with other reflectivity techniques especially when polymer or magnetic materials are involved. Neutrons allow to use selective labeling via deuteration. The neutron interaction with the magnetism is very large and this compensates for the low incidence flux. Quantitative measurements are easy to perform.

Gains in flux will be achieved so as to be able to measure reflectivities down to 10^{-8} within hours. However in practice, most specular reflectivity experiments will require only to measure reflectivities down to 10^{-6}, both because of the incoherent scattering and the intrinsic roughness of most samples. This means that it will be possible to perform reflectivity measurements in a matter of minutes. Most of the effort will thus be put on providing advanced and complex sample environments, especially to perform in-situ measurements for which neutrons are perfectly suited since they are barely absorbed by any surrounding sample environment.

The case of off-specular scattering is less clear-cut. Presently the measurements of off-specular scattering are limited to very rough systems or to multilayer systems because of the low flux issue. The key problem is that even a gain of a factor 100 in flux might be insufficient to alleviate this limitation. On top of that, the technique suffers at the moment from complex data analysis and processing (especially for magnetic and Time-of-flight measurements). Because the flux is so limited, usually only a very narrow Q-range in the reciprocal space can be explored meaning that only rather long correlation lengths (above $1\mu m$) can be probed. The question arises if neutron scattering is an appropriate technique for such studies (except for very specific problems).

At the moment, it is rather clear that the popular field of "nanosciences" is interested in sizes rather well below $100nm$. In this range of sizes, one should consider GISANS techniques. Again, one faces the issue of a rather low flux which limits the studies to either rather well defined objects or multilayers. On top of that, the smaller the objects, the less efficient the GISANS technique is. Direct geometry scattering using VSANS might eventually prove be a good alternative. A direct scattering geometry provides the basic advantage that it is very easy to set-up the experiment; no alignments are required. Present developments are implementing multibeam techniques on SANS instruments: VSANS at HMI, MSANS at FRM2, TPA at the LLB which might eventually use up to 400 beams in parallel, providing an equivalent gain in flux. Similar developments have been implemented for the GISANS technique (REFSANS at FRM2) but since it is a planar geometry, the number of beams is much more limited than in a 2D geometry. The results are however very impressive.

I am very enthusiastic about the developments using Larmor precession encoding. It is yet not clear what will be the outcome but the feeling is that there is a clear potential in the techniques using either SESANS or MIEZE configurations.

14.2.2. Other surface related techniques around neutron sources

For the sake of completeness I shall mention that around neutron sources other types of secondary particles are generated which can be used for the study of thin films or magnetic structures. Muon facilities are installed around both European spallation sources (PSI and ISIS). A number of experiments have been performed on thin films [187].

At the new reactor FRM2 in München, a positron source has been installed which is about 1000 brighter than previous positron sources. The operation of the NEPOMUC spectrometer is just starting but it it likely that it will open possibilities for new types of experiments [188].

14.2.3. Long term - futuristic opportunities

Neutron reactors have reach their technical limits and further gains are limited. Neutron reactors are somewhat out of fashion and the new projects of neutrons sources are based on the spallation principle. Nevertheless, neutrons reactors could still have a role to play since the integrated flux will always be higher than on spallation sources. One needs to use the neutrons in a more efficient way. The spin-echo instruments are a very good example of an instrumentation development which allowed to use a very broad spectrum and maximize the use of the neutron beam. If neutron energy analysis could be performed in a detector, without the use of the time of flight technique, this would revolutionize all neutron scattering techniques. This possibility is not unrealistic, either using magnetic precession techniques or optical techniques.

One could mention that during the last decade, laboratory X-ray sources have made tremendous progress. Micro-focus X-ray sources have been developed which provide very high flux, coherent x-ray sources to the labs. Advanced optics such as Göbel optics have multiplied the flux on lab x-ray spectrometers by 100. This allows to perform experiments in small laboratories which until recently were restricted to big synchrotron facilities.

In my opinion it is perfectly realistic to consider that a similar evolution could happen in the field of neutron scattering. At the moment there are about 40 reflectometers available around the whole world. The new spallation source SNS will provide only 2 extra reflectometers which will be of course restricted to very selected experiments. The present situation prevents neutron reflectometry to be a routine characterization technique. However, it seems possible that in the near future it might be possible to design very compact neutron sources with a flux comparable to the present one. The present state of big facilities around big reactor is somewhat an heritage from the past since physicists installed their equipment around existing reactors which were not design from scratch to perform very well designed experiments. They were built as "big neutron" source with no overall plan with the instruments in mind.

Instead of thinking "big", the next big step might take place in thinking "small". Instead of aiming at more and more powerful sources, one could try to evaluate the use of very "compact" spallation sources. Neutron optics is now advanced enough to handle millimetric or even sub-millimetric beams. Such optics could be coupled to a very small spallation target and a small moderator very close to the target. This would be possible since the energy dissipated in such a small source would be small (a few 10kW). This would allow to benefit from very high neutron densities. It seems plausible that the neutron flux at the guides exit would be competitive. A number of problems connected to

radiological shielding and safety would be avoided. Such a small source would thus be cheap to operate. This road has the potential to change the neutron scattering technique from a niche technique to a mainstream technique.

Another possible improvement could be to build "cheap" ultra cold neutron sources ($\lambda > 500$Å). These neutrons would be very easy to handle and would open lots of new possibilities. They would be especially suited for the study of surfaces. The newest UCN source installed at the 20MW reactor FRM2 provides UCN densities which are 10 times higher than previous sources ($10^4 n/cm^3$). The Canadian Spallation Ultracold Neutron Source Project proposes to build an UCN source which would be 5 times brighter by using a very low power $20\,kW$ proton accelerator [189]. The field of very cold neutron sources is making steady progress but is still very specialized.

The number of available probes for the matter has not increased for more than a century (light, X-ray, electrons, neutron, muons are not new). Most progress have been made in their use. It is clear that laser sources, synchrotron sources and electron sources have made breakthroughs during the last decades whereas neutrons sources are still in their infancy (compared to light and x-rays). I do not see why it should not be the time for neutrons to benefit from technical breakthroughs. I think that all ingredients are gathered. Neutron could then become a routine tool for matter characterization.

14.3. My projects

My objective is to use the maximum potential out of the neutron scattering techniques for the study of magnetic nanostructures. I personally think that the possibilities of neutron scattering is presently only partially used, both for technical and methodology reasons.

My efforts will cover 3 aspects:

(i) *Methodology:* I will make an effort consisting in unifying the description and theoretical framework of the different techniques. Advanced data processing tools will be developed with the aim to make them easily available to the different users of neutron scattering instruments.

(ii) *Physics:* The possibilities of the different techniques will be demonstrated on several systems in which the physics is only partially understood.

(iii) *Instrumentation:* The performances of the spectrometers will be improved so as to turn today complex experiments into routine experiments.

14.3.1. Methods developments

The issue is to make the different techniques as transparent and technically accessible to users so that they can extract as much information as possible from the experiments they perform. The situation is rather different from one technique to the other.

Specular reflectivity is used routinely and the data processing is accessible to any casual user. The technique can nevertheless take a new step by being subject to a systematic validation of its reliability. This is an essential step if it is to be used for routine characterization applications. In this frame, I am trying to organize a Round Robin on reference samples to demonstrate the reproducibility of the results between the different neutron spectrometers available across the world.

Off-specular scattering. In the case of off-specular reflectivity and grazing incidence small angle neutron scattering, the data processing is still reserved to expert users and casual users can only extract qualitative information. The quantitative data processing is still complex and time consuming. I will try to work so as to improve the situation.

Small angle neutron scattering. Presently, the processing of magnetic SANS data is often using rather crude approximations. This situation is partly due to the lack of data processing tools to extract detailed information from the magnetic scattering in SANS measurements. The models to be used are much more complex than in non magnetic SANS. I am presently developing tools which should allow to deal with complex anisotropic magnetic objects and complex magnetic arrangements. This work will be done within the frame of the MAGAFIL ANR with the help of a post-doc student.

I will make an effort consisting in unifying the description and theoretical framework of the different techniques. This work involves making lectures so as to make the techniques known to potential users (this manuscript is part of this work) and developing modeling tools and user friendly programs, which is a field in which I already have some experience (www-llb.cea.fr/prism/programs/programs.html).

14.3.2. Physics problems

In the field of the physics, I will focus on the study of magnetic anisotropic nano-objects by neutron scattering. The first motivation is that there has been tremendous progress is the synthesis of magnetic nano-objects both in the quality of the objects (mono-dispersity), the variety of objects (wires, cubes, tubes) and the quantities (grams). The second motivation is that high performances polarized SANS spectrometers are made available (at the JCNS/FRM2, at the ILL and within a few years at the LLB) so that advanced studies will become much more easy to perform. Developing expertise in this field is thus essential.

The topics that I plan to explore are the following:

(i) *Measurement of magnetic form factors in complex objects*

It is now possible to fabricate very homogeneous magnetic nanowires using planar technologies (Fig. 14.1a). These objects could be used in spin electronic devices. In collaboration with L. Cagnon and O. Fruchart (Lab. Louis Néel/Grenoble), we would like to understand the detailed behavior of such magnetic nanowires. We would for example like to see if it is possible to finely control the reversal behavior of such systems by pinning the magnetization along the wires. The measurement of the inner magnetization of such wires is also of interest. This involves measuring the detailed form factor of such wires. The study is simplified by the fact that we deal with a very well ordered (single crystal), perfectly monodisperse system.

(ii) *Magnetic order at the nanometric scale in nanocrystals (Fig. 14.1b)*

This work should be performed in collaboration with C. Amiens (LCC Toulouse) on magnetic nanocrystals of metallic nanoparticles. We aim at probing the long range magnetic order in such structures at low temperatures. The same question arises in arrays of nanowires that we plan to study with M. Darques (Univ. Catholique Louvain). Macroscopic magnetic measurements suggest that anti-ferromagentic or frustrated orders set-in. SANS measurements should give straightforward answers about the long range magnetic correlations in such systems.

(iii) *Characterization of magnetic nanocomposite combining magnetic nanowires and*

polymers (Fig. 14.1c)

This work in collaboration with G. Viau (INSA Toulouse) and J-Y. Piquemal (ITODYS/Univ. Paris Diderot) is supported by the ANR MAGAFIL The aim is to develop composite permanent magnetic materials (using the strong shape anisotropy of the wires). The dispersion of the wires in the polymer matrix is one the key parameter which will define the qualities of the material. SANS is a very useful tool for such studies.
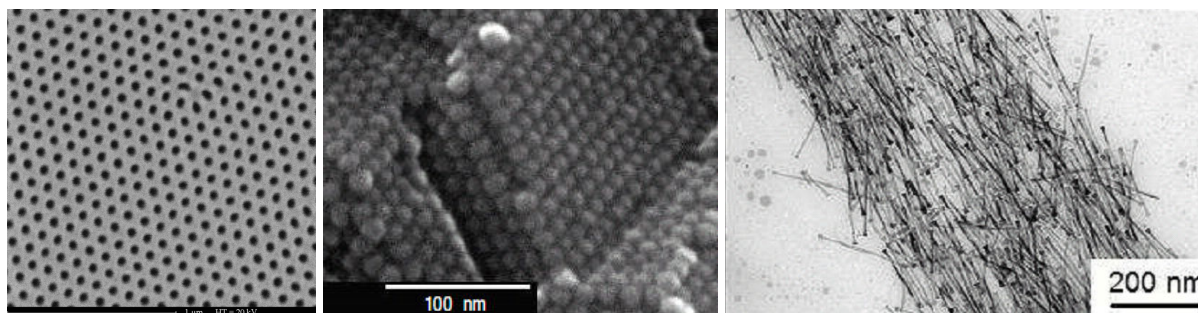

Figure 14.1.: *(a) Nanoporous alumina template with pores of 60nm in which magnetic wires are grown (courtesy of L. Cagnon). (b) Crystal of FeCo nanoparticles [25]. (c) Bundle of magnetic nanowires (courtesy of G. Viau).*

The study of the nanomagnetic structures in manganites crystals will also continue.

These different studies will require that new advanced data modeling tools are developed. This work is in progress. I hope that these new tools will make it possible to extract all the information which can be measured by SANS in complex magnetic systems and go beyond the usual approximations.

14.3.3. Instrumentation developments

The use of neutron scattering can develop only if new possibilities are offered to the users. This means that neutrons spectrometers must continuously be improved so as to be able to perform new experiments. This can happen in 2 ways:

(i) *The performances of the spectrometers are significantly improved.* This is for example the case of single crystals diffractometers which are now used to characterize epitaxial thin films. I have shown in Chapter 12 that significant gains in flux are possible on neutron reflectometers for specular reflectivity measurements ($\times 5$ with low risks and up to $\times 50$ if advanced optical techniques are used). The gains in flux that would will be achieved could be used to perform either ultra-fast reflectivity measurements (within seconds) or in-situ measurements versus external parameters such as the temperature, the humidity, the UV illumination... This would open a lot of possibilities for new experiments. In the future, I will personally focus my work on the *EASYREF* and *REFOCUS* techniques (see Chapter 12) and demonstrate their usability. The developments of these new implementations will be supported in 2009-2013 by a European Research contract "Neutrons Optics" which I am coordinating. This research network gathers most of the European neutron facilities (FRM2, HMI, ILL, JCNS, BNC). At the end of this project, a few concepts will emerge. We will take benefit of the $CAP2015$upgrade at the LLB to implement the concept which fits most of our needs on the EROS reflectometer.

(ii) *New types of instruments are developed.*

Beyond the techniques which I have presented in Chapters 2-7, it is not easy to foresee if any new technique that may emerge in the near future. At the moment, most of the developments are aimed at improving the performances of existing techniques. I personally think that inelastic scattering studies will always be rather limited because they have to compete with other much more sensitive techniques (Brillouin Light Scattering, Ferromagnetic Resonance). Nevertheless, it is possible than new techniques based on spin precession techniques such as $MIEZE$ will provide a significant technical improvement that make inelastic measurements possible on very small amounts of material.

In my opinion, imaging techniques is one of the fields which is most likely to make significant technical progress.

14.3.4. Long term project: neutron imaging

In the field of cartographic magnetic measurements in the direct space, the near field probes (MFM, STM), electronic microscopy, X-ray microscopy (PEEM) have reached exceptional performances in terms of spatial resolution (5-10 nm). The techniques of neutron imaging will not be able to reach such spatial resolution in the near future. However, the previous techniques can only probe surfaces of materials in very thin films. They do not allow to probe the magnetic configurations in-depth.

I propose to use precessional techniques in order to probe such structures. The principle consists in illuminating the structure to be studied with a polarized neutron beam and to measure the Larmor precession during the interaction with the magnetic structure. In a first step, I propose to apply this technique to 1-dimensional structures such as planar magnetic domain walls in thin films (Bloch type). These walls can be artificially created in thin film hetero-structures in which one plays either with the magnetic anisotropies, or with the coupling between the materials or by the application of external magnetic fields. Precessional imaging would for example allow to probe the profile of magnetic domain walls. This information is presently not experimentally available. Demonstration experiments are presently in progress in collaboration with A. Thiaville (U. Paris-Sud/LPS) and M. Viret (CEA/SPEC).

If these measurements on one-dimensional structures are fruitful, the technique could be extended to the imaging in volume of magnetic structures at the micrometric scale. Presently, no technique is available for magnetic volume imaging at the micrometric scale. It has recently been demonstrated that it was possible to perform precessional imaging at the millimetric scale [190]. The first experiment has directly imaged the magnetic flux lines trapped in a super-conducting material (see Fig. 14.2).

These first measurements reach millimetric resolutions. In the state of the art of neutron imaging, it seems difficult to reach length scales significantly smaller than a fraction of millimeter. I propose to develop a technique which would allow to image magnetic structures at a micrometric scale. Such a technique would have an interest in the study of microsystems using permanent magnets to measure the distribution of field lines created outside the magnets (see Fig. 14.3). The technique would be based on the scanning of a micrometric neutron beam. This would alleviate the need for an ultra-high resolution neutron detector. The neutron flux presently available on polarized spectrometers would allow to perform a magnetic image in a matter of hours.
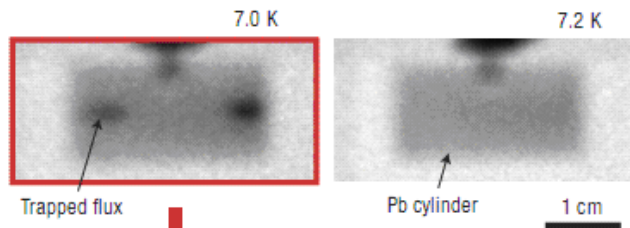
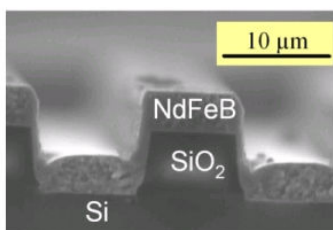Figure 14.2.: Magnetic flux trapped in a Pb cylinder (adapted from [190].)

Figure 14.3.: Permanent Magnets (NdFeB) microstructures used in micro-mechanical systems (HF switches for ex.) (N. Dempsey, Institut Néel Grenoble).

14. Perspectives

Part IV.

Annexes

Annexe I: SANS versus GISANS. Figure of merit.

In this annexe, I discuss the respective merits of performing either SANS of GISANS experiments. In the field of X-rays, the question is not relevant since x-rays cannot go through the sample. Thus in the case of thin films structure, it is always necessary to use a Grazing incidence geometry. In the case of neutrons, the substrate is usually not an issue especially when it is a silicon substrate which is perfectly transparent for neutrons. Thus the question which arises is: what is the most efficient way of performing a small angle experiment on a thin film system? Is the direct SANS geometry more efficient or does the specific GISANS geometry provide extra gains in flux?

The first key consideration is the flux incident on the sample for the different configurations SANS and GISANS. In SANS, the illuminated area of the sample can get bigger as the studied objects get smaller because the resolution can be relaxed. For large objects, the angular resolution needs to be good enough and only a fraction of the sample surface can be used. The illuminating flux is thus inversely proportional to the square of the objects sizes.

If one considers objects of a typical size ξ, the typical resolution should be of the order of $\delta Q = \frac{1}{10}\frac{2\pi}{\xi}$. The angular divergence is related to the wavevector resolution by $\delta Q \sim \frac{4\pi}{\lambda}\delta\theta$. Thus the angular resolution should be of the order of $\delta\theta = \frac{1}{2\times 10}\frac{\lambda}{\xi}$. For a collimation length L, and pin-hole diameters d, the divergence is $\delta\theta = 2\frac{d}{L}$. Thus the maxium pin-hole size that can be used is $d = \frac{\delta\theta L}{2} = \frac{1}{4\times 10}\frac{\lambda L}{\xi}$. For a typical instrumental configuration using neutrons of wavelength $\lambda = 1\,nm$, a collimation distance of $L = 10\,m$, a collimation of diameter $50\,mm$ can only be used for objects of typical size smaller than $5\,nm$.

In the case of a direct SANS geometry, the neutron flux is proportionnal to the pin-hole collimation surfaces $\phi \propto \left(\pi\left(d/2\right)^2\right)^2$.

In the case of a GISANS geometry, in the direction of the SANS scattering (perpendicular to the incidence plane), the collimation can have a size $d_y = \frac{\delta\theta L}{2} = \frac{1}{4\times 10}\frac{\lambda L}{\xi}$ as before. In the plane of incidence, in the reflection geometry, the angular resolution must be of the order of a fraction of the critical reflection angle. A value of $\delta\theta_x = 0.06°$ would be typical for a wavelength of $\lambda = 1\,nm$ since in this case the critical edge ranges from $0.4°$ for Silicon to $1°$ for Nickel. Thus the collimation in the incidence plane is $d_x = \frac{\delta\theta_x L}{2}$. The flux in a GISANS geometry is thus given by $\phi \propto \left(d_y \times 0.005\right).\left(d_y \times 0.05 sin\left(\theta_c\right)\right)$. The GISANS technique benefits from a large interaction with the sample which gives an enhancement of a factor 10 of the scattered intensity. The Figure 14.4 compares the flux incident on the sample in the two geometries (SANS and GISANS). The flux is weighted by a factor 10 in the case of the GISANS. One can see that for objects with a size larger than 50 nm, it is beneficial to use a GISANS geometry. For small objects with sizes smaller that 20 nm, a direct SANS geometry should be used.

Note that these calculations have been made for a fixed spectrometer configuration. In

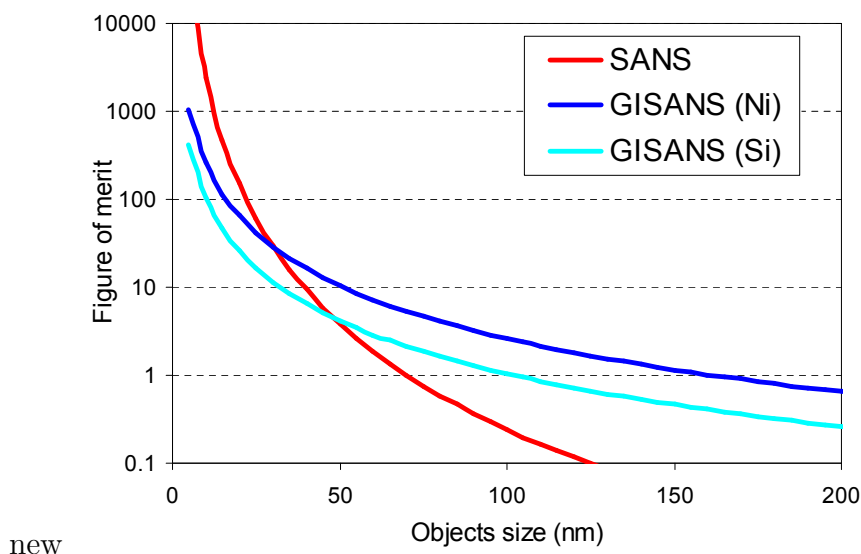*Annexe I: SANS versus GISANS. Figure of merit.*

new

Figure 14.4.: *Figure of merit of the 2 geometries (SANS and GISANS) as a function of the typical size of the objects that are being probed.*

the case of small objects, the resolution can be relaxed so that shorter wavelengths can be used (for the same configuration). The flux is thus significantly increased. However, in the case of the GISANS geometry, the critical edge is proportionnal to the wavelength so that when the wavelength is decreased, the incidence angle on the sample must be decreased so that the fraction of the beam which is intercepted by the sample is also reduced.

Besides flux considerations, other advantages of disadvantages should be mentionned for the different geometries. In the case of the GISANS geometry, the sample alignement in non trivial and is usually very temperature sensitive. Among the advantages of the GISANS technique we can mention that it is possible to achieve a depth sensitivity. It is also possible to study solid-liquid interfaces without being disturbed by the solvent by using a transmission geometry through the substrate.

In the case of the SANS geometry, no sample alignement is required which is important for temperature dependance studies. The data processing is easier. There are extra degrees of freedom since the sample can be rotated so as to probe different directions in the reciprocal space. Large samples are not required.

In a more general way, what can be the motivations for using the GISANS technique? The first one is that direct space imaging techniques such as AFM or MFM have a limited spatial resolution. The AFM or MFM techniques are also not quantitative whereas neutrons can provide values of the contrast corresponding to scattering length densities. AFM/MFM technique may also be perturbative techniques.

GISANS can also provide in-situ measurements at solid-liquid interfaces, under high magnetic fields at low temperatures. In some cases, it is possible to achieve a depth sensitivity.

One should also mention that the advent of new techniques such as multibeam techniques are likely to increase the flux on SANS spectrometer by large amounts (x20-100) so that experiments which are presently very time consuming will become routine experiments in the near future.

Annexe II: Grazing Incidence Diffraction in Laue geometry

Probing the magnetic structure of very thin films (thickness smaller than $10nm$) can be difficult because of the tiny amount of matter. For a $1cm^2$ sample it corresponds to around $10\mu g$ of magnetic material. A way of increasing the diffraction signal is to work in a grazing incidence geometry. If we consider a neutron wave incident on a surface with an angle θ_i lower than the total reflection angle θ_c, the neutron wave-function does not penetrate into the sample but travels as an evanescent wave along the surface and remains localized over a depth of around $100-400\text{Å}$ (see Figure 14.5). This effect strongly increases the interaction of the neutron with the surface. This evanescent neutron wave can be scattered by Bragg planes perpendicular to the surface. Work in this field has been performed on the spectrometer EVA at the Institut Laue–Langevin [212, 213, 214, 215].
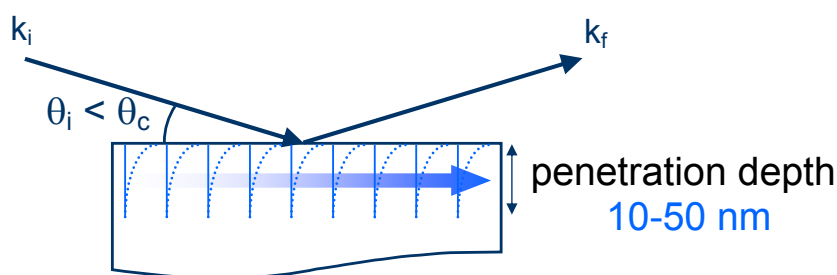

Figure 14.5.: *A neutron wave incident on a surface with an angle θ_i lower than the total reflection angle θ_c, does not penetrate into the sample but travels as an evanescent wave along the surface and remains localized over a depth of around $100-400\text{Å}$.*

The diffracted wave exits the sample surface with an angle θ_f, equal to θ_i(see Fig. 14.6red). There are however other contributions that can be observed. A fraction of the beam can be refracted at the sample surface and give a transmitted refracted diffraction signal (green). Since the sample cross section is very small (a few tens of μm), a part of the incident beam enters the side of the sample and gives a bulk contribution (blue). All these different contributions emerge at different angles with respect to the sample surface. In real experiments it is thus essential to use a Position Sensitive detector to analyze these different contributions.

It is very difficult to set-up a GID experiment on a monochromatic spectrometer since the alignments are complex and the measured signal are very weak. With T.-D. Doan, *we have proposed a new design for a neutron grazing incidence diffractometer based on a Laue-type configuration.* For our grazing incidence diffraction (GID) experiments, we have used the reflectometer EROS at the LLB. A schematic of the experimental setup is shown in Figure 14.6. The sample is mounted horizontally on a goniometric table, very

accurately aligned by the standard reflectivity procedure using the single detector placed in front of the beam. This angular alignment is crucial to perform GID measurements. The chopper is removed; thus the sample is illuminated with the full guide spectrum (Laue configuration). A 2D position-sensitive detector (PSD; $200 \times 100mm^2$), having a $0.16°$ angular resolution, can be set at a 2φ angle (ranging from $110°$ to $140°$) in the horizontal plane. The sample is then rotated accordingly into a Bragg diffraction condition. According to Bragg's law, $\lambda = 2d_{hkl}sin\varphi$, the useful wavelength is selected by the d_{hkl} of the material. The alignment of the sample is performed using the Laue configuration and then the diffracted wavelengths are identified in a Time-of-Flight measurement.

The advantages of this setup compared to a monochromatic set-up are the following:

– The detector position, 2φ, can be adjusted so that the diffracted beam corresponds to the wavelength peak of the guide spectrum.

– There is no limitation due to $\Delta\lambda/\lambda$; all possible neutrons are used for the diffraction.

– No precise adjustment of the sample angle φ (angle between the Bragg planes and the beam direction), is necessary because the 2D PSD provides a detection angle of $5°$ in the equatorial plane.

With the wavelength spectrum on EROS having a maximum around 4Å and the PSD placed at $120°$, one can investigate in-plane parameters around 2.3Å. To test the efficiency of the experimental setup, several materials were probed: single crystals of $SrTiO_3$, $LaAlO_3$, Al_2O_3, MgO and Co.
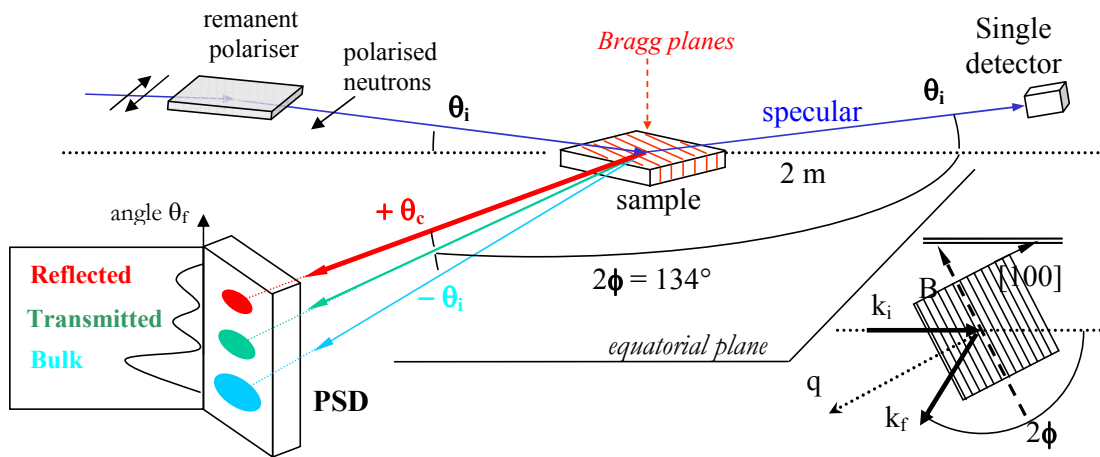
Figure 14.6.: *Surface diffraction setup in a Laue configuration. After the diffraction on the sample surface, several contributions can be observed. A reflected wave (R), a refracted wave (T) and a transmitted wave (B). Their all emerge at different angles with respect to the sample surface.*

We have studied a manganese oxide $La_{0.7}Sr_{0.3}MnO_3$ thin film deposited on a single-crystal $SrTiO_3$ substrate. The surface of the film is $1cm^2$ and its thickness is $20nm$. The thin film in-plane (1 0 0) mosaicity is $0.03°$ as measured by X-ray diffraction. The $La_{0.7}Sr_{0.3}MnO_3$ compound is ferromagnetic with $T_c = 370K$. Its lattice parameter matches perfectly the substrate ($d_{100} = 3.9$Å). The external magnetic field is applied along the [1 0 0] direction. We have performed measurements at room temperature varying the incident angle from $0.3°$ to $0.6°$ by steps of $0.05°$ with a detector position $2\phi = 134°$. The diffraction from the (1 0 0) planes of the sample was expected for $\lambda = 7$Å neutrons.

Figure 14.7 shows the signals observed on the PSD for "up" and "down" neutron polarizations in linear scale at $\lambda = 0.7nm$ in the (θ_i, θ_f) plane. At the starting incident angle $\theta_i = 0.3°$ one can observe the diffraction due to the substrate, this signal is observed for all θ_i values. As the incident angle is increased, the diffraction signal from the film (noted Reflected) arises ($\theta_f \sim 0.41°$) which is in good agreement with the expected value for the critical angle θ_c. The diffraction signal from the film is maximum at the critical angle and as the incident angle increases, its intensity strongly decreases. For $\theta_i > \theta_c$ a third feature is observed. It corresponds to the transmitted signal (noted Transmitted). Its angular position is getting closer to the substrate signal as the incident angle increases.

Figure 14.8 shows a 2D plot of the measurement obtained for an incidence angle of 0.4°. Four peaks can be observed and are marked as bulk ($\theta_f = -0.13°$), transmitted ($\theta_f = 0.12°$), and two reflected peaks ($\theta_f = 0.39°$ and $\theta_f = 0.41°$). The four observed peak positions are well explained in the formalism of the evanescent neutron scattering. A significant polarized surface signal is observed with an intensity ratio (or magnetic contrast) $I_{DO}/I_{UP} = 1.7$. The calculated polarized signals are plotted as an insert in Figure 14.8 as calculated within the DWBA approximation [112]. The amplitude of the magnetic contrast is well reproduced.

This is the first report of polarized GID measurements on a very thin magnetic film ($20nm$) demonstrating the feasibility of such measurements. More technical details can be found in [134, 135].
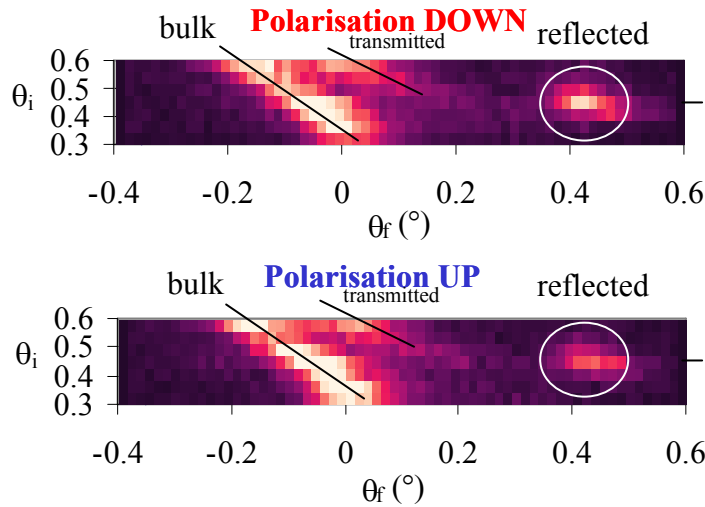
Figure 14.7.: *Intensity observed in a linear scale on the PSD as a function of the incident angle θ_i and the output angle θ_f .*

However, in practice, it proved that extremely high quality films are necessary. Moreover, the geometry is very restrictive. In order to benefit from the grazing incidence geometry, only diffraction lines in the plane of the thin films are accessible. In the case when there is a significant substrate miscut, not only the alignements become very difficult but the grazing incidence effect is lost. In later experiments, it proved that working with a very high flux, close to the reactor, in a normal 4-circles geometry led to equivalent results in terms of flux since the gain due to the grazing incidence geometry was easily compensated by the higher flux. The direct diffraction geometry, besides being easier to
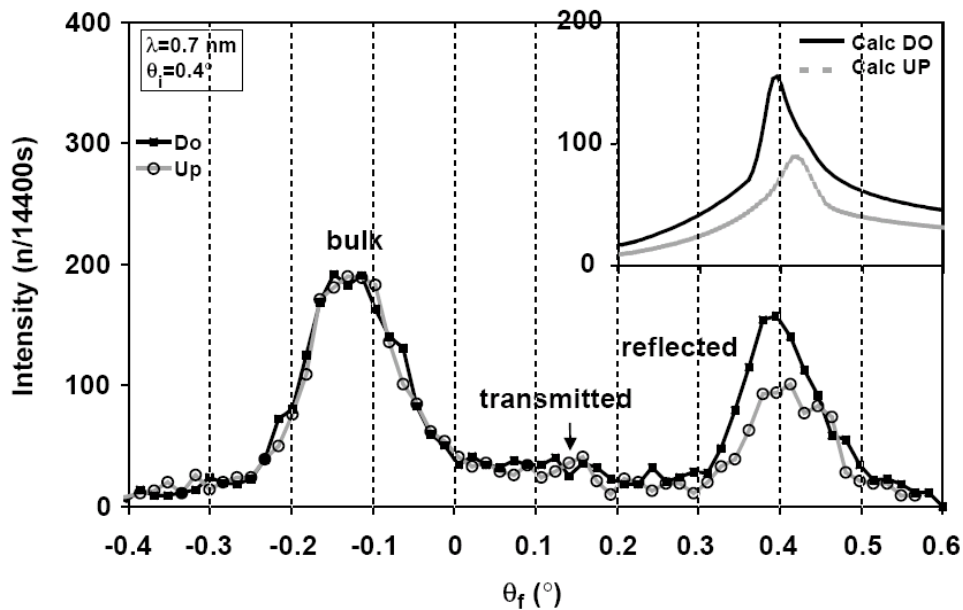
Figure 14.8.: *Polarized GID signal on the PSD for an incidence angle of 0.4°. Three diffraction peaks can be observed: the diffraction from the bulk, and the diffraction from the film in the transmission and reflection positions. DWBA calculation of the magnetic contrast (insert).*

set-up also provide the key advantage of a 4-circles geometry, i.e. that it is possible to probe any diffraction line of the thin film in the reciprocal space, which in practice is essential.

Annexe III: Inelastic scattering at very low energies

Magnetic dipolar coupling leads to low-energy excitations in magnetic materials named as magnetostatic waves (MSW) (Fig. 14.9a). The typical energy of these excitations is of the order of a few tens of meV. Among the most commonly used experimental probes, one can distinguish small wave-vector techniques (ferromagnetic resonance, Brillouin light scattering) which are very accurate, allowing to measure ultra-thin films, and inelastic neutron diffraction working at high wave-vector transfer but which is usually restricted to bulk samples.
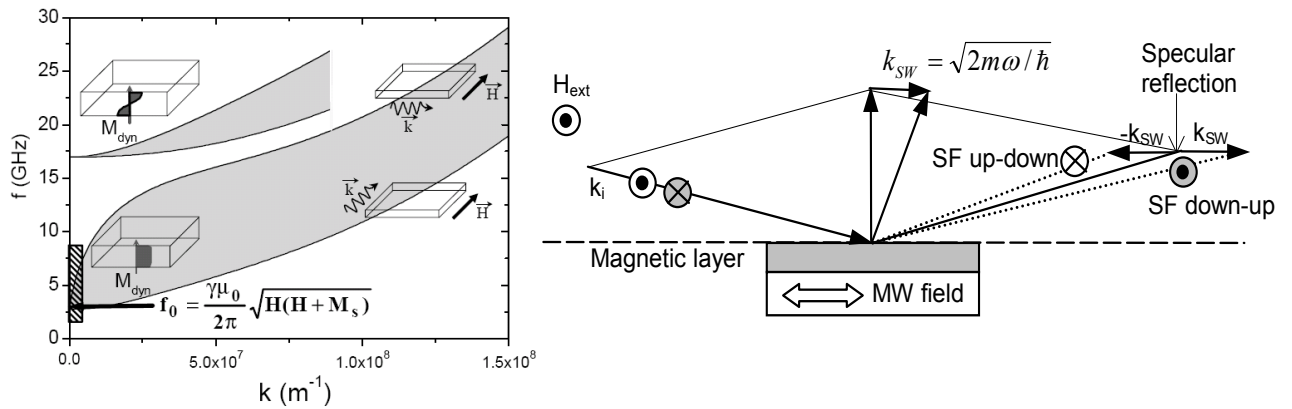
Figure 14.9.: *(a) Dispersion curve of the spin waves for a 30nm permalloy film with a 10mT in-plane bias field. The dispersion is anisotropic, depending on the angle between k and H. (b) By exchange of a magnon of energy, the reflected beam is spin-flip and its reflection direction is changed.*

We here explore the interaction of a neutron at grazing incidence with spin waves in a permalloy film. Working at grazing incidence in a reflectivity geometry makes it possible to study these very low-energy excitations. During the reflection of a wave on a surface, the in-plane component of the wavevector is preserved. If during the reflection, the neutron annihilates or creates a magnon of energy $\hbar\omega$ and wave vector k, the energy conservation and the continuity of the in-plane wave-vector component give:

$$\frac{\hbar^2 k_i^2}{2m} \pm \hbar\omega = \frac{\hbar^2 k_r^2}{2m} \quad with \quad k_{i\parallel} \pm k = k_{f\parallel}$$

where k_i and k_r are the incident and reflected scattering wavevectors. The neutron experiences a change of energy of $\hbar\omega$ which modifies its wave vector as well as a spin-flip (exchange of a spin ± 1) (see Fig. 14.9b). The relation between the incidence angle and the reflection angle induced by this interaction is $\theta_f^2 = \theta_f^2 \pm \omega/\omega_i \mp 2q/k_i$ where θ_i is the

incident neutron energy and k_i its wave vector. The grazing incidence geometry is such that very small energy changes result in large momentum transfers. Changes in the exit angles can be of the order of several degrees.

We designed a neutron set-up which allows to study these excitations. The studied samples were permalloy thin films. The MSW were either thermally excited or induced by a microwave field. The off-specular neutron reflectivity was measured using a Position sensitive detector (see Fig. 14.10).

Unfortunately, we have not been able to measure any inelastic scattered signal, even with a large microwave excitation (1W input) which enhances the spin-wave population by a factor of about 30. Numerical estimates suggest that the expected signal was in the range 10^{-5} with respect to the specular reflectivity. This was at the limit of our measurement setup.

A possibility to increase the signal is to work at lower excitation energies ($\sim 30 MHz$) in order to obtain smaller exit angles ($\sim 0.45°$) which is feasible using perpendicular resonance $\omega = \gamma\mu_0 (H - M)$ on a high-quality film such as YIG films which have narrow resonance peaks and weak magnetic dispersion.

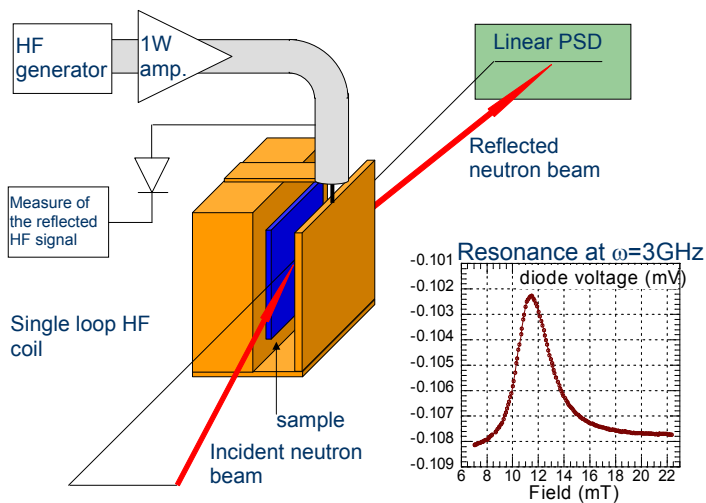More details on this study can be found in [152].

Figure 14.10.: *Description of the set-up. The sample is mounted in a single coil loop.*

Annexe IV: Scattering on ordered nanostructures

A trend in the fabrication of nanostructures is the use of templates to grow ordered nano-objects. One of the most commonly used templates are alumina membranes. The process consists in the deposition of an aluminum film which is then electrochemically oxidized to form alumina. During the process, the alumina layer self-organized into holes perpendicular to the surface (Fig. 14.11a). It is then possible to deposit materials into these holes (usually by electro-deposition) to obtain arrays of nano-objects with sizes in the range $5 - 200nm$.

Figure 14.11b shows a SEM picture of an array of holes in an alumina membrane produced by K. Lagrené. We have written small routines to extract quantitative information from these picture. By identifying the centers of the different holes, it is possible to calculate the structure factor of the distribution of holes (See Fig. 14.11c). It is isotropic and the 1D integration of the structure factor is presented on Fig. 14.11e. It is possible to model the distribution by a Percus-Yevick distribution with $\sigma_{cc} = 91nm$ and density $= 0.45$. The size distribution is also presented on Fig. 14.11d. The average hole radius is $18\,nm$ with a size distribution of 8.5nm.

These systems are rather complex for scattering studies because they are both dense systems with a marked structure factor as well as very anisotropic since there is a perfect orientation of the hole in one specific direction. The scattering on such structures is thus non trivial to process.

Let $S(Q)$ be the structure factor of the system. Let $P(Q)$ be the form factor of a hole. In the case of a perfectly homogeneous system, the scattered intensity would be $I(Q) = |P(Q)|^2 S(Q)$. In real cases, the objects are never perfectly identical so that there is some dispersion in the form factor $P(Q)$.

It is possible to use 2 different approximations. The first is to consider that the form of the wire is totally decoupled from their position so that $I(Q) = |\langle P(Q)\rangle|^2 S(Q)$. It is the decoupled approximation (DA). It is also possible to consider that the position of the holes is correlated with their size. In this case it is possible to express the scattered intensity as $I(Q) = \langle |P(Q)|^2 \rangle S(Q)$. This approximation is called the monodisperse approximation (LMA). In practice it proves that the LMA approximation works better for alumina membranes.
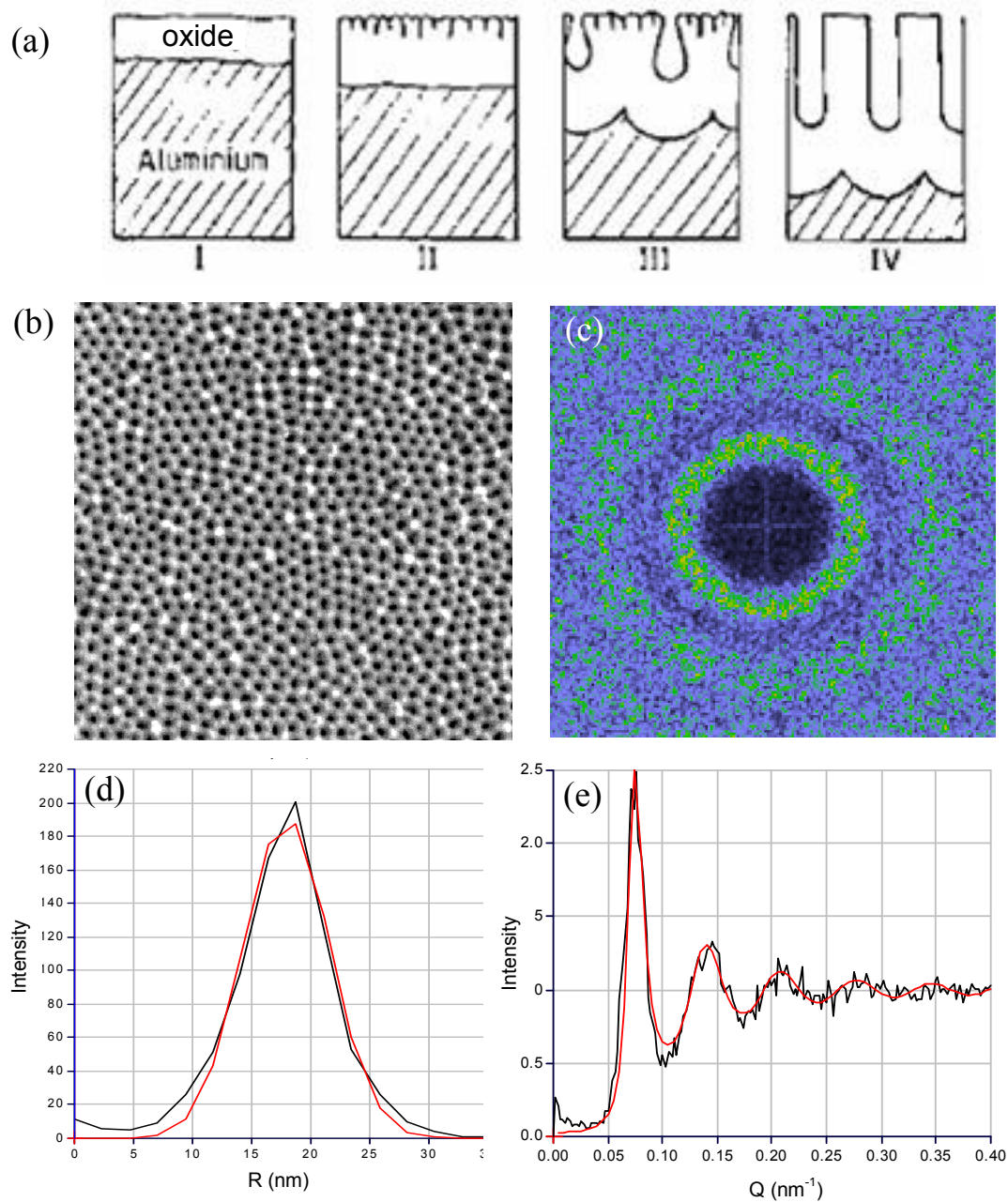
Figure 14.11.: *(a) Anodisation process. (b) SEM image of a layer of holes. (c) Structure factor of the holes positions. (d) Size distribution of the holes (R_{av} = 18 nm; s = 8.5nm) . (e) 1D structure factor modeled using a Percus Yevick distribution with σ_{cc} = 91nm and Density = 0.45.*

A more critical issue is the calculation of the scattering on these very anisotropic and very ordered systems. I present here typical geometries of the scattering on ordered planar structures. If one considers an assembly of disks (Fig. 14.12a), if the finite thickness of the system is not taken into account, a classical scattering function is observed (Fig. 14.12b). However, in the case of a thin plane of disk (Fig. 14.12c) perpendicular to the incident neutron beam, since the system has a finite thickness, the structure factor is modulated by a *sinc* function corresponding to the finite thickness of the membrane. Depending

on the characteristic size of the system, the Ewald sphere (small arc Fig. 14.12d) may see significant intensity fluctuations due to the *sinc* modulation (along the horizontal direction).

This is illustrated by the case of 3 membranes with thicknesses ranging from 5 to $50\,nm$. In the case of the thin membrane, the *sinc* modulation is very broad so that along the Ewald sphere the intensity is not too much modulated (Fig. 14.12e). For thicker systems (50 and 500nm), the *sinc* modulation becomes very narrow and the interaction with the Ewald sphere almost disappear for the thicker membrane. Thus the scattered intensity is strongly affected. These effect have to taken into account in order to process quantitatively the SANS data measured on ordered arrays of nano-objects.

Such effects are illustrated by the measurement on a membrane of very long wires of the order of 1μm (Fig. 14.13). In this case, the sample is tilted by an angle of 1.7° and one can observe both a vertical/horizontal asymmetry (Fig. 14.13a) together with a *loss of the symmetry 2* (there is more intensity on the right than on the left). In classical SANS measurements, $+Q$ and $-Q$ asymmetries are not expected. This can be accounted for by the Ewald sphere intersection (Fig. 14.13b). The calculation reproduces most of the features of the measured signal. The calculation uses the parameters determined from the SEM images.

Besides, by performing radial cuts (Fig. 14.13c), one can observe that the oscillations are better resolved than the calculations. The second oscillations of the form factor is more clearly defined on the experimental data. This means that the SEM picture of the membrane surface only gave partial and biased information about the inner structure of the membrane. The SEM only sees the surface whereas the SANS measurement probes the inner structure of the membrane and suggest that the structure is actually better defined inside the membrane compared to what can be observed on the surface.
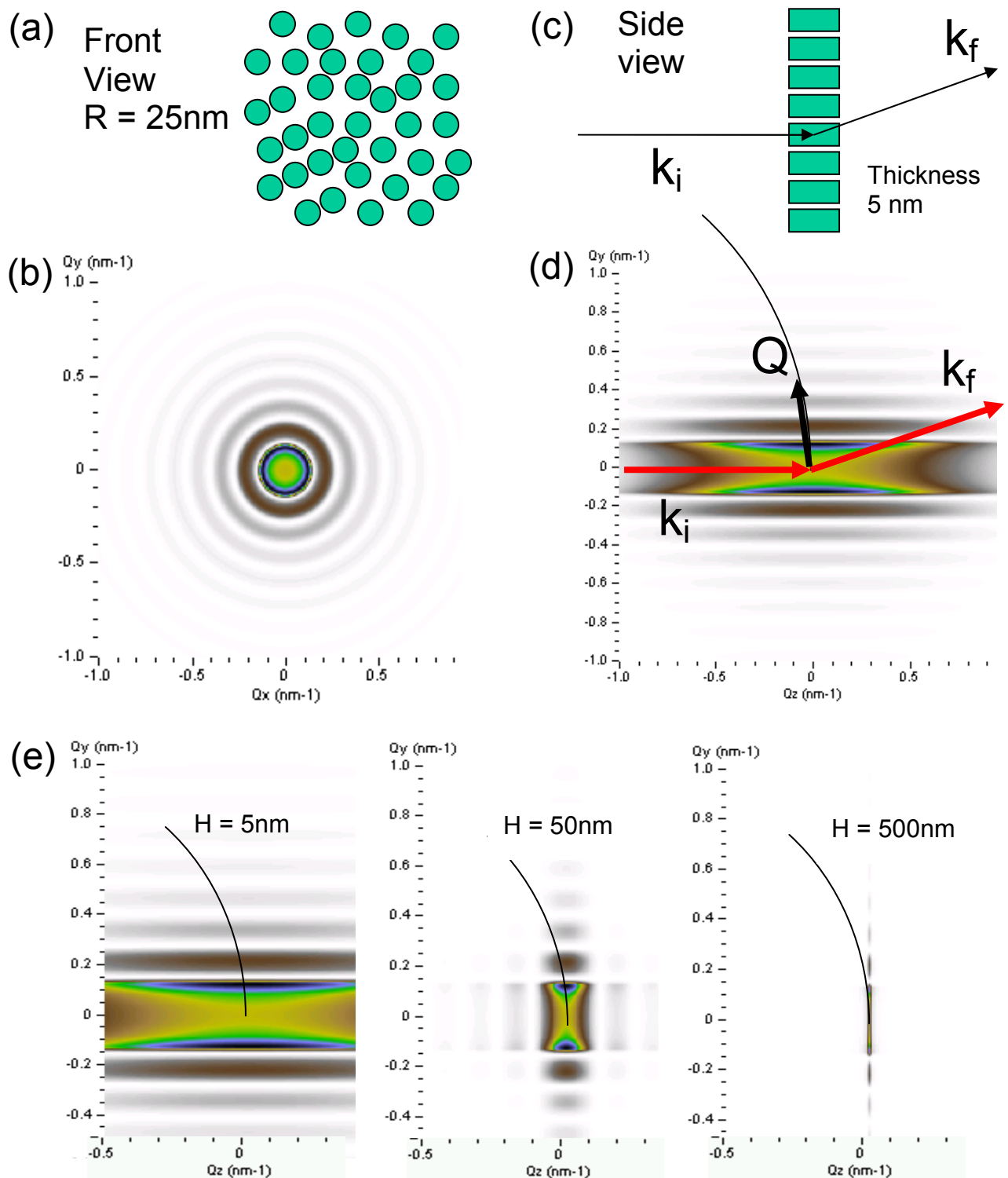
Figure 14.12.: *(a) Assembly of disk. (b) Scattering function from this assembly of disks. (c) Incidence geometry with the beam perpendicular to the plane of the membrane, that is parallel to the nanowires length. (d) 2D scattering function in the above geometry. Along the Q_y direction one has the scattering function of disks but it is modulated along the Q_z direction (incident neutron direction) by a sinc function. (e) 2D scattering function for various thickness of the membrane (H = 5 nm, H = 50 nm and H = 500 nm).*
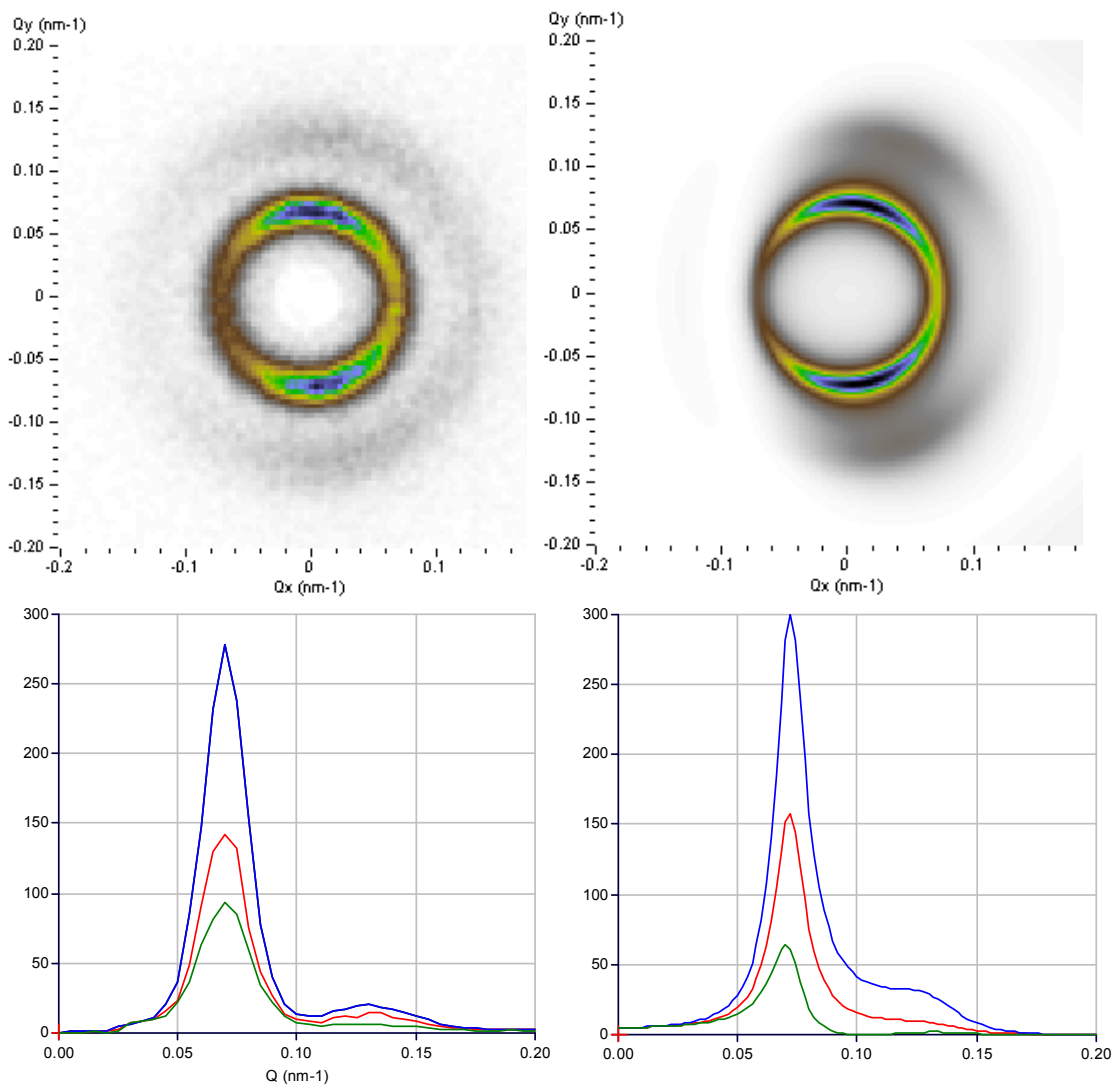
Figure 14.13.: *SANS : very long nanowires 1600nm (c) Projections along main axis*

Annexe IV: Scattering on ordered nanostructures

Bibliography

[1] C.F. Majkrzak et al, J. of Appl. Physics **63**, 3447-3452 (1988).

[2] P. Grünberg et al, Phys. Rev. Lett. **57**, 2442 (1986).

[3] A. Schreyer et al, Phys. Rev. Lett. **79,** 4914-4917 (1997).

[4] S. Langridge et al, Phys. Rev. Lett. **85**, 4964-4967 (2000).

[5] B. Hjörvasson et al, Phys. Rev. Lett. **79** ,901 (1997).

[6] YY. Huang, G.P. Felcher and S.S.P. Parkin, *J. Magn. Magn. Mater.* **99**, 31-38 (1991).

[7] W. Szuszkiewicz et al, Journal of Superconductivity **16,** 205-8 (2003).

[8] S. Singh et al, J. of Appl. Phys. **101,** 033913 (2007).

[9] H. Kepa et al, Phys. Rev B **64,** 121302 (2001); W. Szuszkiewicz et al, Journal of Superconductivity **16**, 209-12 (2003).

[10] H. Kepa et al, EuroPhysics Lett. **56,** 54-60 (2001).

[11] M.N. Baibich, J.M. Broto, A. Fert, F. Nguyen Van Dau, F. Petroff, P. Etienne, G. Creuzet, A. Friedrich, J. Chazelas, *Phys. Rev. Lett.* **61**, 2472 (1988).

[12] S.G.E. te Velthuis et al, Phys. Rev. Lett. **89,** 127203 (2002); S.G.E te Velthuis et al, *J. Appl. Phys.* **87,** 5046 (2000); S.G.E. te Velthuis et al, *Appl. Phys. Lett.* **75,** 4174-6 (1999).

[13] F. Radu et al, *J. Magn. Magn. Mater.* **240,** 251-253 (2002); F. Radu et al, Phys. Rev. B **67,** 134409 (2003).

[14] J. Noguès et al, *J. Magn. Magn. Mater.* ***192,*** 203-232 (1999); M.R. Fitzsimmons et al, *Phys. Rev. Lett.* **84,** 3986-89 (2000); M. Gierlings et al, *Phys. Rev.* B **65,** 092407/1-4 (2002).

[15] S. Lee, A. Pirogov, M.S. Kang et al. Nature **451**, 805 (2008).

[16] V. Lauter-Pasyuk et al, Physica B **248,** 166-170 (1998).

[17] K.V. O'Donovan, J.A. Borchers, C.F. Majkrzak, O. Hellwig and E.E. Fullerton, *Phys. Rev. Lett.* **88,** 067201/1-4 (2002).

[18] D. Haskel et al, *Phys. Rev. Lett.* **87,** 207201/1-4 (2001); V. Leiner et al, *Physica* B **283,** 167-70 (2000).

Bibliography

[19] J. Stahn et al, Phys. Rev B **71,** 140509 (2005); J. Chakhalian et al, Nature Physics **2,** 244-248 (2006).

[20] L.T. Baczewski et al, Phys. Rev. B **74,** 075417 (2006).

[21] V. Lauter-Pasyuk et al, Phys. Rev. Lett. **89,** 167203 (2002).

[22] O. Fruchart, P.O. Jubert, C. Meyer C et al., Journal of Magnetism and Magnetic Materials **239** (2002) 224-227.

[23] T.L. Wade and J.-E. Wegrowe, Eur. Phys. J. Appl. Phys. **29**, 3–22 (2005).

[24] C.P. Li, I.V. Roshchin, X. Batlle et al., J. Appl. Phys. **100**, 074318 (2006).

[25] C. Desvaux, C. Amiens, P. Fejes et al. Nature Materials **4**, 750-753 (2005).

[26] M. Klokkenburg et al., Phys. Rev. E **75** (2007) 51408 .

[27] A. Wiedenmann et al., J. Phys. **18** (2006) s2713.

[28] D. Ung, Y. Soumare, N. Chakroune, G. Viau, M. J. Vaulay, V. Richard, F. Fievet, Chem. Mater. **19**, 2084-2094 (2007).

[29] J. Lekner, *Theory of reflection of electromagnetic and particle waves* (Martinus Nijhoff, Dordrecht, 1987).

[30] C. Fermon, F. Ott and A. Menelle, Neutron reflectivity, pp.163; F. de Bergevin pp.3, in: J. Daillant and A. Gibaud (eds) X-Ray and Neutron Reflectivity: Principles and Applications, Springer Lecture Notes in Physics, Berlin 1999.

[31] G.P. Felcher, R.O. Hilleke, R.K. Crawford, J. Haumann, R. Kleb and G. Ostrowski, *Rev. Sci. Instr.* **58**, 609-619 (1987).

[32] S.J. Blundell and J.A.C. Bland, *Phys. Rev. B* **46**, 3391-400 (1992).

[33] C. Fermon, C. Miramond, F. Ott, G. Saux, *J. of Neutron Research* **4**, 251 (1996).

[34] N.K. Pleshanov, *Z. Phys. B* **94**, 233-243 (1994).

[35] C.F. Majkrzak, *Physica B* **221**, 342-356 (1996).

[36] H. Zabel, R. Siebrecht, A. Schreyer, Physica B **276-278** (2000) 17-21.

[37] H. Zabel, K. Theis-Brohl, J. Phys.: Condens. Matter **15** (2003) S505-S517.

[38] G.P. Felcher, J. Applied Physics **87** (2000) 5431-6; G.P. Felcher, Physica B **267-268** (1999) 154-161.

[39] M.R. Fitzsimmons et al, J. Magn. Magn. Mater **271,** 103-146 (2004).

[40] A. Schreyer, J.F. Ankner, T. Zeidler, H. Zabel, C.F. Majkrzak, M. Schaefer and P. Gruenberg, *Euro. Phys. Lett.* **32**, 595-600 (1995).

[41] J.A.C. Bland et al., Journal of Magnetism and Magnetic Materials **93,** 513-522 (1991); A. Schreyer et al, Euro. Phys. Lett. **32,** 595-600 (1995).

[42] D.E Bürgler, P. Grünberg, S.O. Demokritov and M.T. Johnson, *Interlayer exchange coupling in layered magnetic structures* , in: K H J Buschow (ed.) *Handbook of Magnetic Materials* vol 13, CityplaceAmsterdam, Elsevier, 2001, pp. 1.

[43] H. Kępa, C.F. Majkrzak, A. Yu. Sipatovdand, T.M. Giebultowicz, Physica B **397**, 36-42 (2007).

[44] L. Cheng et al, Physical Review B **69**, 5 (2004).

[45] A. Bergmann et al, Physical Review B **72**, 12 (2005).

[46] M. Vadala et al, Journal of Physics D-Applied Physics **40**, 1289 (2007).

[47] A. M. Beesley, et al., Journal of Physics-Condensed Matter **16**, 8507 (2004).

[48] S. Singh et al, Electrochemical and Solid State Letters **9**, J5 (2006).

[49] M.R. Fitzsimmons et al, Phys. Rev. B **73,** 134413 (2006).

[50] V. Leiner, M. Ay, and H. Zabel, Physical Review B **70**, 1 (2004).

[51] S. Bedanta et al, Physical Review B **74**, 5 (2004).

[52] P. Böni, *Physica B* **234-236**, 1038-1043 (1997).

[53] S. Nerger et al, Physica B **297,** p.185-8 (2001).

[54] C. Cornea, D. Stoeffler, J. Magn. Magn. Mater. **198-199** (1999) 282; C. Cornea, Ph.D. Thesis, Louis Pasteur University, Strasbourg, 1999.

[55] E. Kentzinger, U. Rücker, W. Caliebe, G. Goerigk, F. Werges, S. Nerger, J. Voigt, W. Schmidt, B. Alefeld, C. Fermon, Th. Brückel, Physica B **276-278** (2000) 586.

[56] M. Pannetier, T.D. Doan, F. Ott, S. Berger, N. Persat, C. Fermon, Europhysics Letters **64,** 524-8 (2003).

[57] S. Moyerman et al, Journal of Applied Physics **99,** (2006)

[58] C. Schanzer et al, Physica B-Condensed Matter **356,** 46-50(2004)

[59] Z. Y. Zhao et al, Physical Review B **71,** 1098-0121(2005).

[60] M.R. Fitzsimmons et al, Phys. Rev. Lett. **84,** 3986-89; (2000); C. Leighton et al, *Phys. Rev.* B **65,** 064403/1-7 (2002); M.R. Fitzsimmons et al, Phys. Rev. B **65,** 134436 (2002).

[61] M. Gierlings et al, *Phys. Rev.* B **65,** 092407/1-4 (2002).

[62] P. Blomqvist et al, Journal of Applied Physics **96,** 6523-6526 (2004).

[63] A. Paul et al, Phys. Rev. B 1098-0121 (2006).

Bibliography

[64] S. Roy et al, Phys. Rev. Lett. **95,** 047201 (2005).

[65] C. Fermon, Physica B **213 & 214** (1995) 910-913.

[66] G.P. Felcher, S. Adenwalla, V.O. De Haan and A.A. Van Well, *Nature* **377**, 409 (1995).

[67] G.P. Felcher, S. Adenwalla, V.O. de Haan, A.A. van Well, *Physica B* **221**, 494-499 (1996).

[68] L. Névot and P. Croce, *Revue de Physique Appliquée* **15**, 761 (1980).

[69] B. Toperverg, Physica B **297**, 160 (2001).

[70] E. Kentzinger, U. Rücker, B. Toperverg, F. Ott and T. Brückel, Phys. Rev. B **77**, 104435 (2008).

[71] https://neutronreflectivity.neutron-eu.net/main/Reflectometers

[72] F. Mezei, *Z. Phys.* **255**, 146 (1972).

[73] X. Zhao, W. Zhao, X. Zheng, M.H. Rafailovich, J. Sokolov, S.A. Schwarz, M.A.A. Pudensi, T.P. Russel, S.K.Kumar and L.J. Fetters, *Phys. Rev. Lett.* **69**, 776 (1992).

[74] J. A. Dura, C. A. Richter, C. F. Majkrzak, and N. V. Nguyen, Applied Physics Letters **73**, 2131 (1998).

[75] H. H. Chen-Mayer, G. P. Lamaze, K. J. Coakley, and S. K. Satija, Nuclear Instruments & Methods in Physics Research Section a-Accelerators Spectrometers Detectors and Associated Equipment **505**, 531 (2003).

[76] D. G. Wiesler and C. F. Majkrzak, Physica B **198**, 181 (1994).

[77] V. M. Pusenkov, K. Moskalev, N. Pleshanov, A. Schebetov, V. Syromyatnikov, V. Ul'yanov, A. Kobzev, and O. Nikonov, Physica B **276**, 654 (2000). S. V. Metelev, N. K. Pleshanov, A. Menelle, V. M. Pusenkov, A. F. Schebetov, Z. N. Soroko, and V. A. Ul'yanov, Physica B **297**, 122 (2001).

[78] B. D. Vogt, H. J. Lee, V. M. Prabhu, D. M. DeLongchamp, E. K. Lin, W. L. Wu, and S. K. Satija, Journal of Applied Physics **97**, 7 (2005).

[79] Z. Tun, J. J. Noel, and D. W. Shoesmith, Physica B **241**, 1107 (1997); Z. Tun, J. J. Noel, and D. W. Shoesmith, Journal of the Electrochemical Society **146**, 988 (1999).

[80] J. J. Noel, H. L. Jensen, Z. Tun, and D. W. Shoesmith, Electrochemical and Solid State Letters **3**, 473 (2000).

[81] J. Majewski, T. L. Kuhl, M. C. Gerstenberg, J. N. Israelachvili, and G. S. Smith, Journal of Physical Chemistry B **101**, 3122 (1997).

[82] T. Charitat, E. Bellet-Amalric, G. Fragneto, and F. Graner, European Physical Journal B **8**, 583 (1999).

[83] A. P. Maierhofer, D. G. Bucknall, and T. M. Bayer, Biophysical Journal **79**, 1428 (2000).

[84] D. Schwendel, T. Hayashi, R. Dahint, A. Pertsin, M. Grunze, R. Steitz, and F. Schreiber, Langmuir **19**, 2284 (2003).

[85] I. Burgess, M. Li, S. L. Horswell, G. Szymanski, J. Lipkowski, J. Majewski, and S. Satija, Biophysical Journal **86**, 1763 (2004).

[86] F. Ott et al, J. Mag. Mag. Mat. **211,** 200-205 (2000).

[87] R.P. Borges et al, Journal of Applied Physics **89,** p. 3868-73 (2001).

[88] J.-B. Moussy et al, Phys. Rev. B **70**, 174448 (2004).

[89] G.P. Felcher et al, Neutron News **5,** 18-22 (1994).

[90] D. L. Nagy, et al., Physical Review Letters **88**, 4 (2002).

[91] H. Lauter, et al., Journal of Magnetism and Magnetic Materials **258**, 338 (2003); V. Lauter-Pasyuk et al, Journal of Magnetism and Magnetic Materials **226**, 1694 (2001).

[92] A. Paul et al, Physica B-Condensed Matter **356**, 31 (2005);

[93] M. Gierlings et al, Physica B **356** 36-40 (2004).

[94] A. Paul et al, Physica B **356** 26-30 (2005).

[95] U. Rücker, E. Kentzinger, B. Toperverg, F. Ott, Th. Brückel, Appl. Phys. A **74** S607-609 (2002).

[96] E. Kentzinger, U. Rucker, B. Toperverg, et al, Physica B **335,** 89-94 (2004).

[97] S.V. Kozhevnikov, F. Ott, E. Kentzinger, A. Paul, Physica B **397**, 68-70 (2007).

[98] F. Ott, A. Menelle, C. Fermon, P. Humbert, Physica B **283,** 418-421 (2000).

[99] F. Ott, P. Humbert, C. Fermon and A. Menelle, Physica B **297,** p.189-93 (2001).

[100] K. Theis-Brohl, Physica B-Condensed Matter **345**, 161-168 (2004); K. Theis-Brohl et al, , Physical Review B **71**, 4 (2005); K. Theis-Brohl et al, Physica B **356**, 14 (2005).

[101] S. Langridge, et al., Physical Review B **74**, 6 (2006).

[102] K. Temst et al, European Physical Journal B **45** 261-266 (2005); K. Temst et al, Journal of Magnetism and Magnetic Materials **304** 14-18 (2006)

[103] E. Popova et al, European Physical Journal B **44** 491-500 (2005).

[104] K. Theis-Brohl, et al., Physical Review B **73**, 14 (2006)

Bibliography

[105] E. Kentzinger, U. Rücker, B. Toperverg, F. Ott and T. Brückel, Phys. Rev. B **77**, 104435 (2008).

[106] F. Pfeiffer et al., Phys. Rev. Lett. **88** (2002) 055507-1.

[107] S.P. Pogossian et al., Phys. Rev. B **53** (1996) 14359.

[108] U. Rücker et al., Physica B **297** (2001) 140.

[109] V.K. Ignatovich, F. Radu, Phys. Rev. B **64** (2001) 205408-1.

[110] E. Kentzinger et al., Physica B **335** (2003) 82.

[111] E. Kentzinger et al., Physica B **335** (2003) 89.

[112] B.P. Toperverg, Physica B **297** (2001) 160.

[113] M. Klokkenburg et al, Phys. Rev. E **75** (2007) 51408.

[114] M. Viret, H. Glattli, C. Fermon et al. Euro. Phys. Lett. **42**, 301-306 (1998).

[115] A. Pautrat, J. Scola, C. Simon et al. Phys. Rev. B **71**, 064517 (2005).

[116] E. Dagotto, Nanoscale phase separation and colossal magnetoresistance: the physics of manganites and related compounds (Springer-Verlag, Berlin, 2003).

[117] Y. Tomioka, A. Asamitsu, H. Kuwahara, Y. Morimoto and Y. Tokura, J. Phys. Soc. Jpn. **64**, 3626 (1995).

[118] A. Anane et al, Phys. Rev. B **59**, 77 (1999).

[119] M. Viret et al, Phys. Rev. Lett. **93** (2004) 217402.

[120] Rauscher et al , Phys. Rev. B **52** (1995) 16855.

[121] Ch. Simon, S. Mercone, N. Guiblin, C. Martin, A. Brulet and G. Andre, Phys. Rev. Lett. **89**, 2072021 (2002).

[122] J. W. Lynn, J. Appl. Phys. **75** (1994) 6806.

[123] Q. Huang, P. Karen, V L. Karen, A. Kjekshus, J. W. Lynn, A. D. Mighell, N. Rosov. and A. Santoro. Phvs. Rev. B **45**, 9611 (1992).

[124] M.A. Aebersold, B. Gillon, O. Plantevin et al, J. Am. Chem. Soc. **120** (1998) 5238-5245.

[125] C. Piquer, F. Grandjean, O. Isnard et al. J. Appl. Phys. **95** (2004) 6308-6316.

[126] J. W. Lynn, T. W. Clinton, W-H. Li, R. W. Erwin, J. Z. Liu, K. Vandervoort, and R. N. Shelton, Phys. Rev. Lett. **63**, 2606 (1989).

[127] D. M. Lind, S. P. Tay, S. D. Berry, J. A. Borchers, and R. W. Erwin, Journal of Applied Physics **73**, 6886 (1993).

[128] T.F. Doan, B. Hennion and F. Ott, unpublished data.

[129] P. J. van der Zaag, Y. Ijiri, J. A. Borchers, L. F. Feiner, R. M. Wolf, J. M. Gaines, R. W. Erwin, and M. A. Verheijen, Physical Review Letters **84**, 6102 (2000).

[130] J. A. Borchers, M. J. Carey, R. W. Erwin, C. F. Majkrzak, and A. E. Berkowitz, Physical Review Letters **70**, 1878 (1993).

[131] H. Béa, M. Bibes, S. Petit, J. Kreisel, and A. Barthelemy, Philosophical Magazine Letters **87**, 165 (2007).

[132] H. Bea, M. Bibes, F. Ott, B. Dupe, X.-H. Zhu, S. Petit, S. Fusil, C. Deranlot, K. Bouzehouane, and A. Barthelemy, Phys. Rev. Lett. **100**, 017204 (2008).

[133] J. A. Borchers, Y. Ijiri, D. M. Lind, P. G. Ivanov, R. W. Erwin, A. Qasba, S. H. Lee, K. V. O'Donovan, and D. C. Dender, Applied Physics Letters **77**, 4187 (2000).

[134] T.-D. Doan, F. Ott, A. Menelle, U. Rücker, P. Humbert, C. Fermon, I.L. Prejbeanu, Applied Physics A **74** (2002) S186-188.

[135] T.D. Doan, F. Ott, A. Menelle, C. Fermon, Physica B **335** (2003) 72-6.

[136] V. Garcia, Y. Sidis, M. Marangolo, F. Vidal, M. Eddrief, P. Bourges, F. Maccherozzi, F. Ott, G. Panaccione and V. H. Etgens, Phys. Rev. Lett. **99**, 117205 (2007).

[137] N. Menyuk et al., Phys. Rev. **177**, 942 (1969).

[138] D. Lebeugle, D. Colson, A. Forget et al. Phys. Rev. Lett. **100**, 227602 (2008).

[139] C. Dufour, K. Dumesnil, S. Soriano, et al. Phys. Rev. B **66** (2002) 094428.

[140] K. Dumesnil, C. Dufour, P. Mangin, et al. Phys. Rev. B **60** (1999) 10743-10746.

[141] A. Mougin, C. Dufour, K. Dumesnil, et al. Phys. Rev. B **59** (1999) 5950-5959.

[142] G. Shirane, S. M. Shapiro, J. M. Tranquada, Neutron Scattering with a Triple-Axis Spectrometer: Basic Techniques (Cambridge University Press, 2006)

[143] M. Hennion, C. Bellouard, I. Mirebeau, J. L. Dormann, and M. Nogues, Europhysics Letters **25**, 43 (1994).

[144] C. Bellouard, I. Mirebeau, and M. Hennion, Physical Review B **53**, 5570 (1996).

[145] M. F. Hansen, F. Bodker, S. Morup, K. Lefmann, K. N. Clausen, and P. A. Lindgard, Physical Review Letters **79**, 4910 (1997).

[146] H. Casalta, et al., Physical Review Letters **82**, 1301 (1999).

[147] S.N. Klausen, K. Lefmann, P.-A. Lindgard et al, J.M.M.M. **266** (2003) 68–78.

[148] P. Grünberg, Light Scattering in Solids V (edited by M. Cardona and G. Güntherodt, Springer, Berlin, 1989).

Bibliography

[149] B. Heinrich, Ultra-thin Manetic Structures Vol II, pp. 195-257 (edited B. Heinrich and J.A.C.. Bland Springer, Berlin, 1994).

[150] A. Schreyer et al, Journal of applied physics **87** (2000) 5443 – 5448.

[151] B. Hennion et al, Physical Review B **66** (2002) 224426; B. Hennion et al, J. of superconductivity. **16** (2003) 151 – 154.

[152] M. Bailleul, F. Ott, C. Fermon, Physica B **335** (2003) 68-71.

[153] P. Mazur and D. L. Mills, Phys. Rev. B **26**, 5175–5186 (1982);

[154] D.A. Korneev, V.I. Bodnarchuk, V.F. Peresedov, V.V. Zhuravlev, A.F. Schebetov, Physica B **276-278** (2000) 314-315.

[155] http://material.fysik.uu.se/Group_members/adrian/reflect.htm

[156] http://neutronreflectivity.neutron-eu.net/main

[157] S. Soriano, C. Dufour, K. Dumesnil et al. European Phys. Journal 63, **469-478** (2008).

[158] A. Hubert and R. Schäfer, Magnetic Domains, Springer Verlag, Berlin, 1998.

[159] R.C. O'Handley, Modern Magnetic Materials, Principles and Applications, John Wiley, New York, 2000.

[160] R. Skomski, H. Zeng, D.J. Sellmyer, IEEE Trans. Mag. **37** (2001) 2549.

[161] M. Pannetier, T. D. Doan, F. Ott, S. Berger, N. Persat and C. Fermon, Europhys. Lett., **64** (4), pp. 524–528 (2003)

[162] R. Labusch, Phys. Stat. Sol. (a) **137** (1993) 525.

[163] R.C. O'Handley, J.P. Woods, Phys. Rev. B **42** (1990) 6568.

[164] A. Aharoni, Phys. Rev. B **47** (1993) 8296.

[165] G. Jung, V. Markovich, C. J. van der Beek, D. Mogilyansky, Y. M. Mukovskii, and Ht, Physical Review B **72**, 6 (2005).

[166] V. Markovich, G. Jung, Y. Yuzhelevski, G. Gorodetsky, Y. M. Mukovskii, and Zi, European Physical Journal B **48**, 41 (2005).

[167] M. Viret, F. Ott, J.P. Renard et al., Phys. Rev. Lett. **93**, 217402 (2004).

[168] J.M.D. Coey, M. Viret and S. von Molnar, Advances in Physics **48**, 167-293 (1999).

[169] O. Glatter et O. Kratky, Small Angle X-ray scattering (Academic Press, London, 1982).

[170] J. Als-Nielsen, Z. Phys. B: Condens. Matter **61** (1985) 411.

[171] McStas : http://neutron.risoe.dk/

140

[172] VITESS http://www.hmi.de/projects/ess/vitess/

[173] ResTrax http://omega.ujf.cas.cz/restrax/

[174] W. Jark, F. Pérennès and M. Matteucci, J. Synchrotron Rad. (2006) **13**, 239-252

[175] http://www-llb.cea.fr/prism/programs/simulspectro/simulspectro2D.html

[176] J. Major et al, Physica B **336** (2003) 8.

[177] http://www-llb.cea.fr/prism/programs/spectraprocessor/spectraprocessor.html

[178] F. Ott, A. Menelle, Physica B **385-86** (2006) 985-988.

[179] F. Ott, A. de Vismes, Physica B **397** (2007) 153-155.

[180] R. Cubitt et al, NIM A **558** (2006) 547-550.

[181] C.F. Majkrzak, Physica B **173** (1991) 75-88.

[182] F. Ott, Nuclear Instruments and Methods in Physics Research A **584** (2008) 401–405.

[183] http://www.ncnr.nist.gov/expansion/CANDOR053007.html

[184] F. Ott, A. Menelle, Nuclear Instruments and Methods in Physics Research A **586** (2008) 23–30.

[185] http://www.ncnr.nist.gov/expansion/MAGIK053007.html

[186] http://www-llb.cea.fr/prism/programs/simulreflec/simulreflec.html

[187] E. Morenzoni, R. Khasanov, H. Luetkens, T. Prokscha, A. Suter, Journal of Neutron Research, **14** (2006) 269 - 278.

[188] C. Hugenschmidt, K. Schreckenbach, M. Stadlbauer, and B. Straer; Appl. Surf. Sci. , **25**2 (2006) 3098-3105.

[189] http://nuclear.uwinnipeg.ca/ucn/triumf/

[190] N. Kardjilov et al, Nature Physics **4**, 399 - 403 (2008)

[191] C. F. Majkrzak, J. W. Cable, J. Kwo, M. Hong, D. B. McWhan, Y. Yafet and J. Waszcak, *Phys. Rev. Lett.* **56**, 2700 (1986).

[192] V.F. Sears, *Physics Report* **141**, 281 (1986).

[193] X.L. Zhou, S.H. Chen, *Physics Reports* **257**, 223-348 (1995).

[194] H. Glättli and M. Goldman, *Methods of experimental Physics, Vol 23C, Neutron Scattering* (Academic Press, Orlando, 1987).

[195] S. Dietrich, A. Haase, *Physics Reports* **260**, 1-138 (1995).

Bibliography

[196] V.F. Sears, *Methods of experimental Physics, Vol 23A, Neutron Scattering* (Academic Press, Orlando, 1987); V.F. Sears, *Neutron News* **3**, 26 (1992).

[197] NISP http://paseeger.com/

[198] H. Fritzsche et al, Phys. Rev B **70,** 214406 (2004).

[199] J. B. Laloe et al, Ieee Transactions on Magnetics **42** (2006).

[200] D. Schmitz et al, J. Magn. Magn. Mater. **269,** 89-94 (2004).

[201] C. Fermon et al, Physica B **267-268** 162-7 (1999).

[202] M. Pannetier, F. Ott, C. Fermon, Y. Samson, Physica B **335,** 54-8 (2003).

[203] A. Ramos, S. Matzen, J.-B. Moussy, F. Ott, M. Viret, Phys. Rev. B **79** 014401 (2009).

[204] W. Szuszkiewicz et al, Journal of Alloys and Compounds **423**, 172-175 (2006).

[205] C.F. Majkrzak and N.F. Berk, *Phys. Rev. B* **52**, 10827 (1995).

[206] C.F. Majkrzak and N.F. Berk, *Phys. Rev. B* **58**, 15416 (1998).

[207] J. Kasper , H. Leeb and R. Lipperheide, *Phys. Rev. Lett.* **80**, 2614-2617 (1998).

[208] A. Ruhm, B. P. Toperverg, and H. Dosch, Physical Review B **60**, 16073 (1999).

[209] W. Lohstroh, G. P. Felcher, R. Goyette, M. Munzenberg, and W. Felsch, Physica B **268**, 352 (1999); W. Lohstroh, M. Munzenberg, W. Felsch, H. Fritzsche, H. Maletta, R. Goyette, and G. P. Felcher, Journal of Applied Physics **85**, 5873 (1999). W. Lohstroh, M. Munzenberg, W. Felsch, H. Fritzsche, H. Maletta, and G. P. Felcher, Journal of Magnetism and Magnetic Materials **199**, 440 (1999).

[210] W. T. Lee, S. G. E. te Velthuis, G. P. Felcher, F. Klose, T. Gredig, and E. D. Dahlberg, Physical Review B **65**, 6 (2002).

[211] N.K. Pleshanov, Physica B **269** (1999) 79.

[212] H. Dosch: Critical Phenomena at Surfaces and Interfaces. Evanescent X-ray and Neutron Scattering (Springer, Berlin, Heildelberg 1992) pp. 32–54 4.

[213] H. Dosch, K. Al Usta, A. Lied, W. Drexel, J. Peisl: Rev. Sci. Instrum. **63**, 5533 (1992) 5.

[214] H. Dosch: Physica B **192**, 163 (1993) 6.

[215] R. Günther, S. Odenbah, O. Schärpf, H. Dosch: Physica B **234–236**, 508 (1997)